Low-valent molecular cobalt complexes for CO_2 reduction

Carla Casadevall[a,b,*] **and Julio Lloret-Fillol**[b,c,*]
[a]Department of Physical and Inorganic Chemistry, University Rovira i Virgili (URV), Carrer Marcel·lí Domingo, Tarragona, Spain
[b]Institute of Chemical Research of Catalonia (ICIQ), The Barcelona Institute of Science and Technology, Avinguda dels Països Catalans, Tarragona, Spain
[c]Catalan Institution for Research and Advanced Studies (ICREA), Passeig Lluís Companys, Barcelona, Spain
*Corresponding authors. e-mail address: carla.casadevall@urv.cat; jlloret@iciq.es

Contents

Abstract

This chapter explores the most representative catalytic systems for electro- and photocatalytic CO_2 reduction into fuels and chemicals, as promising strategies to produce carbon-based fuels and chemicals in a sustainable manner. Practical application of CO_2 reduction faces challenges such as enhancing catalyst activity (turnover numbers, turnover frequencies), achieving high energy efficiency (low overpotential), ensuring excellent selectivity and efficiency for desired products (Faraday efficiencies, product yield, quantum yields), and maintaining long-term stability used earth-abundant-based systems. A deeper understanding of reaction mechanisms is crucial to favor pathways yielding desired products while avoiding undesired ones. Recent

Advances in Catalysis
ISSN 0360-0564, https://doi.org/10.1016/bs.acat.2024.07.001

years have seen the emergence of rational design strategies to boost activity without compromising overpotential or selectivity. This review focuses on molecular cobalt-based catalysts as pivotal components in this evolution. The chapter is divided into two main sections: the first covers the developed and studied cobalt complexes based on heme ligands, such as porphyrins and phthalocyanines, while the second addresses cobalt complexes with non-heme ligands. Key aspects for catalyst development in this rapidly advancing field are discussed.

1. Introduction

Our society, since the industrial revolution, has heavily relied on fossil fuels for energy generation, transportation, production of fertilizers, industrialization, and chemical production *(1,2)*. The consequence of the oxidation of huge amounts of carbon deposited over millions of years thanks to Natural photosynthesis and geological transformations (fossil fuels) has been the emission of huge amounts of carbon dioxide on a time scale of decades, resulting in an alteration of the carbon balance on our planet *(3)*. The atmospheric CO_2 levels have raised from the about 280 ppm *(4)*, to surpass 425 ppm in 2024, and projections grew further with the current technologies *(5–7)*. Carbon dioxide levels have a direct impact on global warming, ocean acidification, sea levels and life on earth *(8)*. The recognition of the anthropogenic CO_2 emissions, its impact in the clime and the economic and social impact has led to social, political, and economic movements to promote alternative technologies with low, zero or negative CO_2 emissions. Only by scientific advancement and technological innovation, we will be able to develop the technologies necessary to transition to a low-carbon emission economy *(1)*.

Certainly, the carbon dioxide reduction reaction (CO_2RR) to fuels and chemicals using renewable energy is pivotal in the quest for sustainable energy solutions and environmental preservation (Fig. 1) *(9)*. The CO_2RR offers numerous advantages, making it a focal point of research and development in the field of catalysis and energy conversion. This process could be seen as inspected by Natural photosynthesis, which produces organic matter and oxygen from carbon dioxide, water and sunlight, whereas respiration consumes the generated organic matter and oxygen to produce energy, water and CO_2 release.

CO_2 is a major greenhouse gas contributing to global warming and climate change and by converting CO_2 into useful chemicals and fuels, the CO_2 reduction reactions can help to mitigate the effects of climate change.

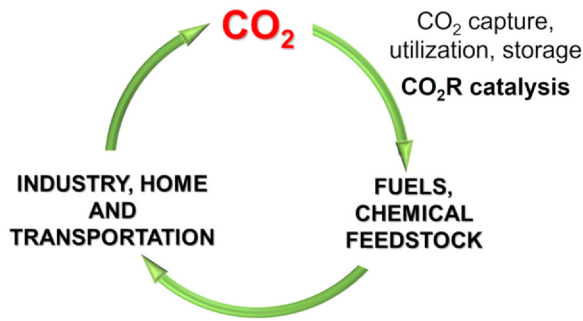

Fig. 1 Schematic representation of a closed carbon cycle by developing CO_2 capture and transformation technologies to produce chemicals and fuels. CO_2R stands for CO_2 reduction.

This process turns a problematic pollutant into a valuable resource. The conversion of CO_2, as a C_1 building block in the synthesis into fuels, such as methane, methanol, and other hydrocarbons provides a means of storing renewable energy, but also the synthesis of chemicals *(9)*. Solar and wind energy, which are intermittent in nature, can be harnessed and stored in the form of chemical bonds through CO_2 reduction (CO_2R). This stored energy can be used when renewable energy generation is low, ensuring a stable energy supply. Therefore, CO_2R reactions could enable the sustainable production of various chemicals and fuels that are conventionally derived from fossil resources. By using CO_2 as a feedstock, the chemical industry can reduce its reliance on fossil fuels, lower its carbon footprint, and promote a circular carbon economy.

However, achieving selective CO_2R presents significant challenges. Primarily, there are substantial thermodynamic and kinetic barriers that must be overcome for effective CO_2R. The formal redox potential for the one-electron reduction of CO_2 to $CO_2^{\bullet-}$ is approximately -1.9 V versus the normal hydrogen electrode (NHE at pH 7, Table 1) under standard conditions, highlighting the intrinsic thermodynamic difficulty of this process *(10,11)*. The inherent challenge in the direct one-electron reduction of CO_2 is largely due to its linear geometry and delocalized π-HOMO orbitals, paired with a highly energetic LUMO orbital. These electronic and geometric characteristics render CO_2 stable against electrophiles and resistant to one-electron reduction (Eq. 1) *(10)*. However, CO_2 readily reacts with nucleophiles such as amines or hydroxide ions, as well as with metal complexes in low oxidation states, which opens the possibility of catalytic transformations.

Table 1 Formal reduction potentials (V vs NHE at pH 7) for the water oxidation half reaction and various CO_2R reactions.

$H_2O \rightarrow O_2 + 4H^+ + 4e^-$	$E^{o\prime} = 0.84 V\ vs.\ NHE$	(1)
$CO_2 + e^- \rightarrow CO_2^{\cdot -}$	$E^{o\prime} = -1.90 V\ vs.\ NHE$	(2)
$CO_2 + 2H^+ + 2e^- \rightarrow CO + H_2O$	$E^{o\prime} = -0.53 V\ vs.\ NHE$	(3)
$CO_2 + 2H^+ + 2e^- \rightarrow HCO_2H$	$E^{o\prime} = -0.61 V\ vs.\ NHE$	(4)
$CO_2 + 4H^+ + 4e^- \rightarrow H_2CO + H_2O$	$E^{o\prime} = -0.48 V\ vs.\ NHE$	(5)
$CO_2 + 6H^+ + 6e^- \rightarrow CH_3OH + H_2O$	$E^{o\prime} = -0.38 V\ vs.\ NHE$	(6)
$CO_2 + 6H^+ + 8e^- \rightarrow CH_4 + H_2O$	$E^{o\prime} = -0.24 V\ vs.\ NHE$	(7)
$2H^+ + 2e^- \rightarrow H_2$	$E^{o\prime} = -0.42 V\ vs.\ NHE$	(8)

To effectively produce fuels through the multi-electron, multi-proton reduction of CO_2, catalysis is essential to reduce the kinetic barriers leading to the desired products *(12)*. However, the significant challenge of this process is achieving high selectivity, particularly in aqueous reaction media. In this regard, one of the main issues is the competitive hydrogen evolution reaction (HER), which often occurs alongside CO_2R. This competition arises because both CO_2R and HER involve proton-coupled electron transfer steps. In water, the abundance of protons can lead to a preferential reduction of protons to hydrogen gas (H_2), thereby decreasing the efficiency and selectivity of CO_2R to desired carbon-based products. Thus, designing catalysts that can selectively reduce CO_2 while suppressing HER is crucial for advancing efficient and practical CO_2R technologies.

Heterogeneous catalysts are widely regarded as the most viable option for large-scale CO_2R in aqueous environments *(13)*. These catalysts can produce a variety of products, ranging from CO to CH_4 (Eqs. 2–7, Table 1) and even multi-carbon compounds (C_{2+}). However, achieving high selectivity for specific products remains a significant challenge. Furthermore, when performing CO_2R reactions in water, the hydrogen evolution reaction (HER) often competes with the desired reaction, making selectivity even more difficult to control (Eq. 8, Table 1).

On the other hand, homogeneous catalysts typically produce two-electron reduction products like CO and formic acid *(14)*. Despite this limitation, recent advancements have shown that well-defined molecular complexes can also facilitate the reduction of CO_2 to products beyond two-electron reductions. Additionally, homogeneous catalysts exhibit promising durability and catalytic performance when immobilized on supports *(15–19)*. Their well-characterized structures, uniform catalytic sites, and solubility enable detailed mechanistic studies using spectroscopic techniques. Recent research has made significant progress in understanding the CO_2R mechanisms, identifying key steps and the thermodynamic and kinetic factors that influence the reaction. Although these studies are challenging, they are crucial for developing faster and more selective catalysts *(20)*. Typically, insights are gained through a combination of electrochemical studies, spectroscopic analysis, and computational modeling.

The development of metal complexes as catalysts for CO_2R is pivotal for advancing this technology. Metal complexes offer several distinct advantages, including the ability to finely tune catalytic properties by modifying both the metal center and the ligands. This tunability allows researchers to optimize catalytic activity, selectivity, and stability for the specific CO_2R reactions. Achieving high selectivity for desired products is one of the significant challenges in CO_2R, alongside CO_2 activation. Metal complexes can be tailored to favor specific reaction pathways, thereby minimizing the formation of unwanted by-products. This high selectivity is crucial to makeCO_2R processes efficient and economically viable. More importantly, the well-defined structure of metal complexes facilitates detailed mechanistic studies. Understanding the mechanisms of CO_2 activation and reduction at the molecular level is crucial for the rational design of more effective catalysts. Metal complexes serve as excellent model systems for such studies, offering insights that can be translated into improved catalytic systems. By advancing the design and understanding of metal complexes for CO_2R, we can realize the full potential of this technology.

To fulfill the sustainability criteria, the CO_2RR must be coupled with an oxidation reaction. Therefore, the selected sacrificial oxidant must be highly available and inexpensive, and the generated oxidized species should be environmentally benign. In this regard, the water oxidation reaction (WOR) is an ideal candidate to pair with the CO_2RR. This approach emulates natural photosynthesis, as artificial

photosynthesis. However, this approach poses several challenges, such as the highly endergonic nature of the overall reaction, the need for CO_2R catalysts to be stable, active, and selective in water, and the necessity for compartmentalization of the reduction and oxidation reactions is needed, an implementation of catalytic systems where both oxidation and reduction reactions. Implementing catalytic systems where both oxidation and reduction reactions can exchange reductive/oxidative equivalents in a synchronized manner requires complex architectures like nanoparticulated systems or reactors.

Although both semi-redox reactions (CO_2R and WO) must operate together, the individual reaction can be studied separately for faster catalyst evolution and deeper mechanistic understanding. Nevertheless, mere catalysts development is not sufficient. A holistic approach should be considered, addressing energy harvesting, operation in practical reaction media at sufficient concentration, durability, and integration into devices. There is still a gap in knowledge regarding the efficient implementation of a full catalyst system for artificial photosynthesis and catalysts are not yet ready for industrialization. Further understanding of the reaction mechanisms and catalyst design to enhance activity, control selectivity, and increase stability is needed to obtain practical catalysts.

Given the endergonic nature of the overall process for CO_2R to fuels and chemicals, electrochemical and photochemical transformations hold promise for ensuring a suitable energy supply by utilizing renewable sources like sunlight or wind. Electrochemistry and photochemistry are thus central to achieving CO_2RR, requiring specific considerations for studying the field and developing catalysts.

This review explores recent advancements in catalyst development for CO_2R, particularly focusing on mechanistically informed approaches using well-defined homogeneous cobalt complexes. The review is organized into two main categories based on the ligands utilized: (i) non-heme, imino- and aminopyridine complexes and (ii) porphyrin and phthalocyanine complexes. In addition, in the review is also highlighted the products generated from CO_2R regarding the number of electrons utilized: those involving two-electron reductions (producing CO and formic acid) and those yielding products from more-than-two-electron reductions (such as CHOH, CH_3OH, and CH_4). This structure helps to highlight common aspects across different catalysts aimed at achieving specific and selective products.

1.1 General considerations on electrochemistry and photochemistry for CO_2 reduction

1.1.1 Electrochemical CO_2 reduction

The electrochemical reduction of carbon dioxide (CO_2) has garnered significant attention due to its potential to convert CO_2 into valuable fuels and chemicals at industrially relevant current densities. This process, known as the electrochemical CO_2 reduction reaction (CO_2RR), occurs at the cathode of an electrochemical cell, where CO_2 is reduced by electrons provided by an external power source. The choice of catalyst is paramount to achieving efficient CO_2R, with cobalt complexes containing nitrogen ligands emerging as promising candidates due to their unique properties. The catalyst must efficiently react with CO_2 and facilitate its reduction through multiple electron/proton transfers.

To evaluate the performance of electrochemical CO_2R catalysts, several metrics are commonly used. Electroanalysis, in particular cyclic voltammetry (CV), together with chronoamperometry (CA or controlled potential electrolysis (CPE)), of the metal complex in solution in the absence and in the presence of the substrate, facilitates the evaluation and catalyst benchmarking in terms of Faradaic efficiency (FE), turnover number, maximum turnover frequency (TOF_{max}), and overpotential (η) *(21)*. Faradaic efficiency (FE) measures the efficiency of electron utilization towards the desired product. The FE is calculated as the percentage of the ratio between the charge associated with the product formation (P) and the total charge passed during the experiment (Q) (Eq. 9). The turnover number (TON) indicates the number of catalytic cycles and the TON of a catalyst can be obtained by measuring the amount of product generated per catalyst unit during an exhausting control potential electrolysis (Eq. 10). Turnover frequency (TOF) TONs per unit time, reflecting the catalyst's activity (Eq. 11) and it is also the observed kinetic rate constant (k_{obs} in s^{-1}) for the catalytic reaction, which typically it can be expressed as the linear dependence on the reactant concentration to the reaction order and the catalytic rate constant (Eq. 12). Nevertheless, it depends on the mechanism and should be analyzed case by case. Minimizing the applied potential required to drive the reduction, known as the overpotential (η), enhances energy efficiency. The overpotential is the extra potential required beyond the thermodynamic potential to drive the reduction reaction (Eq. 13). Stability can be assessed through long-term electrolysis experiments to determine the catalyst's durability under operational conditions or by accelerated stability test by exposing the

catalyst phase to severe operative conditions. Moreover, another important parameter is catalyst selectivity of favoring one product over the other possible ones (S, Eq. 14). A selective catalyst should preferentially produce a desired product such as carbon monoxide (CO), formic acid (HCOOH), methane (CH_4), or methanol (CH_3OH), while minimizing by-products.

$$FE\,(\%) = \frac{P(C)}{Q(C)} \cdot 100 \tag{9}$$

$$TON = \frac{P(mol)}{Cat\,(mol)} \tag{10}$$

$$TOF = \frac{TON}{t} \tag{11}$$

$$TOF_{\max} = k_{obs} = k_{cat}\,[A^0]^n \tag{12}$$

$$\eta = E^{o\prime}{}_{A/B} - E_{app} \tag{13}$$

$$S\,(\%) = \frac{Selected\ Product}{\sum All\ products} \tag{14}$$

A technique to highlight due to its capacity to shed light on the electrochemical reaction mechanisms is the spectroelectrochemistry (SEC). In particular, SEC is a powerful technique for investigating the electrocatalytic CO_2R mechanism on the electrode surface under working conditions. In SEC experiments, information about the reaction is obtained simultaneously from steady-state in-situ electrochemical, and spectroscopic measurements. Infrared (IR) spectroscopy coupled with electrochemistry (IR-SEC) enables the detection of potential CO_2R intermediates, such as metal carboxylates and carbonyls. Moreover, IR vibration is sensitive to the chemical environment and the metal oxidation state. Moreover, other techniques such as ultraviolet and visible light spectroscopy (UV-Vis) and Raman spectroscopy are also very informative *(22)*.

In addition to catalysts, both electrodes and the electrochemical cells are also crucial for the study of catalysts and the effective implementation of CO_2R processes. Various types of electrochemical cells are employed for CO_2R, each offering distinct advantages (Fig. 2). Flow cells, SEC-cells and H-cells are commonly used, with flow cells providing continuous operation and improved mass transport, while SEC-cells and H-cells are simpler and more suitable for mechanistic studies.

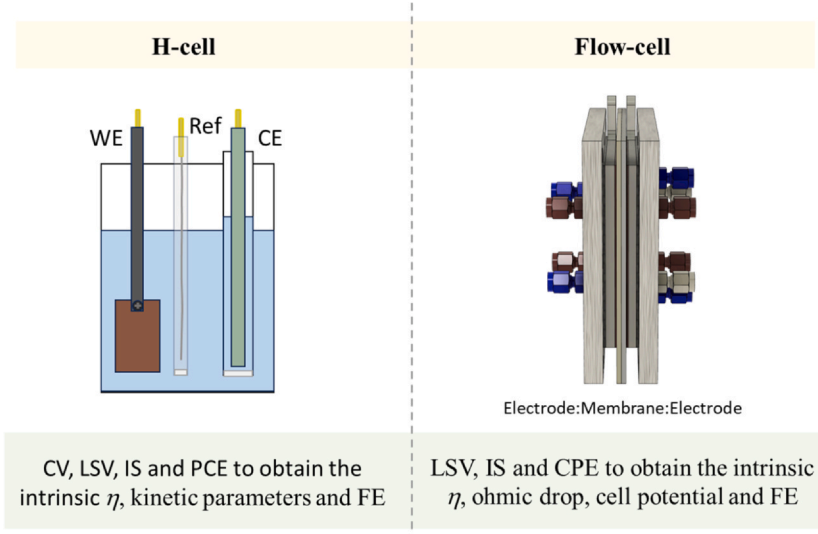

Fig. 2 General scheme of electrochemical cells and their features.

1.1.2 Photochemical CO_2 reduction

Photochemical CO_2R leverages light energy to convert CO_2 into valuable chemicals and fuels. The efficiency of this process hinges on several key aspects, beginning with the absorption of light. Efficient light absorption, particularly in the visible spectrum, is critical for initiating effective photochemical processes. This is because the absorbed light energy must be converted into chemical energy through a series of subsequent steps. The generation and separation of electron-hole pairs must also be efficient to prevent recombination, ensuring that reductive equivalents are available. Additionally, the integration of photocatalysts or photosensitizers with CO_2R catalysts is essential to facilitate efficient electron transfer and subsequent product formation, thus minimizing energy losses and enhancing overall energy efficiency. In this regard, it is important to match the thermodynamics and kinetics of the electron transfer processes.

Photocatalytic systems designed for CO_2R typically involve a light-absorbing material, known as a photosensitizer, coupled with a catalyst. Key components of these systems include photosensitizers, which can be molecules or materials that absorb light and generate excited states or electron-hole pairs. Common examples of photosensitizers are semiconductor materials like TiO_2 and molecular photosensitizers such as

ruthenium, iridium or copper complexes. The photogenerated electron is then transferred to the CO_2 reduction catalyst, which initiates the reduction process. The catalyst activates and reduces CO_2 through a series of proton-coupled electron transfer steps, ultimately leading to the formation of desired reduction products. The efficient photoinduced electron transfer to the CO_2R catalyst is crucial for the process, necessitating effective integration between the photosensitizer and the CO_2R catalyst to facilitate electron transfer and product formation.

To evaluate the performance of photochemical CO_2R systems, several metrics are commonly used. Quantum efficiency (QE) is a critical metric that measures the number of CO_2 molecules reduced per photon absorbed. Specifically, it is defined as the ratio of the number of molecules of CO_2 reduced (or any target product formed) to the number of photons absorbed by the photosensitizer or photocatalyst. This metric reflects the effectiveness of the photochemical process in utilizing light energy to drive the desired chemical reaction. Turnover number (TON), as in the case of electrochemical CO_2R, is another important metric, indicating the number of times the catalyst can turn over (i.e., reduce CO_2) before deactivation. Stability, the ability of the photocatalytic system to maintain activity over extended periods under illumination, is also a crucial performance metric, as it determines the long-term viability and practical applicability of the system.

$$QE\,(\%) = \frac{n^{*}P(mol)}{h\nu\,(mol)} \cdot 100 \tag{15}$$

Light sources play a crucial role in photochemical CO_2R systems. For fundamental studies aimed at understanding the underlying mechanisms rather than optimizing solar-to-fuel efficiency, the primary requirements are precise control of light intensity and temperature. Controlled light

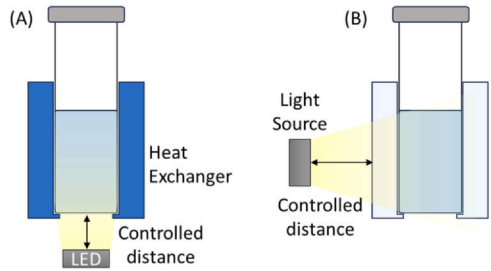

Fig. 3 Schematic representation of irradiation sources and setups.

intensity ensures that the photon flux reaching the photocatalyst is consistent, allowing for reproducible experimental conditions and accurate mechanistic studies (Fig. 3). Temperature control is equally important, as reaction kinetics and catalyst stability can be significantly influenced by temperature variations. Therefore, maintaining a stable temperature is essential for obtaining reliable data and understanding the intrinsic properties of the photocatalyst.

For studies focused on optimizing solar-to-fuel efficiency, solar light simulators have become indispensable. These simulators are designed to mimic the spectral distribution and intensity of natural sunlight, providing a standardized and controlled environment for evaluating the performance of photocatalytic systems under conditions that closely resemble real-world solar irradiation. Solar light simulators enable researchers to accurately assess the efficiency of converting solar energy into chemical energy, facilitating the comparison of different photocatalysts and system configurations.

In the context of solar-to-fuel efficiency calculations, the use of solar light simulators ensures that the experimental conditions reflect the variable nature of sunlight, including changes in intensity and spectrum throughout the day. This is crucial for determining the practical viability of photocatalytic systems for large-scale applications. Accurate solar-to-fuel efficiency measurements require that the light source replicates the solar spectrum as closely as possible, typically adhering to standard solar irradiance models such as AM1.5 (Air Mass 1.5), which represents the solar spectrum at the Earth's surface with the sun at a 48.2° angle above the horizon.

Nevetheless, LEDs are also usefull ligh sources to evaluate the catalytic activity of catalysts, and mechanistic studies, since its light emission is very stable, there is a large collection of wavelenghts avaliable and are economical facilitation the implementation of high-throughput photoreactors *(23)*.

1.2 Molecular design of cobalt complexes with nitrogen ligands

Molecular catalysts, particularly those based on transition metals like cobalt, have shown great promise for CO_2R due to their tunable coordination environments and well-defined active sites. Design strategies for cobalt complexes focus on enhancing catalytic efficiency, selectivity, and stability. One approach involves modifying the ligands by introducing electron-donating or withdrawing groups to fine-tune the electronic properties of the cobalt center. Modulating its redox properties and influencing its ability to activate and reduce CO_2 and is essential for optimizing the catalyst's reactivity and selectivity. Another strategy involves incorporating

functional groups that provide hydrogen bonding or electrostatic interactions, which can stabilize intermediates and transition states, thereby boosting catalytic performance. Additionally, precise localization of Lewis bases (like secondary amine groups) around the cobalt center can be tailored to optimize interactions with CO_2 and intermediates, acting as proton relays, facilitating proton transfer to the active site and enhancing the protonation steps crucial for CO_2R. In addition, using multidentate ligands that strongly coordinate the metal center can create a more rigid and stable coordination environment, enhancing the overall activity and stability of the catalyst *(12,20,24)*.

Each metal complex offers unique advantages and faces specific challenges in the context of CO_2R. For instance, manganese tricarbonyl complexes with polypyridyl ligands such as bipyridine and its derivatives can stabilize various oxidation states (I, 0, -I), which are notable for their low overpotential in water. Recent studies have shown promising control over the selectivity for specific products, such as CO and formic acid, against hydrogen evolution. However, these complexes present limited stability and the formation of off-cycle products. Nevertheless, remarkable stability and turnover frequencies (TOFs) have been observed in specific cases of electrode functionalization *(12,19,20,24,25)*.

Nickel complexes often use bipyridyl, N-heterocyclic carbene (NHC), and cyclopentadienyl ligands, which provide a stable coordination environment for the nickel center. Ni complexes with appropriate ligand modifications can achieve high TOFs and selectivity for CO_2R to CO. However, achieving high selectivity for a single product can be challenging, as Ni complexes may produce a mixture of CO and hydrogen depending on the reaction conditions *(12,13,20)*.

Iron is highly abundant, inexpensive and biocompatible, making Fe complexes appealing for CO_2R. Iron complexes frequently utilize porphyrins, phthalocyanines, and polypyridyl ligands, which mimic natural enzyme active sites and provide a stable environment for Fe. These complexes exhibit high selectivity for specific products, such as CO, formic acid, or methane, depending on the ligand design and reaction conditions.

Cobalt complexes have several key features that make them particularly interesting for CO_2R. Cobalt complexes with nitrogen-based ligands offer a unique combination of tunable electronic properties, enhanced proton transfer mechanisms, high selectivity, stability, cost-effectiveness, and sustainability. These features make them highly suitable for the electrochemical and photochemical reduction of CO_2. Extensive studies with

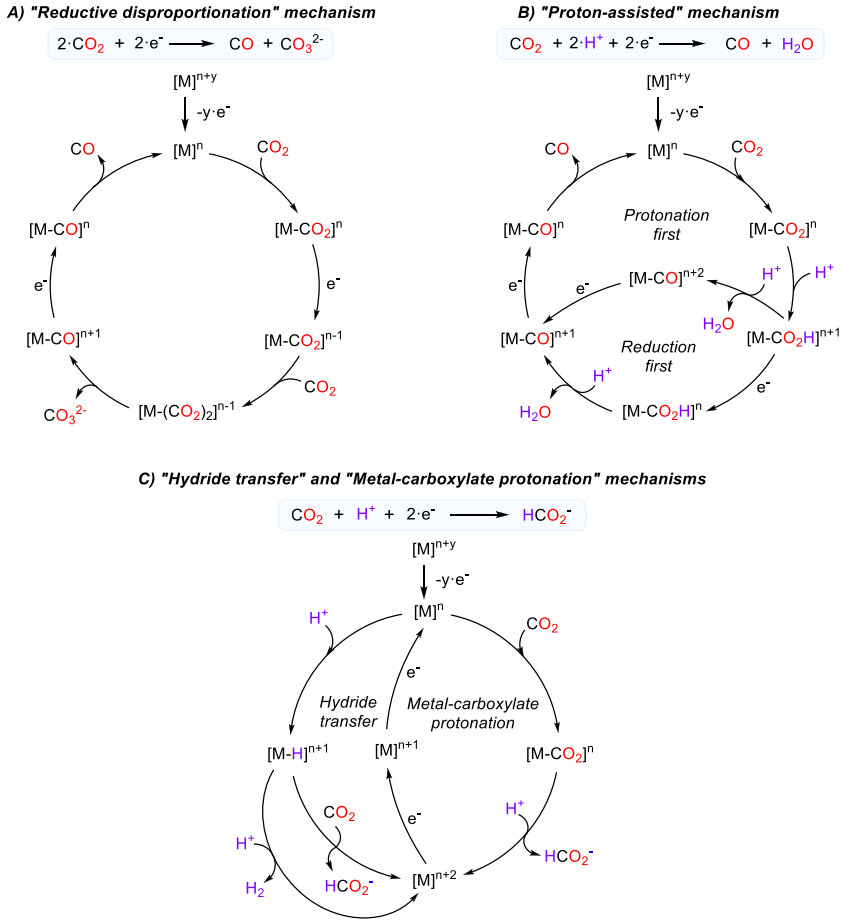

Fig. 4 Overview of the two-electron reduction catalytic cycles for the "reductive disproportionation" mechanism (A), the "proton-assisted" CO_2R to CO (B) and the "hydride transfer" and "metal-carboxylate protonation" mechanisms for the CO_2R to formate and hydrogen (C).

polypyridyl, aminopyridyl, and macrocyclic ligands have demonstrated their versatility. These ligands can be easily modified to tune the electronic and steric properties of the cobalt center, allowing for deep mechanistic investigations. Generally, Co complexes demonstrate good selectivity for CO or formic acid production. Remarkably, cobalt complexes have shown that under certain conditions, methanol and formaldehyde are accessible products. Although long-term stability can be an issue, and some Co complexes may deactivate over prolonged electrolysis, studies with

phthalocyanine and covalent organic frameworks have shown stabilities over 100 h. In this regard, this review focuses on cobalt complexes, as an earth-abundant and cost-effective metal, with nitrogen-based ligands. Nitrogen-based ligands, such as aminopyridines, polypyridines, porphyrin and phthalocyanine ones, because can stability of the catalysts in various oxidation states of cobalt, are synthetically versatile, allowing fine tuning of electronic, steric and introducing second shell interactions.

1.3 Mechanistic pathways

The general CO_2 reduction reaction (CO_2RR) mechanisms with well-defined metal complexes typically begin by reducing the metal site to a sufficiently low oxidation state ($[M]^n$) that can react directly with CO_2 ($[M\text{-}CO_2]^n$) or with the aid of protonation to produce an intermediate ($[M\text{-}CO_2H]^{n+1}$, Fig. 4). In the absence of a Brønsted acid, a reductive disproportionation mechanism is possible (Fig. 4A), where two CO_2 molecules are reduced by two electrons to yield CO and carbonate. The second CO_2 molecule acts as a Lewis acid to promote the O abstraction breaking the C–O bond forming CO_3^{2-} *(26)*. When there is a high concentration of protons, the reduced intermediate ($[M]^n$) can also be protonated to produce a metal hydride intermediate ($[M\text{-}H]^{n+1}$). Controlling this divergent step is crucial for selectivity.

When the metal site reacts with CO_2, it leads to the formation of CO via the C–O cleavage pathway, via consecutive single-electron transfer (SET) and protonation steps. The specific order of protonation and electron transfer steps before the C–O cleavage depends on the nature of the metal, the ligand, and the reaction conditions. In the presence of a Brønsted acid, the $[M\text{-}CO_2]^n$ complex can undergo protonation to form the intermediate $[M\text{-}CO_2H]^{n+1}$ (Fig. 4B). A subsequent protonation step can induce the cleavage of the C–O bond, resulting in the formation of a metal-carbonyl species $[M\text{-}CO]^{n+2}$. This sequence of events is referred to as the "protonation first" mechanism. Alternatively, if the $[M\text{-}CO_2H]^{n+1}$ intermediate is reduced before the second protonation, the process follows the "reduction first" pathway. In general, electron-rich complexes tend to favor the "protonation first" mechanism.

This preference arises from the increased basicity of the metal-carboxylate adduct. Conversely, the "reduction first" mechanism is more likely to occur with electron-deficient complexes *(25)*. Regardless the path, the $[M\text{-}CO_2H]^n$ intermediate triggers the C–O bond cleavage, producing $[M\text{-}CO]^{n+1}$ and a water molecule *(25)*. The carbon-oxygen bond cleavage is critical

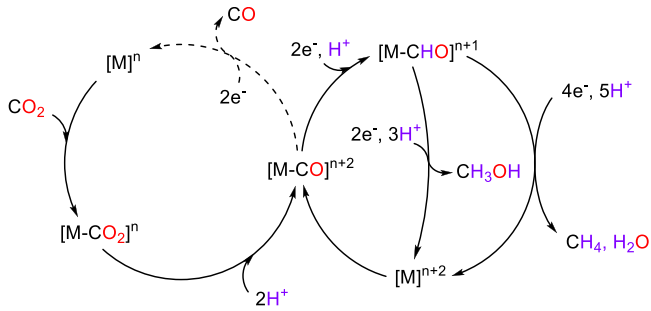

Fig. 5 Pathways for consecutive reduction and protonation leading to higher-order CO_2R products such as formaldehyde, methanol, and methane.

and usually is identified as the rate-determining step (rds) *(25,27–34)*. This pathway results in the formation of the common metal carbonyl intermediate, a subsequent reduction produces the CO release from the reduced metal-carbonyl intermediate ($[M\text{-}CO]^n$, Fig. 4B), which can also have a significant kinetic barrier since metal carbonyls could be thermodynamic sinks *(35,36)*.

Protonation of the metal center to yield a metal hydride can lead to H_2 production through further protonation (Fig. 4C). From the metal hydride, two different products can be formed: H_2 through protonation of the metal hydride, or formate ($HCOO^-$) if the metal hydride reacts with CO_2 (Fig. 4C). Controlling the selectivity between hydride protonation and hydride transfer to CO_2 is challenging and usually relies on modifying the reaction conditions. Reducing the availability of protons enhances selectivity toward formate formation; however, this typically results in formate, not formic acid, under highly basic conditions, which diminishes the reaction's overall appeal.

Accessing CO_2R products beyond two-electron reductions requires the reduction of intermediate species such as metal carbonyls, or products like CO or HCO_2^- (Fig. 5). In particular, the consecutive reduction and protonation of metal carbonyls can yield metal acetyl intermediates ($[M\text{-}CHO]^{n+1}$), which, depending on the protonation and reduction steps, could produce formaldehyde (HCOH), methanol (MeOH) or methane (CH_4). A lack of mechanistic understanding still limits control over selectivity. In this regard, cobalt complexes have the advantage of allowing CO_2R to MeOH with high selectivity, and although with lower selectivity, also HCOH. Producing C_2 products is even more challenging, and the reaction mechanisms that could produce them are still under debate.

2. Complexes based on heme ligands

2.1 Porphyrine and porphine Co complexes

Metal porphyrins are considered one of the most promising families of molecular catalysts for selective electrocatalytic CO_2R to CO. Iron porphyrins, in particular, have been the focus of extensive experimental and theoretical studies conducted by Saveant, Costentin, and Robert. In addition to iron, cobalt porphyrins have been also widely explored for electrochemical CO_2R to CO, showing promising results especially when integrated in supramolecular or heterogeneous catalytic systems *(35,24,37)*.

The first report of a cobalt porphyrin for electrocatalytic CO_2R was published in 1979 by Toshima and coworkers. They examined the catalytic activity of metal-free, cobalt, iron and copper mesotetracarboxyphenyl porphyrin (**MTCPP**) and tetraphenylporphinesulfonate porphyrins (**MTSPP**) for electrocatalytic CO_2R using current-potential measurements on a Hg(Pt) electrode in aqueous solutions. **CoTCPP** and **CoTSPP** (Fig. 6, respectively) showed to be effective catalysts, producing formic acid as the reduction product, while metal-free, iron, and copper porphyrins showed no activity. Although **CoTCPP** and **CoTSPP** exhibited similar catalytic effects to tetrasulfonated cobalt phthalocyanine (**CoTSP**), they were less active (*see cobalt phthalocyanine section below*), suggesting that both the central metal ions and the ligands influence catalytic activity, with cobalt complexes being uniquely effective among the porphyrins tested *(38)*. Later, in 1998, Fujita and coworkers, reported that, in a comparable manner to the iron tetra-phenylporphyrin (**FeTPP**), the cobalt analog (**CoTPP,** Fig. 6) could catalyze the reduction of CO_2 to CO and formate, either under photochemical conditions using triethylamine as electron donor, as well as, under electrochemical conditions, both using acetonitrile as solvent. However, as a homogeneous catalyst in organic media, **CoTPP** required a larger overpotential (>1 V) due to the need to form the doubly reduced $[Co^0(TPP)]^{2-}$ species (Fig. 5). To mitigate this, the authors developed the fluorinated derivatives of the **CoTPP** bearing more electron-withdrawing groups such as -F and $-CF_3$ (Fig. 6), which were able to catalyze CO_2R at less negative potentials, improving the overpotential *(39)*. However, the authors also tested water-soluble cobalt porphyrins Co tetrakis(4-sulfonatophenyl)porphyrin (**CoTSPP**), Co tetrakis(N-methyl-4-pyridyl)porphyrin (**CoTM4PyP**), Co tetrakis(N-methyl-3-pyridyl)porphyrin (**CoTM3PyP**), Co tetrakis(Nmethyl-2-pyridyl)porphyrin (**CoTM2PyP**), and Co tetrakis(N,N,Ntrimethyl-4-

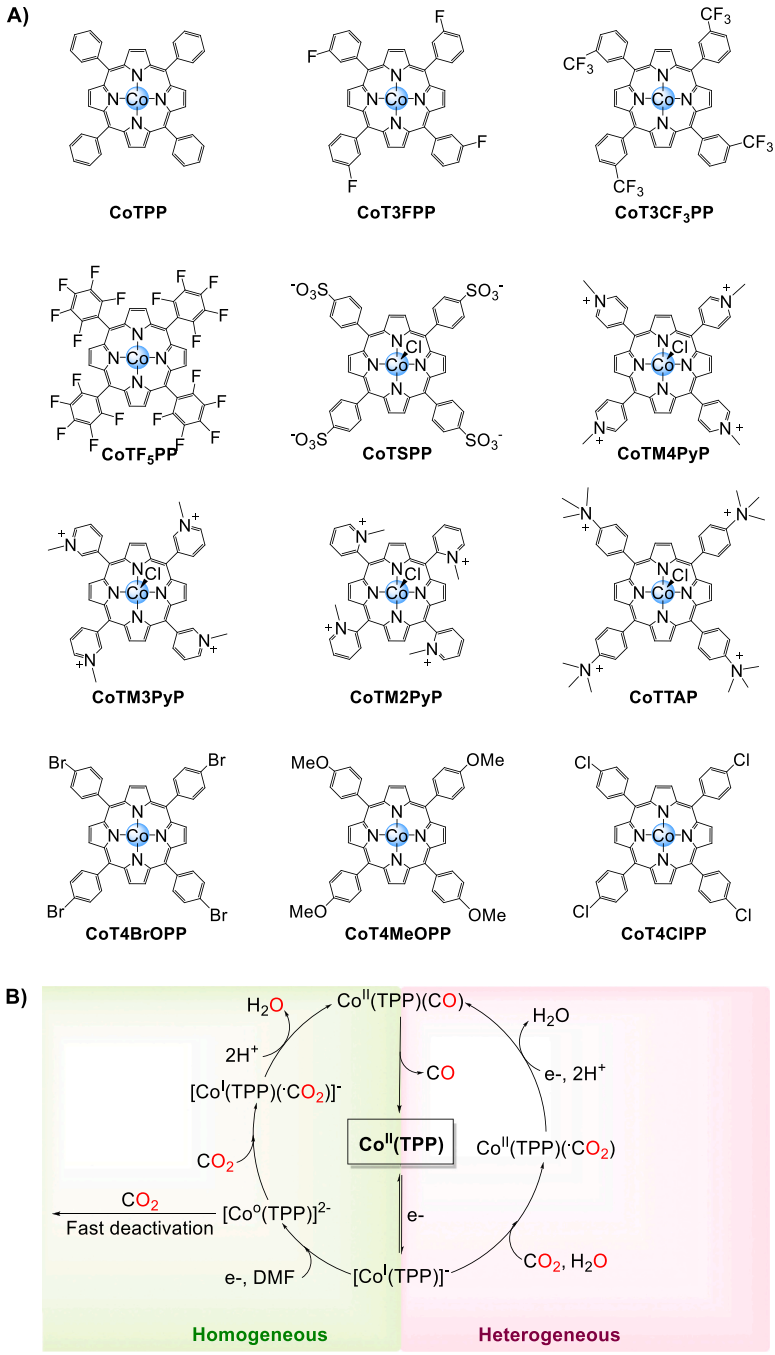

Fig. 6 (A) Representation of the **CoTPP** and its derivative complexes with the different inductive and electrostatic effects for electrocatalytic CO_2R *(40,45)*. (B) Proposed mechanism for CO_2 electroreduction catalyzed by **CoTPP** under homogeneous and heterogeneous conditions *(46)*.

aminophenyl)porphyrin (**CoTTAP**) gave the lowest yields of reduced products, since ring reduction decreased the efficiency for CO_2R *(40)*. Therefore, the strategic tuning of ligands in cobalt porphyrins allows for a design approach akin to that used with iron-based porphyrins. Recently, Manthiram and colleagues demonstrated how peripheral functionalization of the aromatic groups in cobalt porphyrins influences CO_2R with **CoTSPP**, **CoTM4PyP**, **CoTM3PyP** and **CoTM2PyP** (Fig. 6). Specifically, incorporating cationic substituents into the periphery of cobalt porphyrins enhances the rates of CO_2R. This increase in catalytic activity is attributed to the ability of these modified porphyrins to stabilize the [Co-(CO_2)] complex *(41)*. Furthermore, immobilizing **CoTAP** onto reduced graphene oxide (rGO) results in a highly stable film, capable of electrocatalytically reducing CO_2 to CO and formic acid with 45% efficiency each in an aqueous electrolyte at an overpotential of 590 mV *(42)*. The proposed mechanism for CO_2R follows a similar pathway as previously reported cases *(43,44)*.

Additionally, **CoTPP** analogs are very efficient catalysts once immobilized on conductive carbon-based electrodes, such as gas diffusion electrodes (GDE) *(47)* and pyrolytic graphite (PG) *(43)*. In this regard, Sakata et al. investigated the electrochemical reduction of CO_2 at **CoTPP** supported GDEs under both atmospheric and high-pressure conditions, showing that increasing the CO_2 pressure significantly enhances the electrocatalytic activity of **CoTPP** supported GDEs up to 97.4%. The study also highlights that the reduction potentials shift positively with increased CO_2 pressure, indicating an improved catalytic performance due to higher CO_2 concentration in the electrolyte *(47)*.

Following another approach, Yamamoto and coworkers explored the efficiency of cofacial dinuclear metalloporphyrins prepared through the self-assembly of cationic (**CoTM4PyP**) and anionic porphyrins (**CoTSPP**, Fig. 7) for electrocatalytic CO_2R in aqueous DMSO at −1.8 V vs. Ag/Ag^+. The self-assembly led to a significant enhancement of the reduction process and improved conversion rates of CO_2 to CO and formic acid. The study demonstrated that the cofacial arrangement of the metalloporphyrins plays a crucial role in facilitating electron transfer and stabilizing intermediates, resulting in higher catalytic activity compared to mononuclear counterparts. Moreover, cyclic voltammetry (CV) studies showed that the CO_2R was primarily attributed to the Co(I) state of **CoTM4PyP**, despite the complexity of determining the exact oxidation state due to multiple ligand-based reductions. Moreover, the study

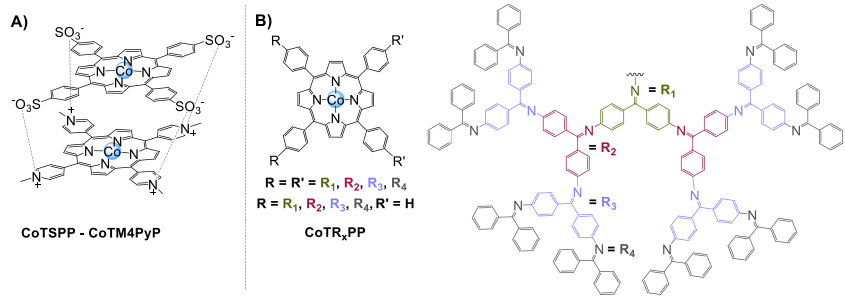

Fig. 7 Representation of the (A) cofacial dinuclear porphyrin complex **CoTSPP-CoTM4PyP**, and (B) the **CoTR$_x$PP**-derivative dendrimer.

concluded that **CoTSPP** acted as an "electron mediator," facilitating electron transfer to the catalytic metal. Additionally, the catalytic activity was not limited to cobalt, as similar results were achieved with copper complexes *(48)*.

The study investigates the catalytic activity of phenylazomethine dendrimers with a **CoTPP** cobalt porphyrin core for the reduction of CO_2 in the presence of strong Lewis acids like lanthanide trifluoromethanesulfonate. The dendrimer catalysts demonstrated enhanced catalytic behavior compared to traditional cobalt complexes, initiating the reduction process at a more positive potential of −1.3 V, which is 1.1 V higher than the conventional cobalt tetraphenylporphyrin (**CoTPP**) catalysts due to improved multi-electron transfer facilitated by the coordinated metal ions. The generation number of the dendrimers influenced the catalytic efficiency, with an optimal generation observed at three (**CoTR$_3$PP**, Fig. 7). Higher generations resulted in decreased activity due to steric hindrance around the catalytic center. A non-symmetric dendrimer design with a pocket shape improved accessibility to the core and catalytic performance, enhancing the catalytic efficiency, emphasizing the importance of structural modification of the ligand environment around the metal center to enhance CO_2R *(49)*.

In another example, Daasbjerg and coauthors compared the electrocatalytic CO_2 reduction of **CoTPP** under homogeneous and heterogeneous conditions *(46)*. Under homogeneous conditions employing DMF as the solvent, **CoTPP** yielded poor catalytic activity (0.17 mA·cm^{-2}) with low product selectivity for CO (50%) and formation of H_2 (2%), formate (4%), acetate (2%), and oxalate (0.4%) at a high overpotential (1.02 V). The low activity in organic solvent was associated to the need for the formation of the catalytically active doubly reduced $[Co^0TPP]^{2-}$ species at

unfavorable overpotentials for CO_2R, causing severe catalyst deactivation during long-term electrolysis. However, the heterogenized molecular catalyst upon immobilization of **CoTPP** on CNTs allowed the selective conversion of CO_2 to CO with 91% Faradaic yield in aqueous solvent and at a lower overpotential (550 mV) than the homogeneous system. The difference in reactivity and selectivity between aqueous and non-aqueous conditions was attributed to the role of water in stabilizing the anionic $[Co(TPP)(CO_2)]^{2-}$ adduct through solvation, increasing the reaction rate of the catalytically active $[Co^{I}(TPP)]^{-}$ species reacting with CO_2 (Fig. 6). These results were in line with DFT mechanistic studies *(44,50)*. Moreover, the heterogenization process significantly enhanced the catalyst's stability, resulting in a 300-fold increase in activity (1118 TON_{CO}). This clearly demonstrates the critical role of the support material in heterogeneous catalysis *(51)*.

In addition to catalyst-support interactions, pH is crucial in controlling selectivity in CO_2R. For instance, Fukuzumi et al. reported a **Co^{II} chlorin** (Fig. 8) complex immobilized on MWCNTs that reduced CO_2-to-CO with 89% of FE at low pH under electrochemical conditions *(52)*.

Additionally, a recent study on Co protoporphyrin (**CoPP**) immobilized on cemented phosphogypsum (PG, **CoPP**/PG) showed that small amounts of CH_3OH and CH_4 can be produced along with CO at moderate overpotentials (~500 mV), with product distribution highly dependent on pH *(53)*. At pH 3, CO is the major product with a FE of around 40%, and CH_4 (FE < 0.5%) is produced at less negative potentials than HER. At pH 1, H_2 dominates, with FEs for CO and CH_4 below 1%. Despite low yields, the FE for CH_4 is slightly higher at pH 1 due to fast CO reduction to CH_4 under these conditions. This pH-dependent behavior aligns with the DFT mechanism reported by the Koper group for Co

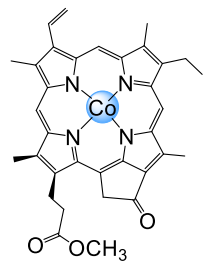

Co(II) Chlorin

Fig. 8 Representation of the Co^{II} chlorin reported by Fukuzumi and coworkers *(52)*.

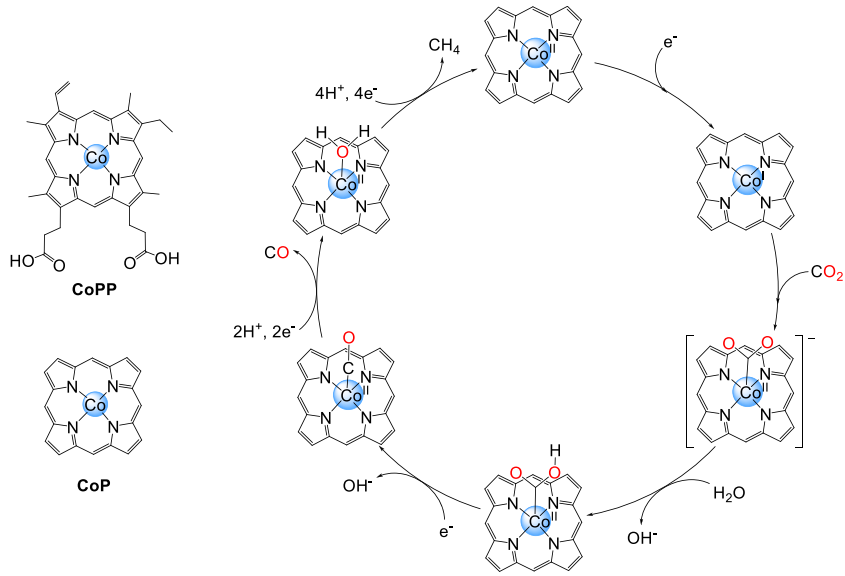

Fig. 9 Representation of **CoPP** and **CoP** complexes and the proposed DFT mechanism for CO_2R to CH_4 *(44)*.

porphine (**CoP**), where CO_2 binding by the catalytically active $[Co^{I}(P)]$ species forms $[Co(P)(CO_2)]^{-}$, followed by electron transfer to create a catalyst-bound $CO_2^{\bullet-}$ radical anion species $[Co(P)(CO_2^{\bullet-})]^{-}$. This radical acts as a strong Brønsted base, abstracting a proton by a water molecule to form $[Co(P)(CO_2H)]^{0}$, which can release CO or reduce it further to CH_4 via concerted PCET steps (Fig. 9) *(44)*. In another study, Yao et al. also investigated a **CoP** system and suggested that the proton required for $[CoP(CO_2H)]^{-}$ formation does not originate from the solution but is held by the pyrrole ligand at acidic pH values (<6.94). This results in an increased local proton concentration near the active center and enhanced catalysis *(54)*. The Koper group also explored the effect of the pH in electrocatalytic CO_2R by Co porphyrin complexes, exploring the formation mechanism of carboxylate adducts in CO_2 electroreduction to CO catalyzed by, focusing on concerted and sequential proton-coupled electron transfer (PCET) pathways. Their findings reveal two distinct subpathways: concerted proton-electron transfer (CPET), commonly associated with solid-state catalysts, and sequential proton-electron transfer (SPET), typically linked to molecular systems. Computational studies identified specific pH thresholds for the formation of $[Co–CO_2H]$ species by Co porphyrin

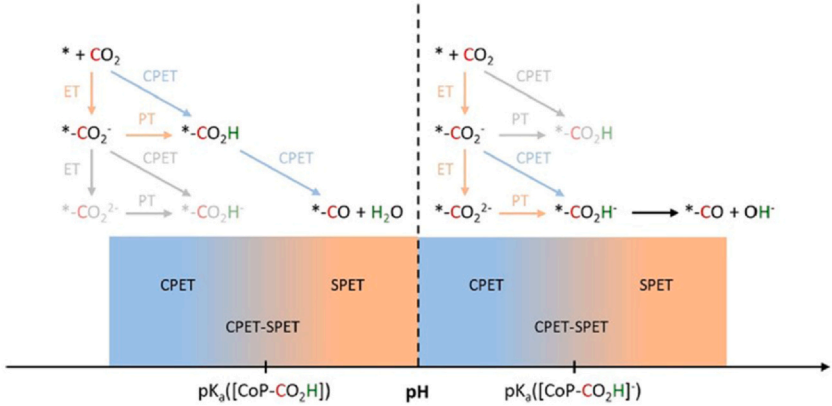

Fig. 10 Representation of the proposed dominant pH-dependent mechanisms for the formation of the carboxylate intermediate as proposed by Koper et al. (PT=proton transfer, ET=electron transfer, CPET=concerted proton-electron transfer, SPET=sequential proton-electron transfer) *(55)*. *Reprinted with permission from Göttle, A. J.; Koper, M. T. M. Chem. Sci.* ***2017****, 8, 458–465, Copyright 2017 Royal Society of Chemistry.*

complexes during electrocatalytic CO_2R, indicating a transition from CPET to a mixed CPET–SPET regime is possible in the vicinity of pH ~ 3.5 (which corresponds to the pK_a of the hydroxycarbonyl species [Co–CO_2H]), even in homogeneous systems. The latter agrees with the observed increase in the CO_2R-to-CO FE at pH 3, supporting the importance of the $[Co–CO_2]^-$ intermediate (Fig. 10) *(53)*. At slightly higher pH levels, the formation of the neutral carboxylate adduct [Co–CO_2H] is unlikely, favoring the formation of the anionic carboxylate adduct $[Co–CO_2H]^-$ instead, formed via a CPET pathway from $[Co–CO_2]^-$ at pH < 8.6 (the pK_a of $[Co–CO_2H]^-$). At pH ≥ 8.6 the SPET regime is dominant and a dianionic CO_2 adduct $[Co–CO_2]^{2-}$ is formed from $[Co–CO_2]^-$ *(55)*.

Additionally to non-covalent adsorption, other strategies have been developed to covalently attach and study Co-based porphyrins onto carbon-based electrodes *(37,56–61)*, and on reticular materials such as MOFs *(62–65)* and COFs *(18,19,66,67–69)*. These methods enable a more direct translation of solution properties to the surface, and often allow for better control of catalyst loading, film thickness, and the local pH environment *(37)*.

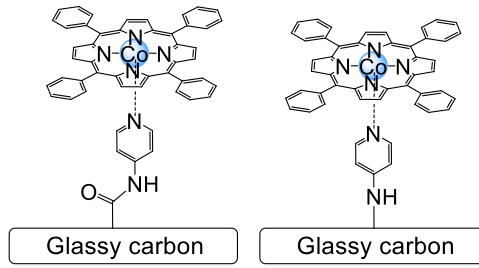

Fig. 11 Selected examples of immobilized **CoTPP** using axial coordination by 4-aminopyridine anchored to the electrode *(57,58)*.

First, for the covalent attachment onto electrodes, in many cases the molecular catalyst reacts or coordinates with specific functional groups or organic molecules introduced on the electrode surface. For instance, in 1991, Aramata and Enyo reported the electrochemical CO_2R of a **CoTPP** fixed on a glassy carbon electrode modified with 4-aminopyridine attached to the electrode by a covalent amide bond (Fig. 11). The **CoTPP**-pyNH-CO/GC electrodes exhibit high electrocatalytic activity and stability for CO_2R to CO in aqueous solutions at potentials 100 mV more positive than those required by water-soluble **CoTPP** derivatives, achieving an overall $TON_{CO} > 10^5$. The increased electron density of the Co(II) center facilitated by the pyridine ligand, enhances the catalyst's performance *(57)*. Later, Aramata reported the functionalization of GC electrodes with 4-aminopyridine by direct anodic oxidation of the amine group, for further coordination to **CoTPP** in the axial position (Fig. 11). Notably, the modified electrode exhibits over 50% efficiency for CO production and demonstrates remarkable stability with an overall $TON_{CO} > 105$. This enhanced performance is attributed to the increased electron density of the Co(II) center facilitated by pyridine coordination, which effectively stabilizes the Co-CO_2 adduct and promotes efficient CO_2 electroreduction. The study underscores the potential of molecular catalyst immobilization via covalent bonding to improve the efficiency and durability of electrocatalytic systems for CO_2R *(58)*. In another example, Hamers and Berry reported the covalent attachment of a Co 5,10,15,20-tetrap-ethynylphenylporphrin (**CoT(alkyne)PP**) onto azide-functionalized boron-doped diamond electrodes through triazolyl linkages (Fig. 12). The system showed electrocatalytic CO_2R to CO for > 1000 cycles at −1.8 V with an estimated TOF of 0.8 s^{-1}. The doubly reduced species was suggested as the active catalyst and CO was the only product detected *(61)*.

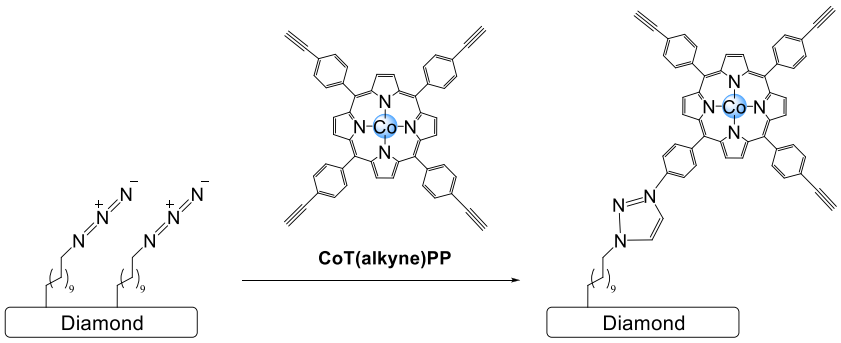

Fig. 12 Anchoring strategy of **CoT(alkyne)PP** on boron-doped diamond electrodes *(61)*.

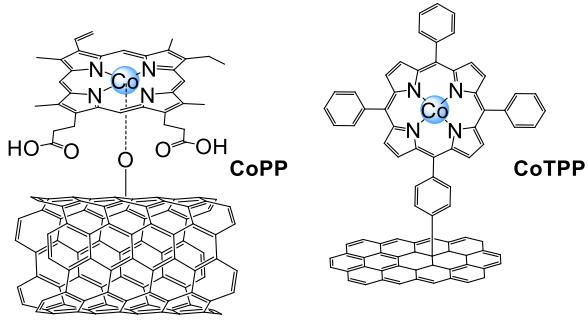

Fig. 13 Anchoring strategy of **CoPP** and **CoTPP** onto MWCNTs *(70)* and carbon cloth *(56)*, respectively.

Additionally, in another example, Ye and Han reported the covalent grafting of **CoPP** onto CNTs for electrocatalyzed CO_2R (Fig. 13). This approach resulted in a highly dispersed catalyst with significantly improved performance compared to traditional physically mixed catalysts. The covalently linked **CoPP**@CNT hybrid exhibited an outstanding current density of 25.1 mA/cm^2 and a FE of 98.3% at an overpotential of 490 mV, with excellent long-term stability. This method enhanced the electron transfer and catalyst-substrate interaction, leading to a higher TOF and selectivity for CO_2 reduction, providing a promising strategy for designing efficient molecular electrocatalysts *(70)*. More recently, Jiang and coworkers reported the covalent attachment of **CoTPP-NH$_2$** to carbon cloth using a phenylene linker, significantly enhancing the electrocatalytic CO_2R to CO thanks to the increase of the electrochemically active surface

density. The covalently immobilized **CoTPP-NH$_2$** exhibited a 81% FE for CO and a TOF of 8.3 s^{-1} at −1.05 V vs NHE, surpassing the non-covalently attached counterpart's TOF of 4.5 s^{-1}, with a cumulative TON of 3.9×10^5 over 24 h, significantly outperforming other CoTPP and Fe porphyrin-based catalysts. The study demonstrates that covalent attachment via a conductive linker markedly enhances the electron transfer rate and overall catalytic efficiency *(56)*.

Following another anchoring strategy, Isaacs and coworkers reported the polymerization of **CoTAP** on an indium tin oxide (ITO) electrode within a ionic liquid medium ($BMImBF_4$) for electrocatalytic CO_2R, resulting in an overpotential reduction from −2.4 V to −0.8 V vs. Ag/AgCl and achieving a FE of 64.9%. This work underscores the potential of using conducting polymers and ionic liquids to enhance the efficiency and selectivity of CO_2 electroreduction *(59)*. In an analogous study, Bocarsly et al. reported the electropolymerization of **CoPP** thin films for the electrochemical CO_2R in aqueous media, achieving CO with a high FE of 84% at an overpotential of 450 mV. The research identifies the rate-determining step as the initial one-electron reduction of the Co center due to sluggish charge transfer kinetics. The study highlights the significance of the local proton source and the importance of pH in optimizing the catalytic performance, with the proposed mechanism involving proton-coupled electron transfer *(71)*.

More recently, Co porphyrins have been explored for photocatalytic CO reduction to develop more sustainable methodologies based on earth abundant elements and the use of water as solvent. In 2019, Cibian, Call, Sakai et al. reported Co porphyrins for CO_2R to CO in aqueous mixtures. In a first study, the authors used a water-soluble **CoTPPS** porphyrin for photocatalytic CO_2R in pure water using **[Ru(bpy)$_3$]$^{2+}$** (bpy = 2,2′-bipyridyl) as photosensitizer and ascorbate as a sacrificial electron donor (Fig. 14A). The photocatalytic system achieved over 82% selectivity for CO production and a TON of 926. At low catalyst loading the system obtained 4000 TON_{CO} and 2400 h^{-1} TOF_{CO}, although with some loss in selectivity *(72)*. In a follow up study the same group reported the photocatalytic CO_2R with **CoTM4PyP** in combination with a water-soluble Cu photosensitizer bearing sulfonate groups (**^{SO3}PS$_{Cu}$**, Fig. 14B) and ascorbate as electron donor. The system achieved high catalytic activity with a TON of 2680 and a TOF of up to 2600 h^{-1} and 77% selectivity for CO. The high efficiency of the system was attributed to the multi-electron

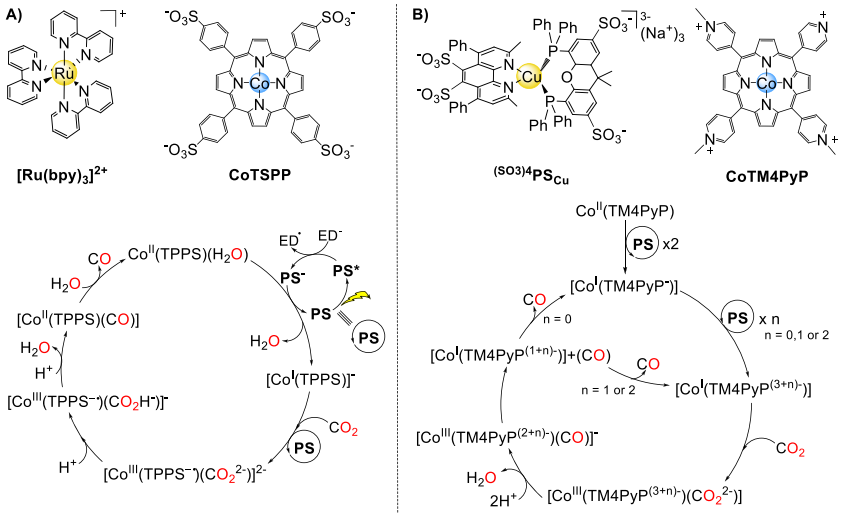

Fig. 14 Reported **CoTPPS/[Ru(bpy)$_3$]$^{2+}$** (A) and **CoTM4PyP/ ^{SO3}PS$_{Cu}$** (B) systems for photocatalytic CO_2R-to-CO and the postulated mechanisms, respectively *(72,73)*.

chargeable property of **CoTM4PyP**, which facilitates rapid electron transfer and enhances CO production *(73)*.

On the other hand, the development of reticular materials incorporating Co porphyrins for CO_2R has led to significant results. In 2015 a remarkable improvement in the catalytic performance was obtained by incorporating a Co tetrakis(4-aminophenyl)porphyrin (**CoTAP**) as a COF building block linked by organic struts through imine bonds reported by the groups of Yaghi and Chang (Fig. 15) for the electrochemical CO_2R to CO in aqueous media. In particular, the authors integrated the **CoTTP** units into COFs and used multivariate synthesis of frameworks containing both catalytic cobalt and structural copper units, resulting in **COF-366-Co**, and the expanded Co/Cu-COFs-367 **COF-367-Co**, **COF-367-Co (10%)** and **COF-367-Co(1%)** (Fig. 15). These COFs exhibited high activity, stability and selectivity for the electrochemical CO_2R to CO in water. In particular, **COF-366-Co** produced CO at −0.67 V applied potential with high selectivity over competing proton reduction with a FE_{CO} of 90% and 24 h stability obtaining 1352 TON_{CO} (34,000 TON_{CO} per electroactive cobalt catalytic site), and 98 h^{-1} TOF (2500 TOF per electroactive cobalt catalytic site). These results show more than 10% enhancement in CO vs H_2 selectivity over the molecular **CoTAP** analogue. Moreover, at the same applied potential, **COF-367-Co** exhibited a

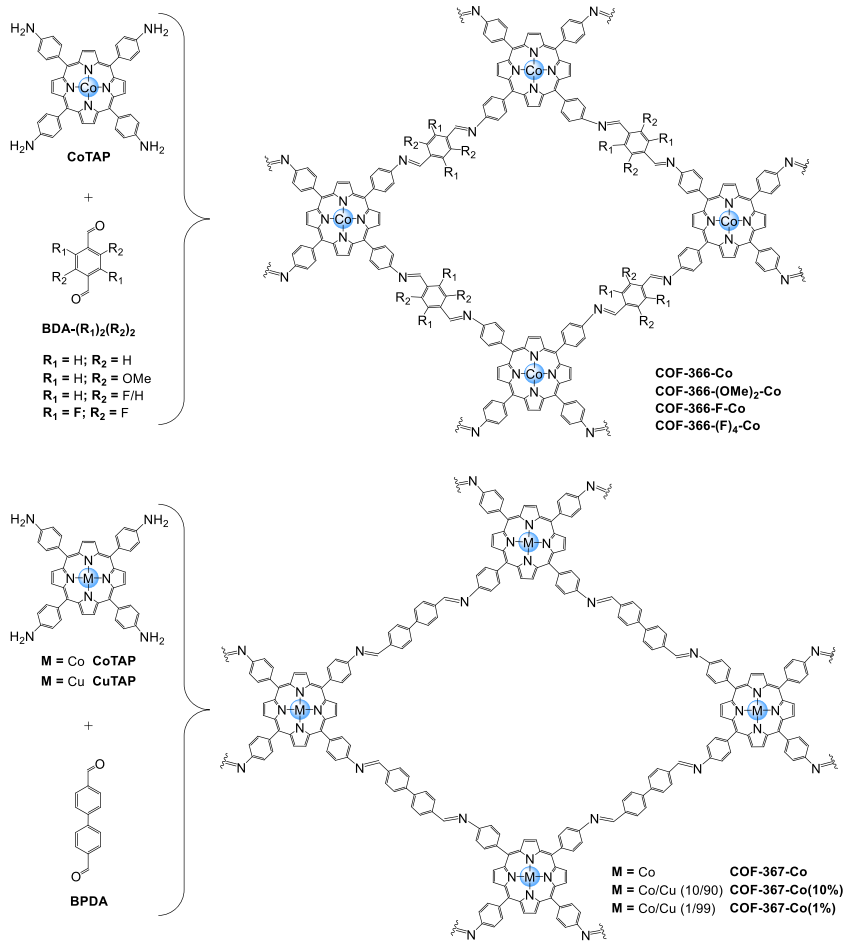

Fig. 15 Representation of the metalloporphyrin-derived COFs based on **CoTAP** and **CuTAP** catalytic centers reported by Yaghi and Chang *(18)*, as well as the subsequent electronic modulation of the **COF-366-Co** *(74)*.

FE_{CO} of 91% during 24 h with 3901 TON_{CO} (48,000 TON_{CO} per electroactive cobalt catalytic site). The best results were obtained with **COF-367-Co(1%)** achieving up to 290,000 TON_{CO} and initial TOF of 9400 h^{-1} per electroactive side at neutral pH with an overpotential of −0.55 volts, resulting in a 26-fold improvement in the catalytic activity compared to molecular cobalt complexes, showing no degradation over 24 h. The study highlights the advantages of modular and tunable COF designs, facilitating enhanced catalytic properties and stability through

spatial and electronic tuning, making them a promising platform for sustainable clean energy applications *(18)*. In subsequent study, the same groups reported the effect of the electronic tunning of the **CoTAP-COF** in the CO_2R activity. The electronic character of the **CoTAP-COF** was tuned by replacing the linkers and improving the catalytic activity (Fig. 7). The activity and selectivity were correlated with the inductive effects of the appended functionality and the electronic character of the reticulated molecular active sites. The extent of this effect was proportional to the electronegativity, and the number of functional groups installed *(74)*.

Later, in 2021 Xu, Zhuang, Liu and coworkers reported the development of a new COF incorporating crown ether B18C6 and **CoTAP** units (**CoTAP-B18C6-COF**) for electrocatalytic CO_2R to CO. The crown ether units in the backbone of **CoTAP-B18C6-COF** played a crucial role by enhancing the hydrophilicity of the frameworks and promoting electron transfer from the crown ether to the Co-porphyrin. The COF enhances the CO_2 binding ability, resulting in 93.2% FE for CO at −0.90 V vs RHE, with a maximum TOF of 1267 h^{-1}. Additionally, the COF exhibits excellent stability and performance, significantly outperforming other COF- and MOF-based catalysts. The study provides new insights into designing effective electrocatalysts by integrating molecular control methods and highlights the potential of crown ether-based COFs in CO_2R applications *(66)*. In another example the Zhang group recently reported metal (Co, Ni, Fe and Cu) TPP porphyrin-based COFs covalently attached to multi-walled carbon nanotubes (MWCNTs) were reported as efficient catalysts for electrochemical CO_2R. The MWCNTs facilitated electron transfer along the porphyrin planes to the immobilized metal active sites. Consequently, covalently linked MWCNT-TPP-COF-M (M: Co, Ni, Fe) showed improved electrocatalytic CO_2-to-CO activity and selectivity compared to pure Por-COF-M and MWCNT@TPP-COF-M without covalent connections between the components. Specifically, MWCNT-TPP-COF-Co exhibited the highest catalytic activity (99.3% FE_{CO}) in 0.5 M $KHCO_3$, higher partial current density and stability in aqueous solutions, while MWCNT-TPPPor-COF-Cu achieved the highest CH_4 FE (71.2%) in 1.0 M KOH in a flow cell. However, HRTEM and Auger spectroscopy results indicated that the high performance of MWCNT-TPP-COF-Cu could be attributed to the formation of Cu-based nanoclusters during electrocatalytic CO_2R *(75)*.

Within the field of reticular materials, in particular, the use of MOFs or 2D MOF nanosheets (or metal−organic layers; MOLs) are interesting

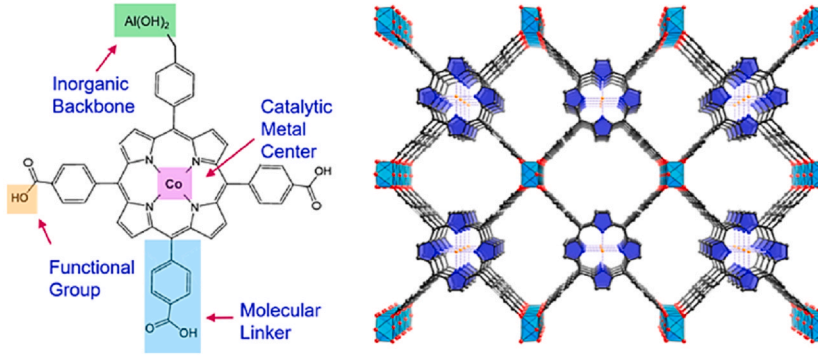

Fig. 16 Representation of the structure and catalytic sites of MOF $Al_2(OH)_2CoTCPP$ reported by Yaghi and Yang and the proposed mechanism *(65)*. *Reprinted with permission from Kornienko, N.; Zhao, Y.; Kley, C. S.; Zhu, C.; Kim, D.; Lin, S.; Chang, C. J.; Yaghi, O. M.; Yang, P. J. Am. Chem. Soc.* ***2015****, 137, 14129, Copyright 2015 American Chemical Society.*

because they facilitate the exposure of the well-defined metal active sites and allow for mechanistic studies *(45,76)*. In this line, the first MOF for electrochemical CO_2R-to-CO in aqueous media was reported by Yaghi, Yand and coworkers in 2015. They developed a **CoTCPP** cobalt-porphyrin-based MOF (**$Al_2(OH)_2$-CoTCPP**, Fig. 16) that exhibited high selectivity for CO selectivity (>76% FE) with a TON_{CO} 1400 per-catalytic-site, and stable performance over 7 h. Mechanistic studies based on in situ spectroelectrochemical analysis revealed a reduction of the Co(II) metal centers to Co(I) throughout the MOF that subsequently reduced CO_2. The MOF structure's modularity allows for precise functionalization, optimizing active-site density and mass/charge transport, demonstrating the potential for further enhancing MOF catalysts' performance by adjusting metal centers, linker units, and film thickness, highlighting MOFs' flexibility and promise in CO_2R *(65)*.

In a different example, Wang and Lin reported the development of MOLs functionalized with **CoPP** and pyridine/pyridinium (py/pyH^+) units (**TPY-MOL-CoPP**, Fig. 17), which significantly improves the electrocatalytic CO_2R to CO, minimizing the H_2 evolution reaction and affording a high CO/H_2 selectivity ratio of 11.8 and a catalytic current density of 1314 mA/mgCo at −0.86 V vs RHE. The study also revealed that the local microenvironment around the **CoPP** centers can be precisely tuned through the MOL structure, enhancing catalytic performance and providing insights into the mechanistic role of pyridinium in CO_2

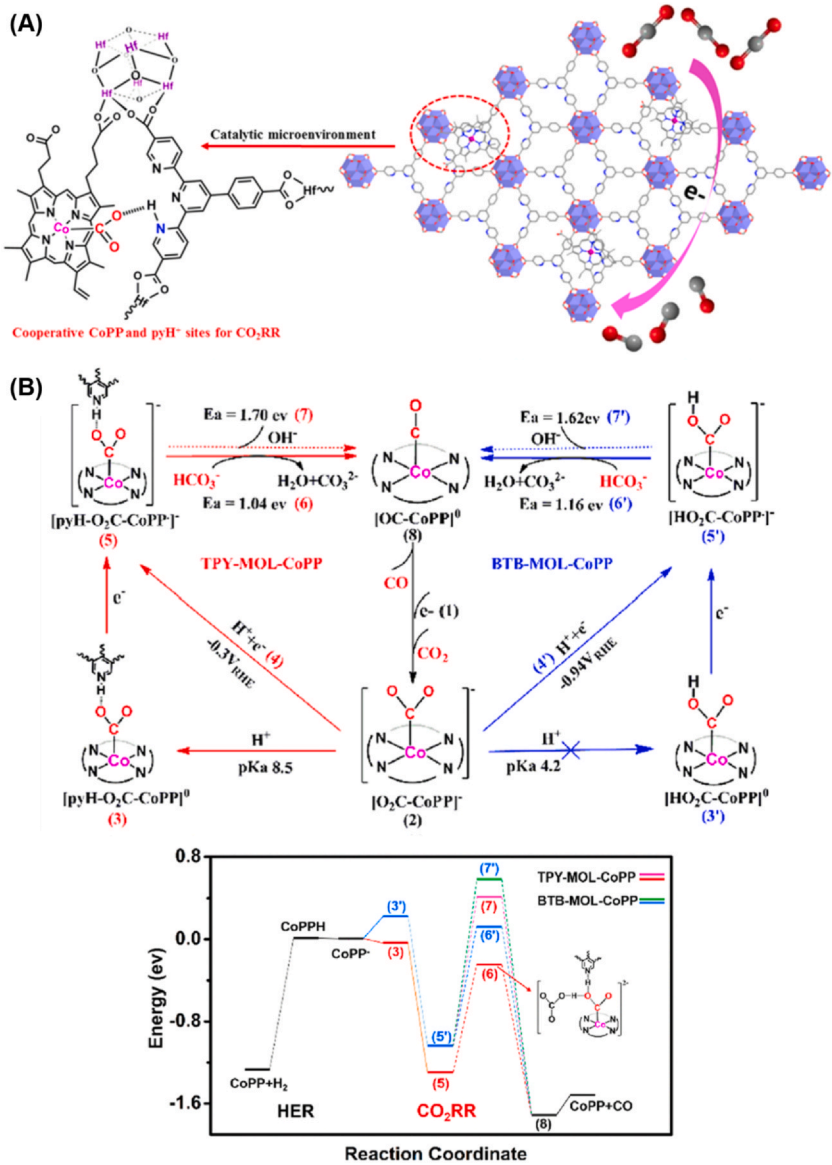

Fig. 17 Structure of **TPY-MOL-CoPP** and the cooperative activation of CO_2 by CoPP and pyH^+ *(77)*. *Reprinted with permission from Guo, Y.; Shi, W.; Yang, H.; He, Q.; Zeng, Z.; Ye, J. Y.; He, X.; Huang, R.; Wang, C.; Lin, W., J. Am. Chem. Soc.* ***2019****, 141, 17875–17883, Copyright 2019 American Chemical Society.*

activation and reduction. The process resembles the second or outer coordination sphere effects by forming a $[pyH^+\text{-}CO_2^-\text{-}CoPP]^0$ species. The addition of divalent cations (Ca^{2+} or Zn^{2+}) decreased the CO selectivity, attributed to the blockage of the terpyridyl units. *In situ* electrochemical diffuse reflectance infrared Fourier transform spectroscopy (DRIFTS) measurements provided evidence of the pyridine protonation to form pyridinium units. In the proposed mechanism, the one-electron reduction of **CoPP** to $[CoPP]^-$ is followed by the CO_2 binding and protonation, leading to the formation of the key $[pyH^+\text{-}CO_2^-\text{-}CoPP]^0$ adduct, which is stabilized by a pre-positioned pyridine moiety to favor CO_2R over H_2 evolution. Then, a second electron reduction follows the C–O bond cleavage, forming $[Co(PP)(CO)]^0$, which undergoes CO release, closing the catalytic cycle *(77)*.

More recently Gu et al. reported ultrathin water-stable 2D-MOFS nanosheets incorporating **CoTCPP** porphyrins anchored onto Zr-BTB. These **CoTCPP/Zr-BTB** nanosheets demonstrate exceptional electrocatalytic performance for CO_2 reduction, achieving a high TOF of 4768 h^{-1} at −0.919 V vs. RHE, with a FE for CO (FECO) of 77.2% and a total current density of 7 mA cm^{-2}. Post-modification with various ligands p-(aminomethyl)benzoic acid (PABA), p-sulfobenzoic acid potassium (PSBA), and p-sulfamidobenzoic acid (PSABA) to tune the microenvironment around the Co center using steric effect, resulted in a improvement of the performance. The resulting **CoTCPP/Zr-BTB-PSABA** exhibiting the highest FE_{CO} (85.1%) and TOF (5315 h^{-1}) *(78)*. The study highlights the significant potential of 2D MOF nanosheets as high-performance electrocatalysts for CO_2R, emphasizing the benefits of precise structural control and post-modification to enhance catalytic activity and stability.

2.2 Phthalocyanine Co complexes

Co phthalocyanines have shown significant potential for application for electrochemical CO_2R. Despite studies indicated that **CoPc** is an ineffective electrocatalyst for CO_2R in a homogeneous phase, its electrocatalytic activity is significantly enhanced when attached to carbon materials and other electrodes, enabling effective use in an aqueous medium *(16,20,79–84)*. In 1974, Meshitsuka and colleagues published the first report on a cobalt phthalocyanine (**CoPc**, Fig. 18) adsorbed on graphite electrodes for the electrochemical CO_2R in aqueous solutions *(85)*. In 1977 Toshima and coworkers examined the electrocatalytic CO_2R with

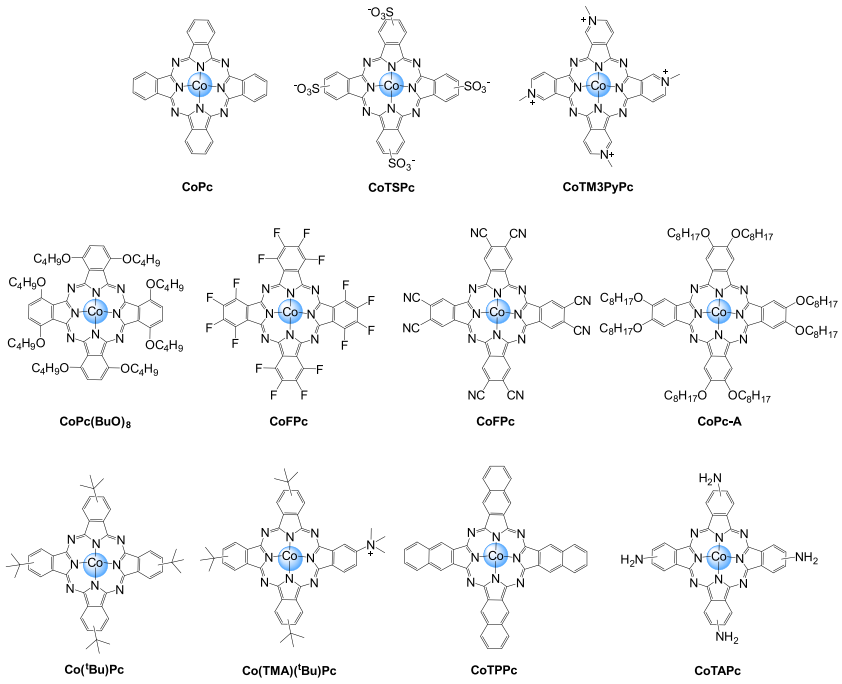

Fig. 18 Summary of the most studied Co phthalocyanines for electro- or photocatalytic CO_2R.

homogeneous water soluble tetrasulfonated metal phthalocyanines (**MTSPc**) in buffer solutions, finding that cobalt (**CoTSPc**) and nickel (**NiTSPc**) derivatives were active and effective catalysts, while copper (**CuTSPc**) and iron (**FeTSPc**) were not. Mechanistic studies pointed to a two-step process: CO_2 adsorption forming a complex with the **MTSPc** at around −0.8 V applied potential, followed by electroreduction at around −1.2 V. Differential capacitance measurements supported this mechanism *(86)*. Later, Lieber and Lewis showed that carbon electrodes modified with **CoPc** can efficiently catalyze the reduction of aqueous CO_2 to CO near the thermodynamic redox potential, with high selectivity and minimal byproducts. The modified electrodes exhibited significantly enhanced stability and catalytic efficiency compared to homogeneous CoPc solutions, achieving 90–95% FE and TOF > 100 s^{-1}. The authors performed preliminary mechanistic studies suggesting an initial protonation step followed by reduction and CO_2 attack *(87)*. In an analogous study, Harty and coworkers reported PTFE-bonded carbon electrodes impregnated with

CoPc for electrocatalytic CO_2R to CO with high efficiency, while electrodes with Mn, Cu or Zn phthalocyanine primarily produced formic acid and hydrogen. The distinct electrochemical behaviors of the metal ions account for the variation in products, with cobalt(II) facilitating CO formation via reduction to Co(I) *(88)*. A similar trend of CO production by **CoPc**-electrodes was reported in 1989 by Matsui et al. They investigated porous carbon gas-diffusion electrodes modified with 17 different metal phthalocyanines for electrocatalytic CO_2R. They found that the product distribution and current efficiencies were highly dependent on the central metal. Group VIII metals like Co and Ni produced mainly CO with a current efficiency of nearly 100%. Sn, Pb, and In phthalocyanines yielded formic acid, with Sn achieving about 70% efficiency at −1.6 V. Cu, Ga, and Ti phthalocyanines primarily generated methane with 30–40% efficiency *(89)*. Another study was reported by Lever and coworkers, where they developed a N,N′,N″,N″-tetramethyltetra-3,4-pyridoporphyrazinocobalt(ll) (**CoTM3PyPc**, Fig. 18) immobilized onto a graphite disk and protected by a Nafion® film for electrochemical CO_2R to CO *(90)*. Later, in 1996, Kaneko et al. reported the coating of a graphite electrode with cobalt octabutoxyphthalocyanine (**CoPc(BuO)$_8$**, Fig. 18) for electrochemical CO_2R. The addition of alkoxide chains on the Co phthalocyanine resulted on higher activity and selectivity for CO production compared to non-substituted **CoPc**, which was attributed to the electron-donating BuO substituents that facilitated CO_2 coordination and electron transfer. Mechanistic studies based on in situ potential-step chronoamperospectroscopy (PSCAS) confirmed the formation of a one-electron reduced species of **CoPc(BuO)$_8$** under steady step. Moreover, the authors proposed that a third reduction of the CO_2-coordinated **CoPc(BuO)$_8$** intermediate was crucial for CO production *(91)*.

Following another electrode-immobilization approach, in 1996, Kaneko et al. incorporated **CoPc** into a coordination polymer poly-4-vinylpyridine (P4VP) membrane coated on a graphite electrode for electrocatalytic CO_2R in aqueous electrolytes. The pyridyl groups of P4VP served as anchoring points for **CoPc** through axial coordination to the cobalt center. This system achieved enhanced electrocatalytic activity at more positive potentials and with greater efficiency compared to pure **CoPc**. The improved and sustained catalytic activity of the **CoPc**/P4VP membrane was attributed to electron donation from the pyridine group to the cobalt center, the proton-exchanging properties of P4VP, and increased local CO_2 concentration in the P4VP layer due to hydrophobic

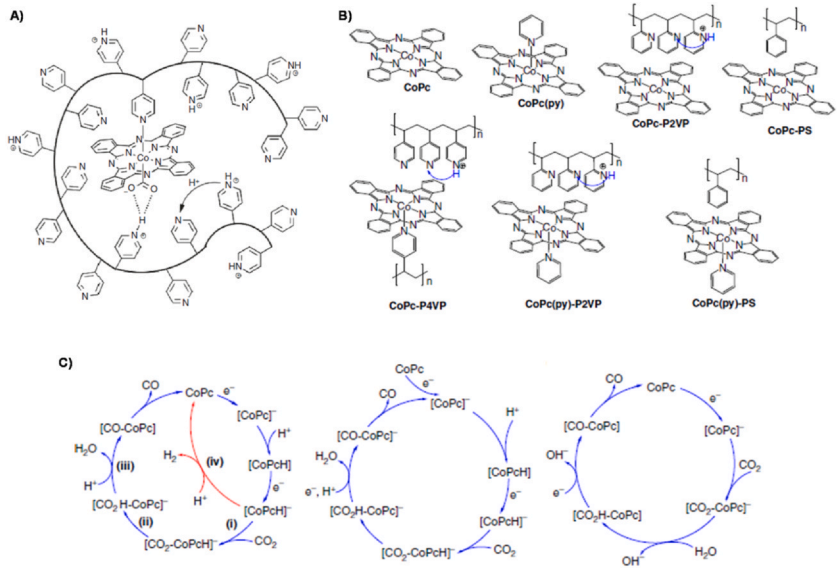

Fig. 19 (A) Representation of the **CoPc** encapsulated within P4VP, first developed by the group of Kaneko in 1996 *(92)* and further studied by the group of McCrory *(94,95)*. (B) Representation of the different **CoPc-P4VP** derivative systems investigated by the group of McCrory, and (C) their proposed CO_2R mechanism (left) compared to other proposed mechanism by **CoPc** in organic solvent (middle) and low concentration bicarbonate buffer in aqueous solution (right) *(94,95)* derivatives. *Figure reprinted with permission from Liu, Y.; McCrory, C. C. L. Nat. Commun.* ***2019****, 10, 1683, Copyright 2019 Springer Nature.*

and acid-base interactions *(92)*. Moreover, in acidic (pH ~ 5) conditions the CO_2R selectivity for CO was enhanced with a CO/H_2 selectivity ratio of about 6 at −1.20 V vs. Ag/AgCl, compared to neat **CoPc**. The enhanced catalytic activity and selectivity was ascribed to the PVP's basic and coordinative properties that create a favorable environment around **CoPc**, where the PVP provides a partially protonated environment around the metal center. The study proposed a concerted protonation-deprotonation mechanism, with electron donation from the pyridine group to the Co center enhancing catalytic activity, and suggested that a CoPc-CO_2 intermediate accepts a third electron to produce CO *(93)*. Following a similar anchoring strategy, in 2026 and 2019 the group of McCrory further investigated the effect of P4VP-polymer films coordination on **CoPc** on the selectivity and the catalytic activity for electrochemial CO_2R *(94,95)*. It was found that the P4VP membrane not only increased the rate of

CO_2R but also suppressed the competing H_2 evolution reaction due to the synergistic effects of axial coordination of pyridine residues to **CoPc** and the secondary and outer coordination sphere effects provided by the **P4VP** matrix (Fig. 19A and B). The study showed that **CoPc-P4VP** exhibited a FE of nearly 90% for CO production, with a TOF of 4.8 s^{-1} at −0.75 V vs. RHE, positioning it among the most active molecular catalysts for CO_2R in aqueous solutions *(94)*. In a follow up study, the same group studied the effect of the modification of the coordinated polymer in the electrocatalytic CO_2R mechanism using **CoPc** embedded in P4VP and derivative. Upon mechanistic studies the authors provided evidence that the axial coordination of the pyridine residues in P4VP to the **CoPc** complex modifies the rate-determining step of the reaction, resulting in increased activity. Moreover, the polymer acts as a proton relay mechanism that suppresses competitive H_2 evolution (Fig. 19C). These mechanistic insights offer strategies for designing more effective CO_2R electrocatalysts by modulating the coordination environment and proton transfer dynamics within polymer-encapsulated systems *(95)*.

To get further insight on the effect of the electrode catalyst loading in the electrocatalytic activity, Manthiram et al. studied the effect of catalyst loading (ranging from 5×10^{-12} to 1×10^{-7} mol·cm^{-2}) and dispersion on the CO_2R activity of **CoPc** drop-casted on oxygen-functionalized carbon paper. The authors found that lower catalyst loadings and higher dispersion levels help reduce transport limitations and avoid aggregation, significantly enhancing the TOF *(96)*. In another example, Wang, Liang and coworkers used hybridization of **CoPc** on CNTs to minimize catalyst aggregation. This was translated into higher electrochemical CO_2R-to-CO activity and better stability compared to their molecular counterparts due to the prevention of molecular aggregation and enhanced charge transport *(97)*.

These studies show that the immobilization of **CoPc** on electrodes not only prevented catalyst decomposition but also ensured sustained catalytic activity, making this approach a promising avenue for efficient electrochemical CO_2R. Therefore, immobilization of cobalt phthalocyanines complexes onto electrodes for electrocatalytic CO_2R has been a promising strategy to make more efficient electrocatalytic CO_2R catalysts *(12–14,20,24,87–90,93,98–101)*.

Another important factor in the modulation of the CO_2R catalytic activity is the modification of the steric and electronic effects of the at the metal center by ligand modification. For instance, Wallace, Officer and coworkers showed that the steric modification of **CoPc** immobilized on

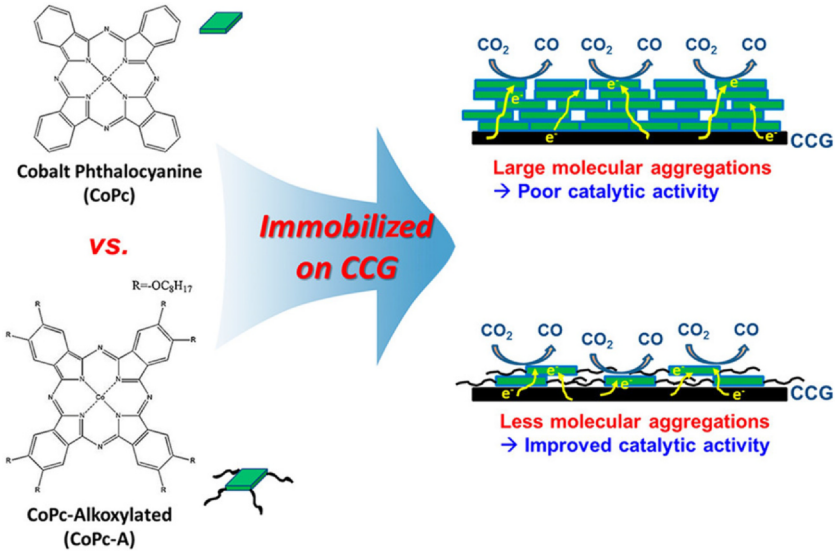

Fig. 20 Representation of the proposed CO_2R mechanism on the **CCG/CoPc** and **CCG/CoPc-A** hybrids. *Reprinted with permission from Choi, J.; Wagner, P.; Gambhir, S.; Jalili, R.; MacFarlane, D. R.; Wallace, G. G.; Officer, D. L. ACS Energy Lett.* ***2019****, 4, 666–672, Copyright 2019 American Chemical Society.*

chemically converted graphene (CCG) via π-π stacking to a sterically hindered cobalt(II) octaalkoxyphthalocyanine (**CoPc-A**), enhanced the electrocatalytic CO_2R activity (Fig. 20). This modification suppressed phthalocyanine aggregation on graphene, enhancing catalytic activity and stability for CO_2R to CO. The **CoPc-A/CCG** catalyst demonstrated a significantly higher catalytic activity (TOF 5 s^{-1} at 480 mV overpotential) and maintained stable CO conversion over 30 h of electrolysis compared to the unsubstituted **CoPc/CCG** catalyst. This enhanced performance is attributed to better dispersion, reduced aggregation, and increased CO_2 accessibility facilitated by the alkoxy groups, resulting in improved electron transport and mass transport properties within the catalyst structure *(102)*. Enhanced catalytic activity and stability by the prevention of CoPc aggregation was also reported by Li and coworkers by the immobilization of **CoPc** thin films on MWCNTs synthesized by microwave-assisted template-directed method. The **CoPc/MWCNT** exhibited 90% FE for CO, a TOF of 4900 h^{-1} at an overpotential of 0.5 V, and stable long-term operation for over 24 h in 0.5 M $NaHCO_3$. Density functional theory (DFT) calculations revealed that the Co center was first reduced from

Co(II) to Co(I), facilitating the formation of a CO_2 anion through charge transfer. This anion then formed a COOH* intermediate via proton transfer, which subsequently converted to CO* through a concerted proton-electron transfer (CPET) step *(103)*. Analogously, other electrode-immobilization methods have been reported *(12,13,20,29,24)*, such as single-pot hydrothermal synthesis *(104)*, solid-state polycondensation *(105)* and direct electropolymerization *(106,107)*.

Regarding the modification of the electronic effects around the metal center in Co phthalocyanines, it was observed that the introduction electron-withdrawing groups, like perfluorinated **CoPc** (**CoFPc**) and cyano-modified **CoP**c (**CoCNPc**) (Fig. 18), further enhanced the electrochemical CO_2R activity and selectivity, achieving high FE and efficient CO_2R-to-CO at lower potentials *(108,109)*. Rodionov et al. showed that **CoFPc** adsorbed on carbon cloth exhibited robust performance for concurrent CO production and water oxidation, achieving high CO selectivity (FE 93%) at −0.8 V vs. RHE at the cathode under neutral pH conditions. The fluorine substituents not only positively shift the CoII/I redox potential but also facilitate CO release, accelerating catalytic turnover. reduced CO2-to-CO *(108)* reported **CoCNPc** functionalized MWCNTs (**CoCNPc/MWCNTs**) resulted in higher selectivity for CO2-to-CO (FE 98%) at lower overpotential and high current densities (∼15 mA cm^{-2}) at −0.63 V vs. RHE *(109)*. Other ligand modifications have been reported. For instance, Berlinguette, Robert and coworkers developed an electrode-immobilized **CoPc** derivative with one trimethyl ammonium (positively charged) and three tert-butyl groups appended to the periphery of the Pc macrocycle (**Co(TMA)(tBu)$_3$Pc**, Fig. 18). **Co(TMA)(tBu)$_3$Pc** showed highly active and selectivity (91% FE) for electrocatalytic CO_2R to CO in a wide pH range from 4 to 14 with over 10 h stability. Its enhanced reactivity was attributed to the through-space interactions between the negative charge of the O atoms in CO_2 and the positive charge of the trimethyl ammonium substituent of **Co(TMA)(tBu)$_3$Pc**. These interactions facilitated not only the reductive coordination of CO_2 to the central Co atom but also the cleavage of the C–O bond of CO_2 followed by CO formation *(16)*.

On the other hand, there are limited studies on using metal phthalocyanines for photocatalytic CO_2R. In one example, Reisner et al. developed a polymeric cobalt phthalocyanine (**CoPPc**) with mesoporous carbon nitride (mpg-CNx) for photocatalytic CO_2 reduction to CO in organic solvents. This hybrid catalyst, converted CO_2 to CO under UV/Vis solar-simulated light, achieving a TON of 90 after 60 h irradiation. It retains 60%

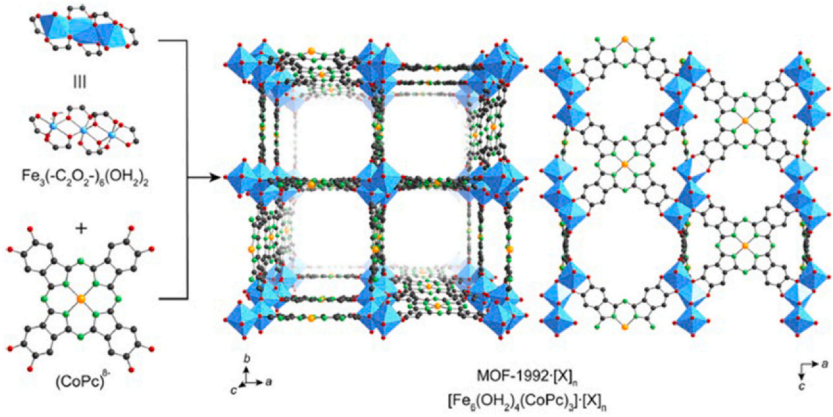

Fig. 21 Single crystal X-ray structure of MOF-1992 based on Fe trimers and Co phthalocyanine catechol linkers (**CoPc**) reported by Yaghi et al. Atom color scheme: C, black; O, red; N, green; Co, orange; Fe, blue polyhedra. Hydrogen atoms and chlorido ligands (section S3) are omitted. The anionic charge of $[Fe_6(OH_2)_4(CoPc)_3]^{6-}$, MOF-1992, is balanced by the presence of $[X]^n$ counterions ($X = Mg^{2+}$ or Fe^{3+}). *Reprinted with permission from Matheu, R.; Gutierrez-Puebla, E.; Monge, M. Á.; Diercks, C. S.; Kang, J.; Prévot, M. S.; Pei, X.; Hanikel, N.; Zhang, B.; Yang, P.; Yaghi, O. M. J. Am. Chem. Soc.* ***2019****, 141, 17081–17085, Copyright 2019 American Chemical Society.*

activity under visible light and shows moderate water tolerance. The authors proposed that the in situ polymerization of the phthalocyanine was crucial for controlling catalyst loading, as well as enhancing the photocatalytic efficiency *(107)*.

Analogously to Co porphyrins, the incorporation of Co phthalocyanine derivatives into reticular materials has further improved their activity and efficiency for CO_2R. Yaghi and coworkers reported the use of Co phthalocyanine catechol building blocks to create a novel metal–catecholate framework (MOF-1992) for electrochemical CO_2R. Confinement of the **CoPc** onto the MOF framework (Fig. 21) resulted in more accessible **CoPc** catalytic sites and an enhanced electronic communication between the catalyst and the conductive surface, leading to a significantly higher electroactive surface area than that of the previously reported reticular Co/Fe catalysts. This resulted in a 3-fold improvement of the TOF for CO production, achieving a FE of up to 97% *(110)*. In an analogous study, Tang and coworkers reported the decoration of the external surface of the zeolite ZIF-90 with active Co tetraminonaphthalocyanine (**CoTAPc**) units also produced a selective CO_2-to-CO electrocatalyst. This system

showed a large current density of 13 $mA \cdot cm^{-2}$ for CO production in aqueous media at an overpotential of 0.86 V with a FE of 90%, with significantly higher catalyst stability compared with the free phthalocyanine molecule *(111)*.

In addition to CuPc-based catalysts, CoPc-based catalysts have recently been explored towards further CO_2R beyond $2e^-$ *(14,20,112,113)*. For instance, Liang, Wang and coworkers reported a significant advancement in the electrochemical reduction of CO_2, demonstrating that **CoPc** immobilized on CNTs could catalyze the six-electron reduction of CO_2 to MeOH with high selectivity and activity. The authors proposed a domino mechanism where CO_2 is first reduced to CO, which is subsequently reduced to MeOH, with a FE over 40% and a partial current density over 10 $mA \cdot cm^{-2}$ at −0.94 V vs. RHE in a near-neutral electrolyte. However, the catalytic activity declined over time due to the reduction of the phthalocyanine ligand, a challenge that was mitigated by the modification of the ligand with electron-donating substituents, resulting in improved stability and performance for at least 12 h *(113)*. In a parallel study, Robert et al. systematically investigated the catalytic reduction of CO_2 to methanol by **CoPc** on MWCNTs in aqueous electrolytes. They reported a subsequent two-step process for the electrochemical CO_2R-to-CO and subsequent further CO reduction to methanol, achieving 95% FE for CO in the first reduction, and further reducing it to methanol at pH 13 with an overall FE of 19.5%. Mechanistic studies pointed to the formation of a key formaldehyde intermediate, with the Cannizzaro reaction possibly contributing to methanol production *(14,20,114)*. Moreover, it is worth noticing that the real potential of cobalt phthalocyanine was achieved when operating under flow conditions using an aqueous electrolyte *(16,115,116)*. For instance, the groups of Robert and Berlinguette reported the evaluation of **CoPc** in a tandem flow cell with nickel foam in the anode led to excellent CO selectivity at industrially relevant current densities (200 $mA \cdot cm^{-2}$) at an overall cell voltage of ca. 2.5 V, while maintaining high product selectivity, out-performing Ag nanoparticles as a CO_2R-to-CO reduction catalyst *(117,118)*.

2.3 Corrole and corrin Co complexes

In 2002 Neta, Fujita, Gross and coworkers reported a Co corrole with a 5,10,15-tris(pentafluorophenyl)corrole ligand (**Co^{Ph3P}TPFC**) for photocatalytic CO_2R to CO in acetonitrile, using p-terphenyl (TP) as photosensitizer and triethylamine (TEA) as sacrificial electron donor (Fig. 22).

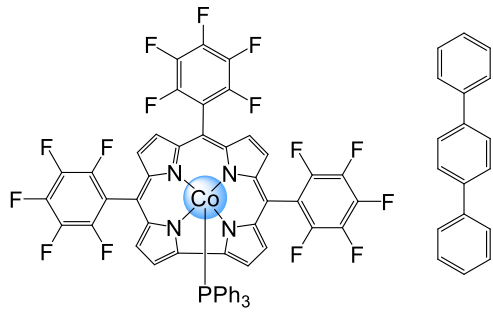

Co^{Ph3P}TPFC **TP**

Fig. 22 Representation of the Co corrole **Co^{Ph3P}TPFC** and the **TP** photosensitizer reported by Neta, Fujita, Gross and coworkers *(119)*.

The authors demonstrated that a catalytically active Co(I) intermediate is formed and then it reacts with CO_2 to produce CO obtaining TON_{CO} ~300, unlike their porphyrin and phthalocyanine counterparts where a more reduced species is required. The system also works under electrochemical conditions to reduce CO_2 to CO. In all cases H_2 was also formed under catalytic conditions. These findings underscore the potential of corroles as effective catalysts for CO_2R in both electrochemical and photochemical processes *(119)*.

More recently, Schöfberger, Roy and coworkers reported the immobilization of a **Co^{Ph3P}TPFC** corrole-derivative functionalized with polyethylene glycol (PEG) onto carbon paper electrodes for electrocatalytic CO_2R. The heterogenized system produced ethanol and methanol with a FE of 47% and 59%, respectively, at −0.73 V vs. RHE applied potential. Comprehensive investigations including isotopic ^{2}D- and ^{13}C-labeling monitored by GC-MS confirmed water as the proton source and CO_2 as the source of carbon for the obtained CO_2R-derived products. This together with further spectroscopic NMR and EPR studies, IR-spectroelectrochemistry (IR-SEC), and complementary control experiments resulted in the proposed mechanism involving a Co^{III}–$CO_2^{\cdot -}$ intermediate that was characterized by EPR, formed after the reduction of CO_2 by the catalytically active Co(I) species. Then, Co^{III}–$CO_2^{\cdot -}$ would undergo subsequent PCETs to form a HCO_2H intermediate, which was analyzed by NMR. Subsequent one-electron reduction and OH^- dissociation leads to a Co^{III}-stabilized $HCO^{\cdot}$ intermediate that leads to a mechanistic bifurcation. While one further PCET allows formaldehyde generation, a

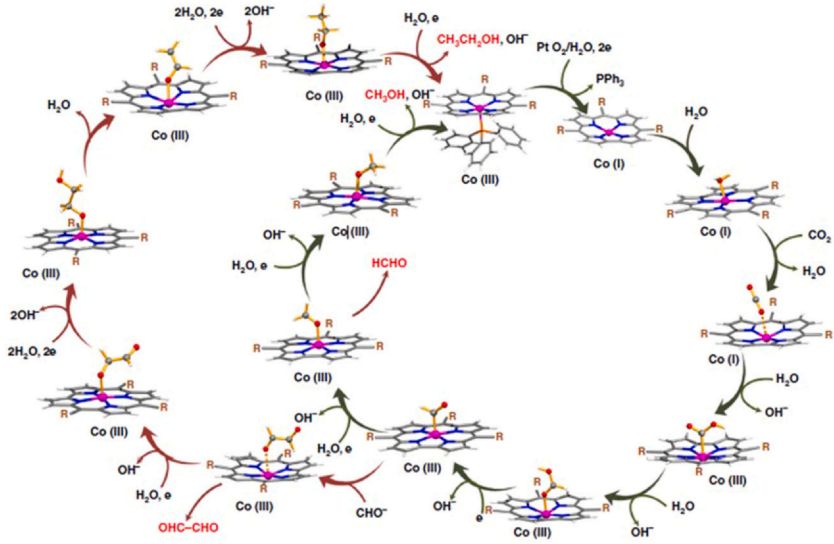

Fig. 23 Single-site mechanism of CO_2R a **Co^{Ph3P}TPFC** corrole-derivative proposed by Gonglach et al. *(120)*. *Reprinted with permission from Gonglach, S.; Paul, S.; Haas, M.; Pillwein, F.; Sreejith, S. S.; Barman, S.; De, R.; Müllegger, S.; Gerschel, P.; Apfel, U. -P.; Coskun, H.; Aljabour, A.; Stadler, P.; Schöfberger, W.; Roy, S. Nat. Commun.* ***2019****, 10, 3864. Copyright 2019 Springer Nature.*

second one gives methanol as the main product. In the other direction, dimerization yields oxaldehyde as a key intermediate that undergoes several PCETs to give ethanol as the second most generated product. External addition of OHC-CHO under the initial reaction conditions resulted in an increased formation of EtOH and confirmation of its role as a key intermediate (Fig. 23) *(120)*.

Since hydrogenation of porphyrin rings during photochemical experiments is a degradation pathway *(37)*, Co corrins (B_{12}) with fewer double bonds **cyanobalamine**, **hydroxocobalamine** and **cobinamide** (Fig. 24) were examined for photocatalytic CO_2R in combination with TP as a sensitizer and TEA as sacrificial electron donor. Similar to Co porphyrins, reduction to form the catalytically active Co(0) species was needed to react with CO_2, producing CO, formate, and H_2 at higher rates (7–13 times greater) than **CoTPP** under the same photocatalytic conditions and with higher selectivity, producing more quantity of reduced products. A selectivity of 31% CO was obtained for **CoTPP**, whereas higher selectivity was obtained by the corrin complexes, 40% with **hydroxocobalamin**, 45% with **cyanocobalamin** and 53% with **cobinamide** *(121)*.

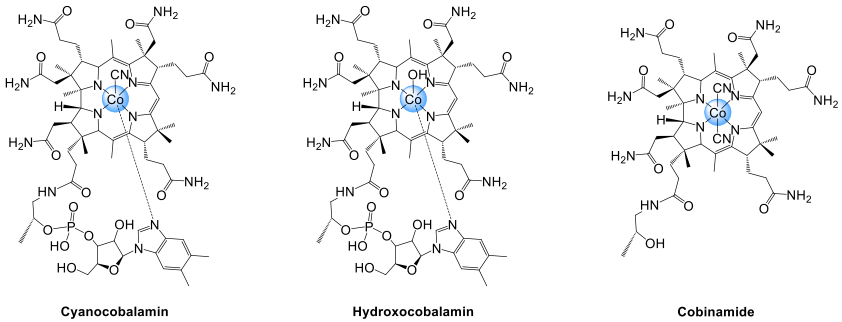

Fig. 24 Representation of the Co corrins **cyanobalamin**, **hydroxocobalamin** and **cobinamide** for photocatalytic CO_2R.

3. Non-heme macrocyclic, polypyridyl and aminopyridyl complexes

In this section, we discuss three distinct families of cobalt catalysts: non-heme macrocyclic, polypyridyl, and aminopyridyl complexes. These catalysts share a common structural feature where the metal center is coordinated by nitrogen-donor ligands, such as amines or pyridines, which results in similar reactivity patterns.

3.1 Imino-aminopyridine complexes and related systems

In 1980, Ficher and Eisenberg reported one of the earliest examples of CO_2 electroreduction catalysts based on metal complexes, the macrocyclic complexes $[Co(HMD)]^{2+}$ (**Co1**, Fig. 25) *(122)*. They showed that **Co1** mediated the electrochemical reduction of CO_2 at −1.6 V vs SCE, producing as mayor products CO and H_2. The Cobalt 'cyclam-like' complex has a macrocyclic tetraazacyclotetradeca-7,14-diene that confers certain stability, including low oxidation states due to the presence of imines. Nevertheless, **Co1** demonstrates lower selectivity for CO production compared to the nickel derivative with the same ligand. However, presented an interesting feature the CO_2 binding constant to the one electron reduce $[Co^{I}]^{+}$ intermediate ($KCO_2 \approx 10^4\ M^{-1}$) is significantly higher than that observed with Ni-cyclam, by approximately four orders of magnitude *(123)*. Similar to the cyclam ligand, the presence of polar –NH groups is essential for stabilizing the η^1-CO_2 ligand *(124)*. Later, Fujita and coworkers have made significant contributions to the study of CO_2 reduction using **Co1** as a model catalyst. **Co1** served as a platform to characterize

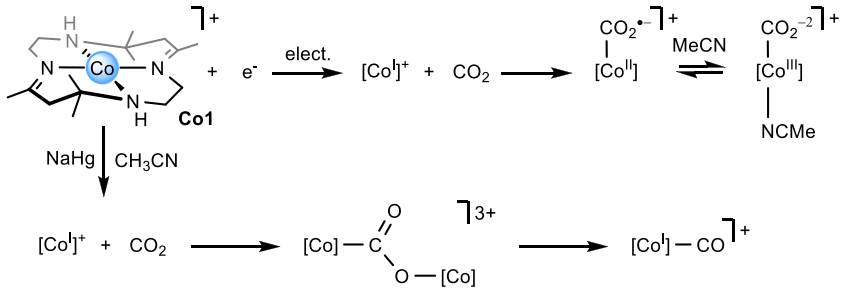

Fig. 25 Steps and intermediates involved in the CO_2 catalytic reduction process.

reaction intermediates. They isolated and characterized the $[Co\text{-}CO_2]^+$ adduct UV-Vis, FT-IR, ^1H NMR, laser flash photolysis, and pulse radiolysis *(125–131)*. XANES (X-ray absorption near edge structure) spectroscopic studies determined that the electronic structure of the carboxylate adduct was a cobalt(II) with a CO_2 radical anion coordinated, $[Co^{II}(CO_2^{\bullet -})]^+$ for the pentadentate complex and a cobalt(III)-CO_2^{-2} for the hexacoordinated ($[(MeCN)Co^{III}(CO_2^{-2})]^+$) *(132)*. This coordination environment was similar to an earlier example *(133)* reported by reducing a cobalt Salen complex (**Co2**, Fig. 26) with K and further reaction with CO_2 ($[Co(pr\text{-}salen)K(CO_2)THF]_n$), where the CO_2 is bonded to the cobalt atom by the Carbon and oxygen atoms to the K^+ ions *(134)*. Additionally, an interesting bimetallic $[Co\text{-}C(OH)O\text{-}Co]^{3+}$ adduct was characterized in the solid state by X-ray diffraction after sparging with CO_2 a solution containing $[Co^I]^+$ formed by reduction with NaHg *(135)*. After several days, the reaction mixture produced the cobalt(I) carbonyl, $[Co^I\text{-}CO]^+$, another important intermediate *(133,136)*.

Recent research with **Co1** highlights demonstrated that bimetallic intermediates are formed in situ from two singly reduced **Co1** species bridged by a CO_2 molecule *(137)*. The presence of coordinating species, such as formate anions, assists in the formation of these intermediates. This bimetallic pathway provides access to elementary steps with lower energy requirements, making the overall catalysis kinetically more facile compared to the mononuclear pathway. Techniques such as pulse radiolysis time-resolved infrared (PR-TRIR) spectroscopy, density functional theory (DFT) calculations, and infrared spectroelectrochemistry (IR-SEC) were used to characterize all major steps of the proposed catalytic cycle.

Numerous molecular catalysts with non-heme ligand platforms have been developed for CO_2 to CO reduction (Figs. 25–26). An interesting

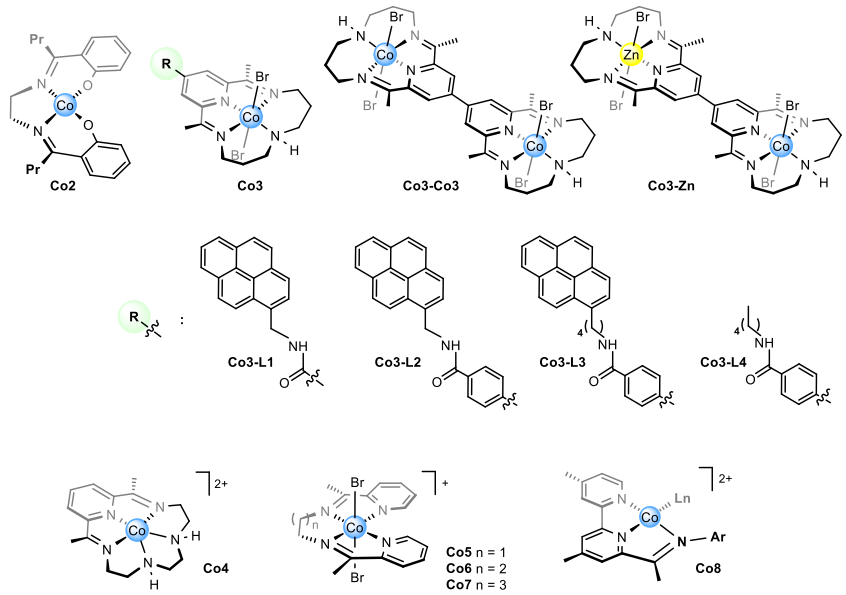

Fig. 26 Selection of imino and aminopyridine complexes. S stands for solvent.

platform is the redox-active pyridyldiimine moiety *(138)* which requires additional coordination, such as in its macrocyclic ligand version (**Co3**) to show improved stability and catalytic performance *(139–141)*. Peters and co-workers further studied the bis(imino)pyridine **Co3** complex as an electrocatalyst, archiving a Faradaic efficiency of 45% and 30% for CO and H_2, respectively, in aqueous acetonitrile *(142)*. In this system, a doubly reduced intermediate facilitates the CO_2 binding, consistent with ligand's non-innocent nature. Further studies revealed that the bound –NH group significantly stabilizes the Co-CO_2 adduct through hydrogen bonding interactions *(143)*. In a follow up study was explored the activation and CO_2 reduction two different visible light sensitizers, $[Ru(bpy)_3]^{2+}$ and $[Ir(ppy)_3]$. The research employs in situ FT-IR measurements and density functional theory (DFT) calculations to understand the mechanistic pathways and electronic structures involved. The results indicate that the cobalt complex undergoes reduction to form a carboxylate intermediate, with further reduction leading to CO production when using a stronger reductant like $[Ir(ppy)_3]$.

These works highlight the importance of the redox non-innocence of the macrocyclic ligand in facilitating CO_2 activation and provides insights into the role of the ligand in stabilizing the intermediate states, ultimately

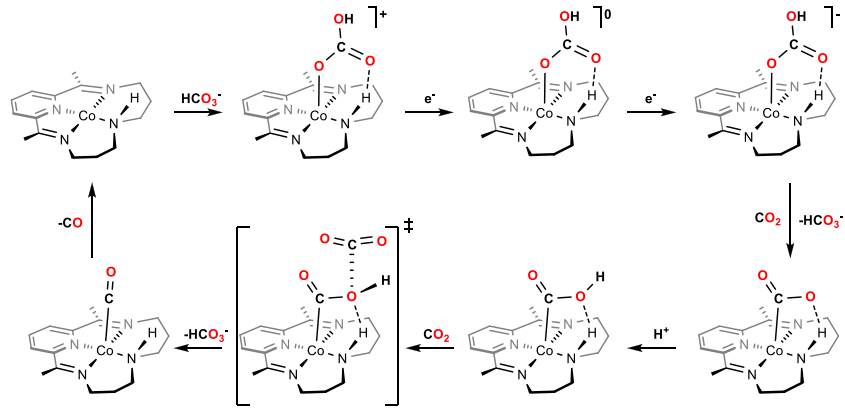

Fig. 27 Proposed mechanism for the electrochemical reduction of CO_2 by a bis(imino) pyridine cobalt complex **Co3** *(146)*.

contributing to the efficient reduction of CO_2 to CO *(144)*. Sheng and Frei *(145)* also investigated the mechanistic pathways of CO_2 reduction facilitated by **Co3** using rapid-scan FT-IR spectroscopy and visible-light sensitization. The study captures and identifies key intermediates, beginning with a one-electron reduced CO_2 adduct $[Co^{I}\text{-}CO_2{}^{d-}]^{+}$, which upon receiving a second electron, transforms into a two-electron reduced $[Co^{I}\text{-}CO_2{}^{-}]^{0}$ complex (Fig. 27). This intermediate subsequently undergoes a rate-limiting step to produce CO while regenerating the catalyst *(145)*. Although it is clear that the ligand presented a redox non-innocent nature, the electronic structure of the reduced states it was been seen DFT dependent.

Garza et al. *(146)* examined the CO_2R mechanism of **Co3**, through DFT calculations elucidated the selectively towards CO vs H_2. The research demonstrates that the doubly reduced **Co3** complex preferentially binds CO_2 (−13.3 kcal/mol) over bicarbonate (−1.9 kcal/mol) or water (−6.4 kcal/mo), facilitating the formation of CO through a sequence of protonation and CO_2 interactions. This binding energy difference underscores the catalyst's preferential affinity for CO_2, driven by electronic and structural factors, including partial charge transfer from the catalyst to CO_2 and hydrogen bonding interactions between the CO_2 oxygen and the NH group in the tetraaza ring. The providing a detailed mechanistic pathway aligns with experimental observations *(146)*.

The pyridyldiimine moiety is versatile and covalent bridge ligands can be obtained and the corresponding homobimetallic cobalt (**Co3-Co3**) and heterobimetallic cobalt-zinc (**Co3-Zn**) complexes can be synthesized. In

the study, the electrocatalytic reduction of CO_2 using the bimetallic complexes demonstrate enhanced catalytic performance compared to their monometallic counterparts. These bimetallic complexes exhibit enhanced catalytic performance compared to their monometallic counterparts. Specifically, the **[Co3-Zn]** complex demonstrates 2 orders of magnitude larger TOF than the parent monometallic **Co3** and 2 orders of magnitude larger TOF_{cat} and 6 orders of magnitude larger TOF_0. This complex also shows a more positive onset potential for CO_2 reduction. The improvement in catalytic performance is attributed to the electrostatic effects exerted by the Zn^{2+} cation, which enhances the stability of the CO_2 adduct and facilitates electron transfer. The study highlights that the incorporation of a redox-inactive Zn^{2+} site into the bimetallic complex significantly improves the overall catalytic activity and selectivity for CO_2 reduction to CO. The role of intramolecular interactions and electrostatic effects in modulating the redox properties and catalytic activity of these bimetallic systems is emphasized, providing a quantitative framework for understanding the enhancement in catalytic performance. The incorporation of redox-inactive metal sites, such as Zn^{2+} in the **[Co3-Zn]**, offers a promising strategy to enhance catalytic activity through electrostatic stabilization of intermediates *(147)*.

In a related study, Chen et al. investigated the product selectivity changes in neat DMF by substituting Co with Fe in a N5 pentadentate bis (imino)pyridine complex (**Co4**). They observed that Co4 primarily produced CO with a faradaic yield (FY) of 82%, while the iron counterpart generated formate. This significant shift in selectivity is crucial for understanding and controlling catalytic processes to favor desired products *(148)*. From the same study, it was found that the cobalt complex demonstrated an overpotential of 566 mV for CO production, based on the electrolysis conditions ($E_{elec.} = -1.5$ V vs SCE), whereas the iron complex exhibited a remarkably low overpotential of 310 mV for formate production ($E_{elec.} = -1.25$ V vs SCE). The same selectivity was observed also under photocatalytic conditions. This underscores the importance of selecting the appropriate metal center to optimize product selectivity and efficiency in CO_2 reduction reactions.

The mechanism proposed for the CO_2R is like the proposed for **Co4**, where the metal complex is initially reduced by two electrons prior reaction with CO_2. Later, a study based on density functional calculations was carried out to uncover the selectivity origin *(149)*. Interestingly, both complexes, **Co4** and the iron homologous, the electronic structure that

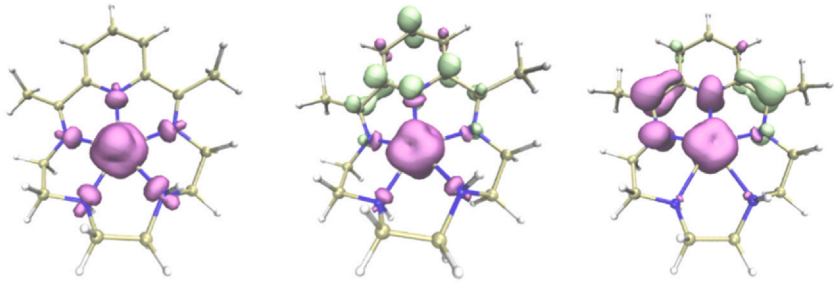

Fig. 28 Spin density plot for the formal oxidation states Co^{II}, Co^{I}, and Co^{0}. Nevertheless, the spin population clearly shows that the reductions are ligand center. A spin electron is shown in purple, and the b spin electrons are in green. *Reprinted from Zhang, Y.-Q.; Wang, Z.-H.; Li, M.; Liao, R.-Z. J. Catal.* ***2022****, 414, 277–293, with permission from Elsevier.*

better describes the systems upon two electron reduction is the oxidation state (II) for the Co and Fe centers, while the ligand gets reduced in two electrons (Fig. 28). The calculated mechanisms are similar than for **Co3** but suggest that the nucleophilic attack to CO_2 takes place by the double-reduced catalyst (formally Co^{0}) or the double reduced and protonated ligand (Fig. 29) to generate the M-CO_2 adduct. Then, internal rearrangement leads to the first CO_2 protonation, followed by a second protonation and C–O cleavage.

Another significant contribution came from the research on carbon nanotube heterogenization of cobalt pyridyldiimine complexes. In this work, derivates of cobalt complex **Co3** functionalized with pyrene were immobilized on multi-walled carbon nanotubes (MWCNTs) and tested in an aqueous carbonate buffer (Fig. 26, **Co3-L1 to Co3-L4**). The heterogenized catalysts demonstrated outstanding stability with turnover numbers exceeding 10,000 and turnover frequencies above $1.2\,s^{-1}$. Notably, the CO selectivity was over 97%, showcasing the potential for high efficiency and specificity in CO_2R *(150)*. The enhanced performance was attributed to the improved mass transport properties and facilitated electron transfer provided by the MWCNTs and the impact of the surface microenvironment on the redox properties of these complexes *(151)*. This research highlights the importance of immobilizing molecular catalysts on conductive supports to develop robust and efficient systems for practical electro- and photo-catalytic applications in CO_2 reduction.

Recently, McCrory and colleagues have introduced a series of non-macrocyclic bis(pyridylmonoimine) complexes (**Co5-Co7**), where the redox-active ligands significantly influence the catalytic performance and

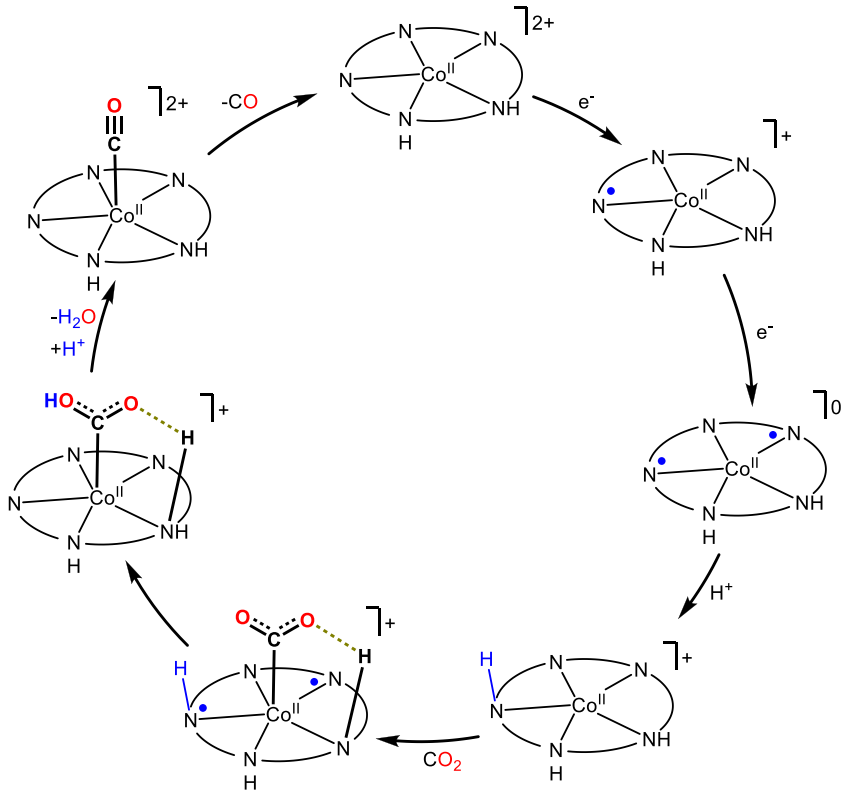

Fig. 29 Proposed mechanism, interesting the assistance of the proton at the ligand.

stability. When Brønsted acid is absent or present in low concentrations, **Co5** exhibits low catalytic efficiency for CO_2 reduction to CO, with a notable amount of formate produced. The team suggests that deprotonation within the Co-CO_2 intermediate causes catalyst deactivation, resulting in formate as a byproduct. Conversely, in the presence of acids (11MH_2O or 5.5 M TFE), **Co5** becomes an effective electrocatalyst for CO_2 reduction to CO. Their findings indicate that a rigid ligand backbone (**Co5**) promotes planar metal dimerization of the catalytic at the Co(I)-Co(I) and Co(I)-Co(0) formal oxidation state pairs, which produces more negative catalytic onset, but higher catalytic activity than the more flexible ligands **Co6** and **Co7**. They also observed that more flexible ligands (**Co6** and **Co7**), imply more positive catalyst onset, but also an increase the affinity of CO to the reduced cobalt complex, leading to catalyst deactivation *(152,153)*. The rigidity of the ligand was attributed as essential for

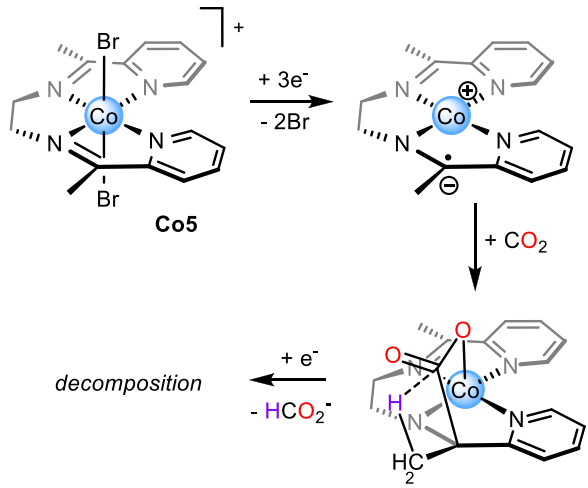

Fig. 30 Proposed decomposition pathway of **Co5**.

achieving higher current and Faradaic efficiency for CO (FE_{CO}), with **Co5** outperforming **Co6** and **Co7**. Nevertheless, regardless of the bridging flexibility of the studied bis(pyridylmonoimine) ligands, the ligand is redox-non innocent and after a Co(II/I) metal center reduction, follows a ligand center one (Co(I)-L/Co(I)-$L^{\cdot-}$), oxidation state that reacts with CO_2 (Fig. 30).

Cobalt complex **Co8** (Fig. 31), utilizing a redox-active imino bipyridyl pincer ligand, stands out among earth-abundant molecular catalysts for its efficiency in catalyzing the electrochemical reduction of CO_2 to formate with a commendable selectivity of 80% *(154)*. The addition of water improves formate production and reduces CO output but also increases H_2 formation, although the Faradaic efficiency (FE) for H_2 production remains below 20%. Comparatively, the symmetrical bis-imino pyridine analog exhibited lower catalytic activity, attributed to reduced conjugation in this system. These findings highlight the critical influence of redox-active ligands on both the efficiency and selectivity of CO_2 reduction reactions (CO_2RR). Based on density functional theory (DFT) calculations and experimental techniques (cyclic voltammetry (CV), electron paramagnetic resonance (EPR), and infrared (IR) spectroscopy), a mechanism has been proposed to explain the formation of both formate and carbon monoxide. The proposed mechanism involves the reduction of the complex to Co^0, which is then protonated by water to form a Co(II) hydride species (CoH). This hydride species reacts with CO_2 to produce a coordinated formate

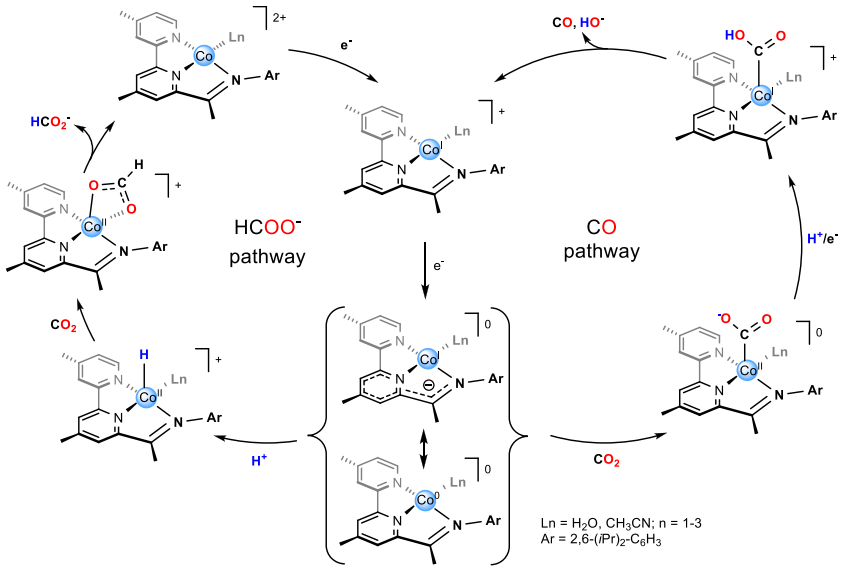

Fig. 31 Proposed CO and formate mechanistic pathways for the bis(pyridylmonoimine) cobalt complex **Co8**.

intermediate, which subsequently dissociates, aided by water or solvent, to regenerate the initial structure. Under anhydrous conditions, Co^0 can directly interact with CO_2 to form a $CoCO_2$ species, leading to CO production. Both formate and CO pathways share the Co^0 and $Co^{0'}$ intermediates, and the redox-active nature of the imino bipyridyl ligand helps delocalize electron density from the metal center to the ligand, favoring the formate pathway. Additionally, the CoH species has a low hydridic character, reducing the likelihood of hydrogen evolution reaction (HER) in the presence of water, thereby enhancing formate selectivity.

3.2 Amino-aminopyridine complexes

A large variety of cobalt catalysts based on aminopyridine ligand have been developed since the first parallel publications of S. L.-F. Chan and C.-M. Che research groups (Fig. 32, **Co9-Co32**) *(155,156)*. These pioneering studies on aminopyridine cobalt complexes underscore the significance of ligand design in achieving efficient and selective CO_2 reduction. They provide foundational knowledge for further development and optimization of molecular catalysts in this field. In the first report (2015), Chan et al. introduced a cobalt complex supported by a tetradentate tripodal ligand (TPA), demonstrating high efficiency in visible-light-driven CO_2

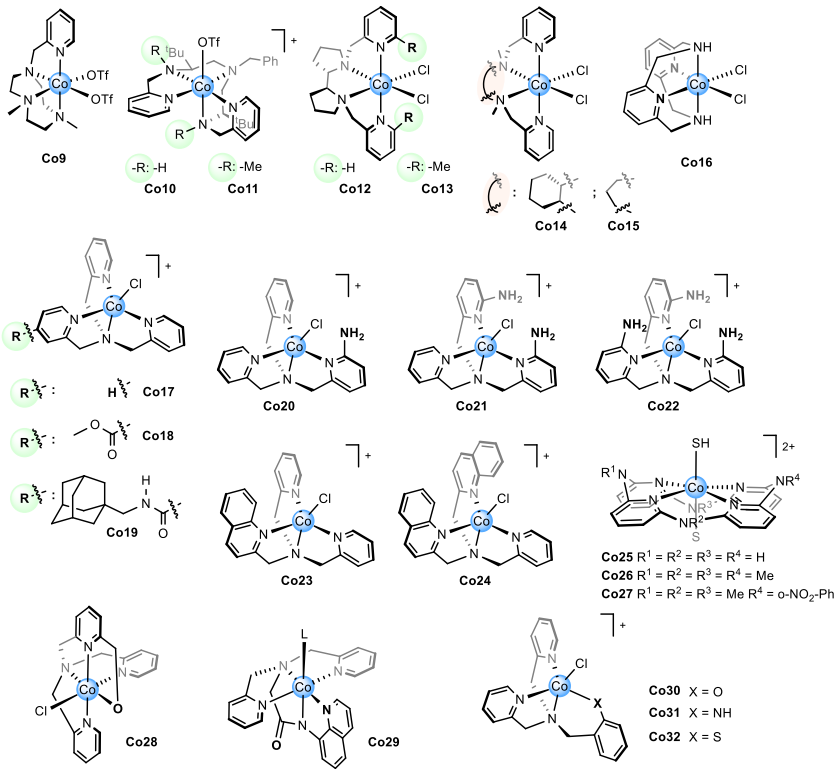

Fig. 32 Selection of aminopyridine complexes. S stands for solvent.

reduction. This complex, [Co(TPA)Cl][Cl] (**Co17**), achieves a turnover number (TON) greater than 900 over 70 h when combined with the photosensitizer $Ir(ppy)_3$ in CO_2-saturated acetonitrile with triethylamine (TEA) as the electron donor. The system exhibits 85% selectivity for CO production, underscoring the effectiveness of the TPA-supported cobalt complex in catalyzing the reduction of CO_2. Mechanistic studies, including electrochemical analysis and time-resolved spectroscopy, revealed that the cobalt complex undergoes reduction to Co(I) species, which then interacts with CO_2 to form CO_2-bound intermediates, ultimately leading to the production of CO. These findings highlight the importance of ligand design in enhancing the catalytic performance and stability of cobalt-based molecular catalysts for CO_2 reduction *(155)*.

Wang et al. *(156)* investigated a series of *cis*-$[Co^{II}(N_4)Cl_2]$ complexes (Fig. 32, **Co12** – **Co15**), focusing on their catalytic activity in the photochemical and electrochemical reduction of CO_2 to CO. Among

the studied complexes, *cis*-[Co^{II}(PDP)Cl_2] (PDP = 1,1′-bis(2-pyridinylmethyl)−2,2′-bipyrrolidine) exhibited the highest catalytic efficiency. Under electrochemical conditions, this complex achieved up to 96% Faraday efficiency for CO production at −1.70 V vs. SCE. In the photocatalytic system, using $Ir(ppy)_3$ as the photosensitizer and triethylamine as the electron donor, the complex demonstrated a selectivity of up to 95% for CO production. The mechanism involves the generation of a Co(I) species through one-electron reduction, which is crucial for CO_2 activation. Ultrafast time-resolved absorption spectroscopy confirmed that photoinduced electron transfer from the excited state of $Ir(ppy)_3$ to the cobalt complex is a key step in forming the active Co(I) species. This study provides detailed insights into the role of chelating N4 ligands in modulating the catalytic activity and stability of cobalt complexes for CO_2 reduction *(156)*.

In general, tetracoordinate aminopyridine cobalt complexes with neutral ligands and *cis* coordination geometry and (Fig. 32, **Co9–Co24**) *(12,35,36,155,156–163)* have shown catalytic activity for CO_2 reduction to CO, modification with anionic groups or pentacoordianted ones also shows promising results. These ligands are known for their high basicity and redox-innocent nature, which facilitates the generation of highly nucleophilic Co(I) intermediates that readily bind to CO_2. The proposed mechanisms for those systems closely resemble those of Ni-cyclam, beginning with the binding of CO_2 to the corresponding M^I intermediate, forming a metal-carboxylate adduct (Fig. 4). Following two protonation steps and a single reduction event, the C–O bond cleavage occurs, resulting in the formation of an M^{II}-CO intermediate that subsequently releases CO *(164–166)*.

Our group has specifically investigated the catalytic behavior of **Co9** in anhydrous acetonitrile and with small amounts of added water (0.5 M) *(35)*. Using IR-SEC, DFT calculations, and labeling studies, we identified the formation of a [Co(I)-CO]+ species even at the non-catalytic Co(II)/Co(I) reduction wave, indicating the process occurs even in the absence of protons (Fig. 33). This finding has significant mechanistic implications:

- CO_2 binds to $[Co(I)]^+$ as can be seen in the CV shift.
- C–O bond cleavage occurs at low overpotentials, at the Co(II/I) redox wave.
- The resulting $[Co^{II}\text{-}CO]^{2+}$ is single reduced to form the thermodynamically more stable intermediate $[Co^{I}\text{-}CO]^{+}$. The intermediate was detected by IR-SEC (ν_{CO} = 1910 cm^{-1}) stretching band shifts 43 cm^{-1} toward lower energy under $^{13}CO_2$ (Fig. 33). DFT calculations show that the release of CO from

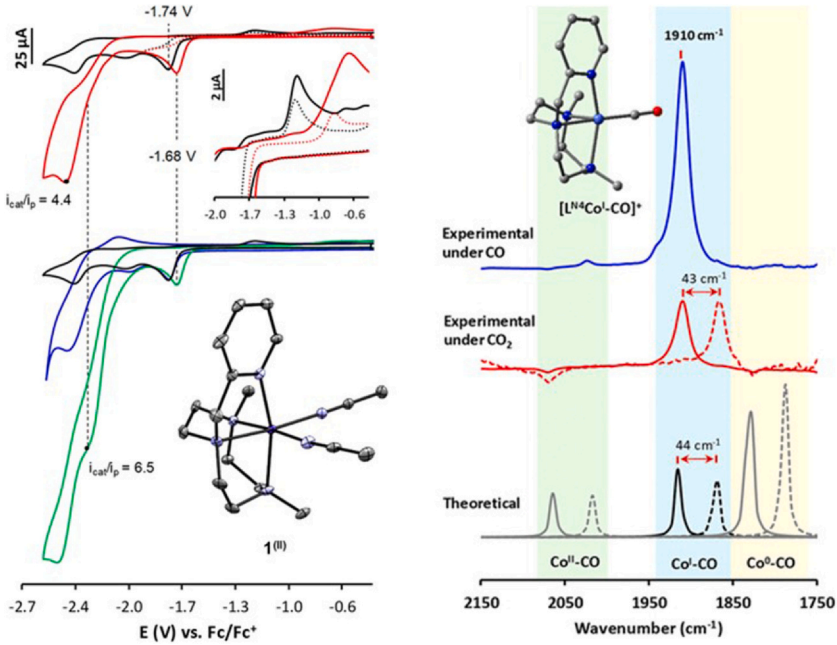

Fig. 33 CV of **Co9** (Left) CVs of **Co9** (1 mM) in anhydrous $TBAPF_6/CH_3CN$ (0.1 M) solution at v = 0.1 V·s–1. (Top) Under Ar (black) and CO_2 (red). (Bottom) Under Ar (black) and with added H_2O (0.55 M) under Ar (blue) and CO_2 (green). Inset: X-ray crystal structure of complex **Co9**; (Right) Top and middle: Experimental FT-IR–SEC of XXX under CO (blue) and CO_2 (red) at ca. – 1.7 V ($^{12}CO_2$ plane, $^{13}CO_2$ dashed). Bottom: Theoretical ν_{CO} bands of **Co9**(II)-CO, **Co9**(I)-CO, and **Co9**(0)-CO ($^{12}CO_2$ red line, $^{13}CO_2$ dashed line) calculated at the B3LYP-D3(SMD)/6–31+G* level of theory. *Reprinted (adapted) with permission from Fernandez, S.; Franco, F.; Casadevall, C.; Martin-Diaconescu, V.; Luis, J. M.; Lloret-Fillol, J. J. Am. Chem. Soc.* ***2020****, 142, 120–133. Copyright 2020 American Chemical Society.*

this intermediate is endergonic and contributes to the kinetic barrier of the mechanism. Thus, we propose an alternative catalytic cycle that begins with the one-electron reduction of $[Co^{I}\text{-}CO]^{+}$, followed by CO_2 binding. Subsequent protonation and reduction steps trigger C–O bond cleavage, resulting in the formation of a Co biscarbonyl species $[Co^{I}(CO)_2]^{+}$, which can dissociate CO (Figs. 34 and 35, blue mechanism).

Co9 exhibits excellent catalytic performance under photocatalytic conditions, which suggests that $[Co^{II}\text{-}CO]^{2+}$ release CO prior $[Co^{I}\text{-}CO]^{+}$ formation. Studies of blue light irradiation under controlled potential electrolysis conditions have shown a positive effect on the catalytic activity,

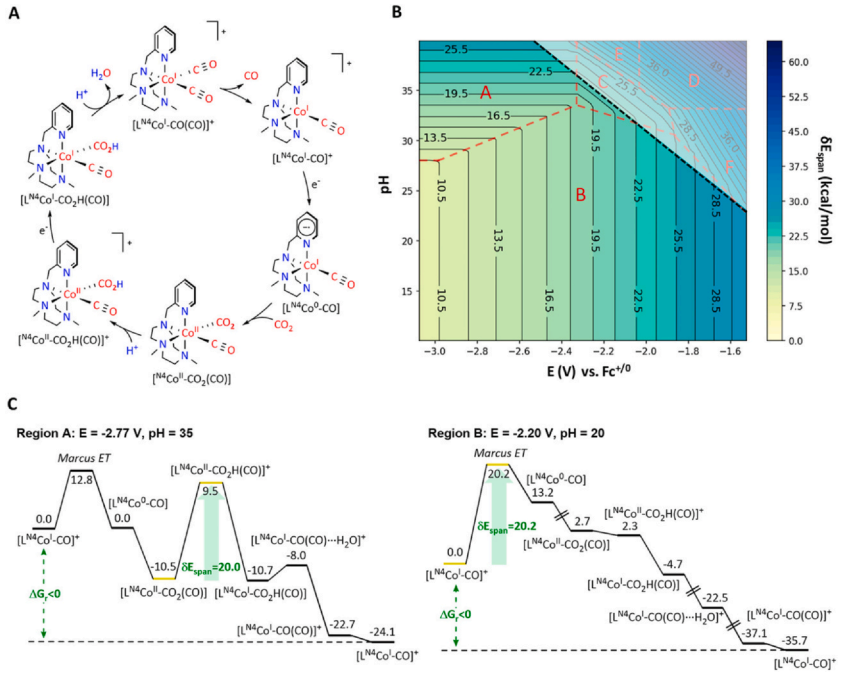

Fig. 34 (A) Proposed reaction mechanism for the CO_2 reduction to CO catalyzed by **Co9**. (B) Contour plots of the kinetic energy span δE_{span} (color scale, kcal·mol^{-1}) of the calculated reaction mechanism versus the applied reduction potential (horizontal axis, V vs Fc/Fc$^+$) and the pH (vertical axis). Regions A–F are delimited by dashed red lines, and the dashed black line spares the thermodynamic ($\Delta G_r < 0$ kcal·mol^{-1}) regime from the non-thermodynamic one ($\Delta Gr > 0$ kcal·mol^{-1}). (C) Gibbs energy profiles associated with regions A and B. *Reprinted (adapted) with permission from Fernandez, S.; Franco, F.; Casadevall, C.; Martin-Diaconescu, V.; Luis, J. M.; Lloret-Fillol, J. J. Am. Chem. Soc.* ***2020****, 142, 1, 120. Copyright 2020 American Chemical Society.*

but also in the selectivity, and durability. A way to rationalize the results is to consider that light can generate an exited state at the cobalt carbonyl intermediates, labializing the Co-CO bond, promoting the CO dissociation, which explains the differences in catalytic activity between photo- and electrocatalytic conditions. This light irradiation effect is even more pronounced for complex **Co10** as it can be clearly seen in CV-light chopped experiments (Fig. 36). Moreover, the catalytic CO production was observed at the Co(II)/Co(I) redox potential *(36)*.

Interestingly, the –NH groups in **Co10** plays a role *(36)*, since the methylated counterpart **Co11** shows a worse catalytic performance. The role of second coordination sphere effect of pendant –NH groups was

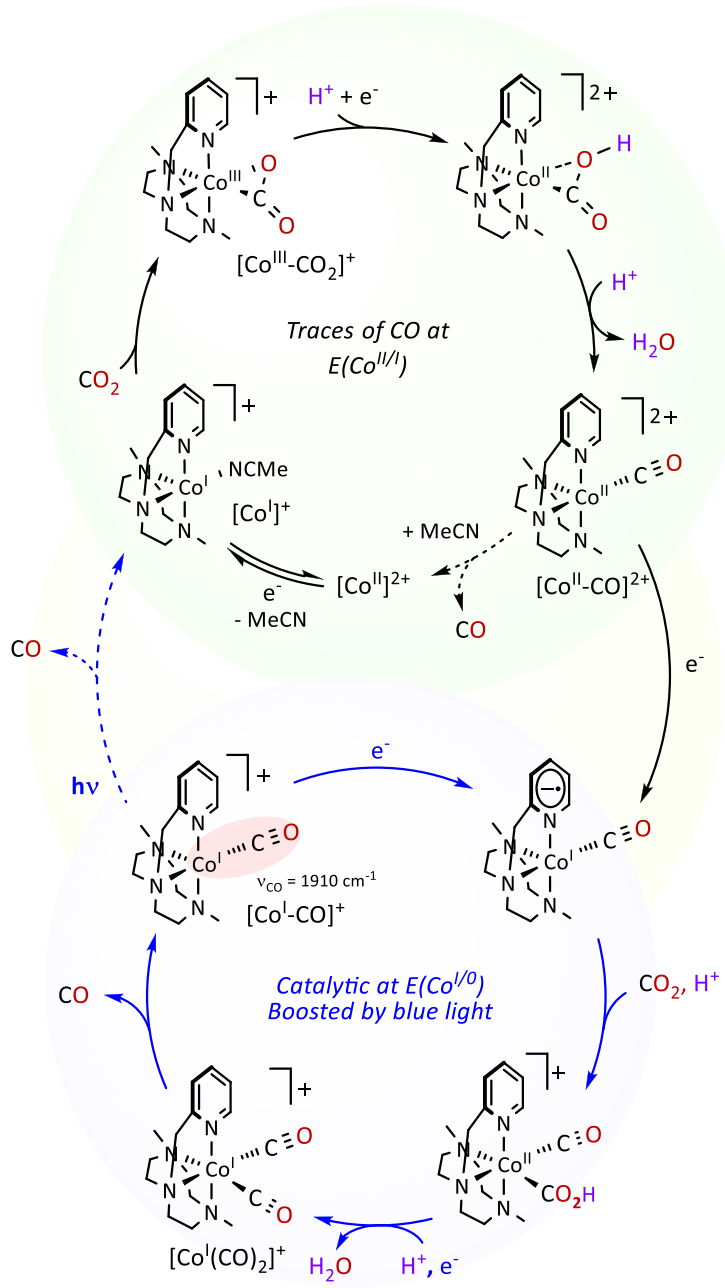

Fig. 35 Mechanistic proposal for both photo- and electrochemical CO_2R to CO catalyzed by **Co9** *(35)*.

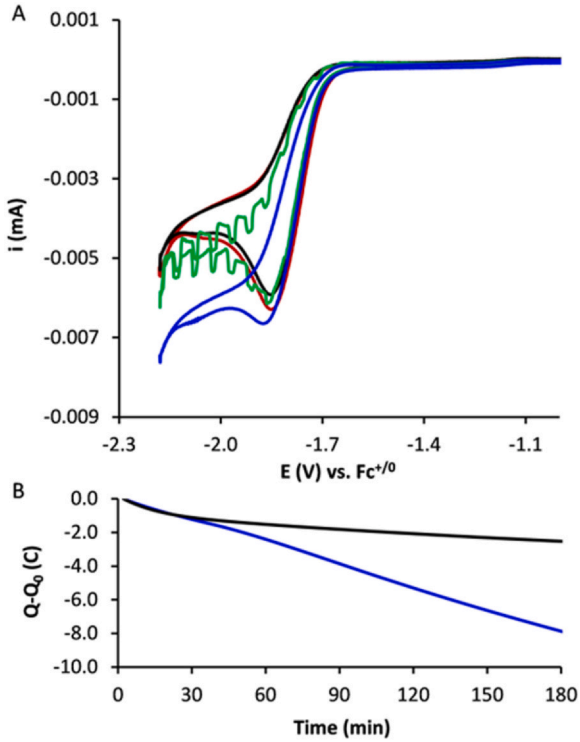

Fig. 36 (A) CV ($0.5\,V \cdot s^{-1}$) of **Co10** in the dark at 22 °C (black), 30 °C (red). CV with chopped light (447 nm, ca. 1 s dark-light cycles, green). CV under 447 nm light irradiation (blue). (B) Charge passed during a CPE in the dark at room temperature (black) and under 447 nm light irradiation (blue). Conditions: CO_2 atmosphere in $TBAPF_6$/CH_3CN (0.1 M) with a 10% of added H_2O over a GC WE disk (ø=0.1 cm) for CV and rod (A=1.8 cm^2) for CPE. *Reprinted (adapted) with permission from reference Fernández, S.; Cañellas, S.; Franco, F.; Luis, J. M.; Pericàs, M. À.; Lloret-Fillol, J. ChemElectroChem,* ***2021****, 8, 4456–4465, Copyright 2021 Wiley-VCH GmbH.*

investigated previously by Marinescu and co-workers with the macrocyclic tetrapyridine-based Co catalyst (**Co25**) *(167)*. Like in our case, the fully methylated counterpart (**Co26**) shows worse catalytic performance *(168,169)*. By DFT calculations, the origin of the catalytic differences was attributed to an intramolecular hydrogen bonding interactions with the TFE forming a [Co^{II}-CO_2H·TFE] adduct (Fig. 37). This result differs from previous proposal, where the expected stabilization of the η^1-CO_2 ligand in the Co-CO_2 adduct is proposed as direct interaction with the -NH groups of the ligand.

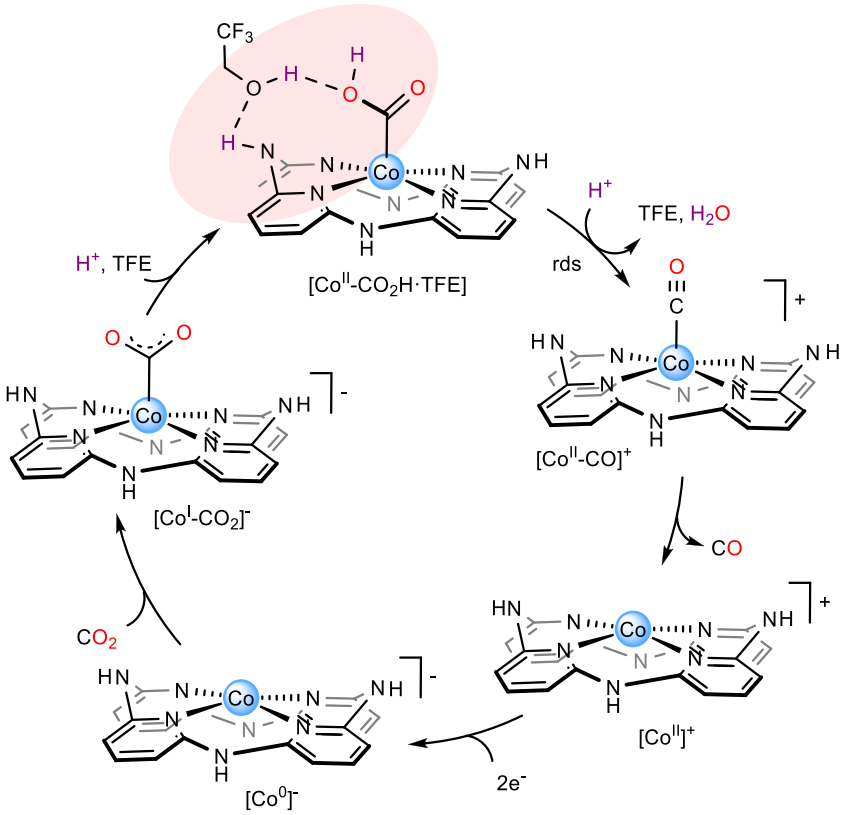

Fig. 37 Proposed mechanism for the CO_2R to CO electrocatalyzed by **Co25**.

Few catalytic systems incorporating cobalt complexes with aminopyridine ligands and anionic ligands have been explored (Fig. 32, **Co28–35**) *(170–172)*. Among these, the **Co28** complex, featuring a pentadentate ligand with an oxygen atom at the cis-coordination site of the labile Cl ligand, demonstrated photocatalytic activity using $Ir(ppy)_3$ as the photosensitizer and Et_3N as the electron donor under visible-light irradiation. The presence of water in the system facilitated the conversion of $2H^+$ to H_2 and CO_2 to HCOOH *(171)*. In a CH_3CN solution without water, the primary products were CO (80%) and H_2 (20%), achieving a total TON of 114. In contrast, using a CH_3CN/H_2O mixed solution with a v(CH_3CN):v(H_2O) ratio of 5:1, the highest total TON of 303 was observed, with a product distribution of 18.8% CO, 60% H_2, and 21.2% formate. Complex **Co29** proved to be an exceptional cobalt-based

photocatalyst for CO_2 reduction in aqueous media, exhibiting significantly higher photocatalytic activity for CO production (TON = 41,017 and TOF = 3.80 s^{-1}) compared to most reported homogeneous catalysts. This result was achieved using $[Ru(bpy)_3]^{2+}$ as the photosensitizer and TEOA as the electron donor *(172)*. Complexes **Co30-Co32** were also capable of reducing CO_2, despite their slightly different coordination environments, though with more moderate catalytic activity *(170)*.

3.3 Catalysts based on polypyridyl ligands

Complexes are based on ligands such as *2,2′*-bipyridine (bpy), *2,2′:6′, 2″*-terpyridine (tpy), *2,2′:6′,2″:6″,2‴*-quaterpyridine (qpy) and their derivatives (Fig. 38) have some characteristic properties due to the nature of the ligand. Those systems tend to be redox non-innocent and the polypyridyl moiety makes them less basic than aminopyridine ligands, both features provide a stabilization of the reduced species, that is going to be reflected in the CO_2R reactivity.

Fontecave and colleagues investigated the catalytic behavior of a series of homoleptic terpyridine (tpy) first-row transition metal complexes. Among these, the $[Co(tpy)_2]^{2+}$ complex (**Co33**) exhibited catalytic activity for CO_2 reduction, achieving a Faradaic efficiency of approximately 20% *(173)*. For the **Co33** complex, the initial electrochemical process is metal-centered, while the subsequent process is ligand-centered. By rationally substituting the tpy ligand with electron-donating tert-butyl (tBu) groups, the researchers minimized the hydrogen evolution reaction, thereby enhancing the selectivity for carbon monoxide (CO) production *(174)*. The proposed electrocatalytic cycle for the reduction of CO_2 and protons (H^+) by **Co33** is depicted in Fig. 39. This cycle involves the formation of active species following the dissociation of a neutral tpy ligand.

The non-redox innocent character is also observed in ligands with bipyridine. For instance, Fujita and co-workers explored the trigonal bipyramidal cobalt complex **Co34,** whereas the active species that react with CO_2 are better represented by the $[Co^{I}L^{\bullet -}]$ electronic structure. Like complex **Co33**, the proposed active species is a cobalt zero, but with the ligand reduced by one electron. The catalytic cycle is triggered by the bidding of CO_2 at the $[Co^{I}L^{\bullet -}]$. This behavior is also observed for catalyst **Co35** and it seems the general behavior of these Co catalysts is based on non-innocent ligand behavior (**Co2–8**, **Co33–48**) *(175–183)*.

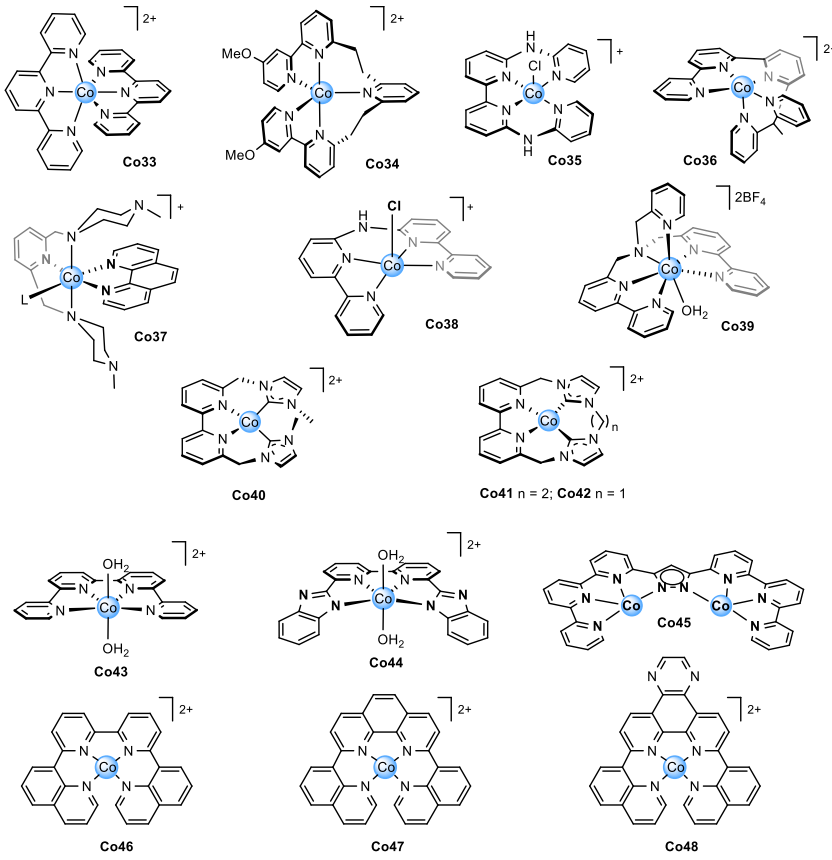

Fig. 38 Selection of CO_2R electrocatalysts based on polypyridyl ligands.

3.3.1 Quaterpyridine ligand and derivates

A noteworthy family of catalytically active cobalt complexes are those based on the quaterpyridine ligand and derivates. Robert, Lau and co-workers showcase that the polypyridine Co complex **Co43** was highly active (TOF_{max} of $3.3{\cdot}10^4$ s^{-1}) and selective to produce CO in acetonitrile when used as a Bronsted acid (PhOH, 3 M) at low overpotential (300 mV) *(184)*. When the catalyst was supported on MWCNTs the catalyst activity and selectivity was extraordinary in aqueous media (pH 7.3). The heterogeneized molecular catalysts has a CO selectivity close to 100% in the overpotential range of 240–440 mV *(185)*. The authors proposed an EEC mechanism for **Co43** based on electroanalysis (Fig. 18) *(186)*, which was corroborated by a computational mechanistic study lead by Head-Gordon

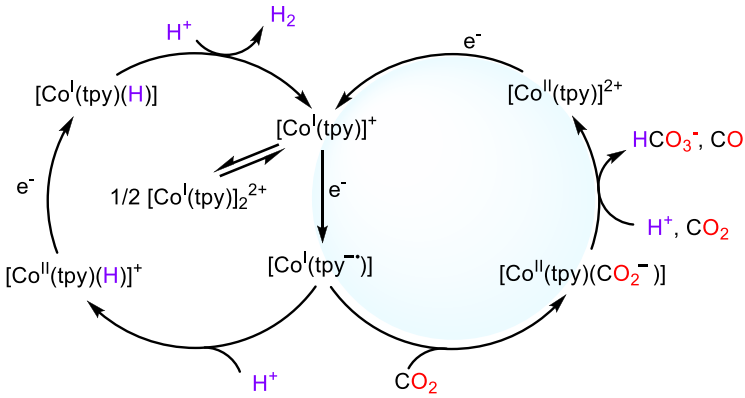

Fig. 39 Simplified version of the proposed mechanism for the electrochemical CO_2 and H^+ reduction catalyzed by **Co33**.

and co-workers, and by G. Dai and co-workers *(187,188)*. From the orbital analysis of one- and two-electron reduced species, they conclude that the second reduction over **Co43** is delocalized onto the metal through metal-ligand bonding interactions. With respect to the metal-carboxylate adduct, according to the DFT analysis, the Lewis acidic character of Co favors the η^1-CO_2 coordination mode (Fig. 40).

In the following study, it was showed that the cobalt-quaterpyridine (Coqpy) molecular complex can be covalently linked to mesoporous graphitic carbon nitride (mpg-C3N4). This hybrid material combines the stability of the semiconductive mpg-C_3N_4 with the catalytic efficiency of the **Co43** complex, achieving a high selectivity for CO production (98%). The catalyst demonstrated remarkable durability, maintaining its activity over 4 days of continuous irradiation, producing approximately 500 turnover number (TON). Efficient electron transfer from mpg-C_3N_4 to the cobalt catalyst was identified as a key factor for its high catalytic performance. Additionally, the catalyst demonstrated excellent recyclability, maintaining its efficiency over multiple cycles *(189)*. Interestingly, the same catalyst showed highly efficient visible-light-driven system for the reduction of CO_2 to CO in water when using an organic triazatriangulenium salt as the photosensitizer. The system employs BIH (1,3-dimethyl-2-phenyl-2,3-dihydro-1H-benzo[*d*]imidazole) and TEOA (triethanolamine) or TEA (triethylamine) as sacrificial reductants. In a CO_2-saturated acetonitrile solution under visible light, the catalyst achieved a turnover number (TON) of over 3700 to produce CO and formate. Adding water enhanced

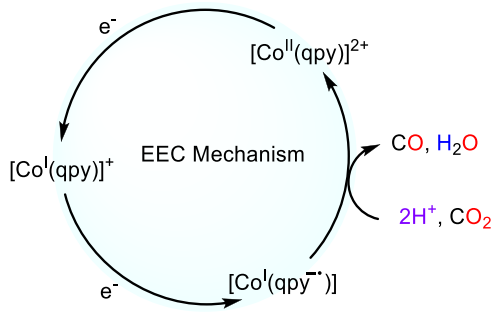

Fig. 40 An experimental-based mechanistic proposal for the electrochemical CO_2R catalyzed by **Co43**.

the catalysis, directing it primarily towards CO production, achieving a TON of 19,000 with 93% selectivity for CO *(190)*. These studies underscore the potential of combining molecular catalysts with photosensitizers and semiconductive materials to develop highly active and durable systems for visible-light-driven CO_2R.

Based on the based flat and rigid cobalt-quaterpyridine geometry, complexes **Co44–Co48** were developed. In those systems, the observed efficient electrocatalytic activity like **Co43**, but complex **Co44**, reported by Tsubonouchi et al. is highly selective electrocatalyst for the reduction of CO_2 to formic acid in DMF solution with 2% of water. The CV studies revealed two reversible redox responses at −1.42 V and −2.32 V vs. Fc/Fc^+, which correspond to the Co(II)/Co(I) and Co(I)/Co(0) transitions, respectively. The catalytic CO2 reduction in the presence of 2.0% water demonstrated high efficiency, with a Faradaic efficiency (FE) of 68% for formic acid (HCOOH) production. This study highlights the potential of quaterpyridine type ligands for developing CO_2R to formic acid catalysts, although the mechanism in the case was not investigated in detail *(179,183,191)*.

3.4 Catalyst design to control selectivity with non-heme macrocyclic, polypyridyl and aminopyridyl complexes

As briefly described in the introduction, a key issue in the development of catalyst for CO_2R is to have good control over product selectivity. One of the reasons for the challenge is the large variety of products that can be formed within close thermochemistry. The thermodynamic energies span from the 2 to the 8 electrons CO_2 reduction products are within less than 400 mVs, being also the hydrogen evolution reaction at about the center of

the span range (Table 1). Therefore, producing a chosen product requires a precise thermodynamic control of reaction intermediates, energy barriers and reaction pathways. Thermodynamic consideration to control the reaction selectivity has been previously discussed *(133,192,193)*. For instance, the free energy of protonation or formation of the metal carboxylate are directly related to the electron-density of the metal centers. The competition between protonation and CO_2 activation is a major challenge for achieving high selectivity. Then, the metal hydride protonation to form H_2 is pka dependent by the reaction with CO_2 not. Therefore, only based on thermodynamic considerations can the reaction of the M-H against protons or CO_2, while more challenging is the reaction of the low oxidation state with protons or CO_2. In this regard, controlling the energy of the kinetic barriers is paramount. Natural enzymatic systems, such as the carbon monoxide dehydrogenase (CODH) enzyme, which efficiently catalyzes the reversible reduction of CO_2 to CO, employs the cooperative interaction between Ni and Fe in CODH's active site as a strategy for achieving efficient catalysis *(194)*. Likewise, secondary interactions can be seen as a powerful concept of cooperative activation, to stabilizes the CO_2-bound intermediate, as a means to lower the activation energy and enhance catalyst performance. Systems that employ similar strategies to improve activity and selectivity. Well-known strategies are introducing hydrogen bonding *(33,129,195–198)* and electrostatic interactions *(199–201)* to stabilize metallo-carboxylate intermediates, favoring the pathway towards CO and bimetallic CO_2 activation *(202–206)*.

Non-heme macrocyclic ligands with aminon imino and pyridyl ligands are synthetically flexible, resulting as an ideal platform to design, implement and test these concepts. In this regard, an early example of secondary interaction was reported by Sutin and co., where they structurally characterized a dicobalt carboxylate complex based on a cyclam type macrocyclic ligand, indicating bimetallic CO_2 activation (Fig. 25, Section 3.1) *(126,207)*. Interestingly, Robert, Lau and coworkers have investigated metal-metal cooperation to force selectivity. In this case, the selectivity was towards formic acid. The authors reported a dimeric version of the active CO_2-to-CO reduction $[Co(qpy)]^{2+}$ electrocatalyst. Using a xanthene bridging scaffold, two $[Co(qpy)]^{2+}$ moieties can be disposed parallelly (**Co49**, Fig. 41) *(208)*.

Under basic photocatalytic conditions, formate was generated selectively. However, in the presence of phenol, the selectivity shifts towards CO. *In situ* IR-SEC revealed a new reaction intermediate, a $4e^-$ reduced CO_2 adduct stabilized by the second Co center, which is proposed to act as a Lewis acid.

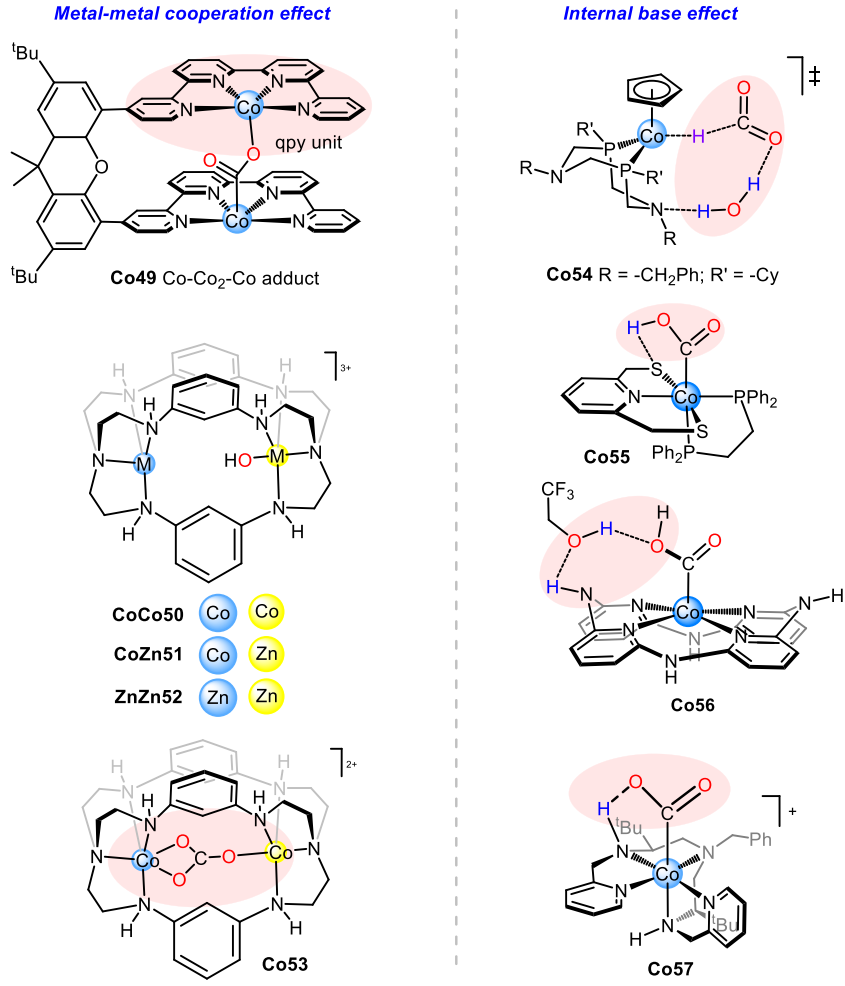

Fig. 41 Selected catalysts with proposed metal-metal and hydrogen bonding interaction to activate the CO_2 and improve the selectivity.

This intermediate was proposed to be common for both, the formation of CO and HCO_2^- (Fig. 41). Under acidic conditions, the typical protonation is followed by C–O bond cleavage, while under basic conditions, potential further reduction leads to carbon protonation, or allowing certain reagent leading to the formate. In a followed-up study showed that the homo-bimetallic copper *bis*-quaterpyridine complex also produce formate with good selectivity 60%. However, the mechanistic studies reveal that the cooperativity between the two copper centers facilitates the formation of a

bridging hydride intermediate in the presence of a proton source (water), which subsequently reacts with CO_2 to produce formate *(209)*.

Lu and co. synthesized a binuclear cobalt cryptate catalyst, **CoCo50**, **CoZn51** and **ZnZn52** to study the metal-metal cooperation to activate the CO_2. Under photocatalytic conditions, **CoCo50** produced CO with 98% selectivity, resulting in a high turnover number (TON) of 16,900 for CO. In contrast, the corresponding monomer, under the same conditions, achieved a TON of only 1600 with 80% CO selectivity. The high catalytic activity of **CoCo50** is attributed to the synergistic effects between the two cobalt centers, which were further enhanced by substituting one Co^{2+} center with Zn^{2+}. This modification resulted in a significant increase in the TON for CO to 65,000 when **CoZn51** was used as the catalyst (Fig. 41), while the **ZnZn52** complex was virtually inactive *(210)*. The mechanism for the photocatalytic reduction of CO_2 by these bimetallic complexes was proposed by DFT calculations. First, the cryptate complex can absorb one CO_2 molecule to form a bicarbonate-cryptate species (like **Co53**), which then undergoes proton-coupled electron transfer to generate $[M^{II}Co^{I}(CO_3H)]^{2+}$. Further protonation of $[M^{II}Co^{I}(CO_3H)]^{2+}$ leads to the loss of H_2O, forming $[M^{II}Co^{I}(CO_2)]^{3+}$. Intramolecular two-electron transfer from the Co^{I} site of to the coordinated CO_2 followed by a proton-coupled electron transfer forms $[M^{II}Co^{II}(COOH)]^{3+}$. Interestingly, the synergistic interaction of the two metals (M and Co) facilitates the cleavage of the C−O bond, by the Co(II) oxidation state, producing $[M^{II}(OH)Co^{II}(CO)]^{3+}$, which releases CO.

Recent studies have underscored the significant role of thiolate ligands in enhancing the catalytic performance of cobalt complexes for CO_2 reduction. Thiolate groups contribute to increased electron density at the metal centers, which is crucial for the activation of CO_2. In the work by Dey et al., a cobalt-dithiolato complex (**Co55**) exhibited high selectivity (~95%) and low overpotential (70 mV) for the reduction of CO_2 to CO. The thiolate ligands not only facilitated CO_2 activation but also played a vital role in protonation processes that lowered the overpotential and ensured efficient proton transfer *(33)*. Similarly, in the research on cobalt-pyridine-thiolate complexes, the thiolate ligands were pivotal in stabilizing the Co(II/I) redox states and enhancing proton-coupled electron transfer (PCET) mechanisms, leading to efficient formate production with low overpotential *(211)*. Another study on a cobalt-pyridine-thiolate complex for CO_2R to CO demonstrated high turnover numbers and selectivity, attributed to the thiolate ligands' ability to stabilize intermediates and facilitate the reduction process *(212)*.

Furthermore, investigations into homobimetallic complexes for visible-light-driven CO_2R revealed that thiolate ligands enhance electron density at the metal centers, promoting CO_2 activation. The cooperative interactions between the metal centers, aided by the thiolate groups, significantly improved the catalytic activity and selectivity for both CO and formate production *(213)*.

Another strategy is the inclusion of hydrogen bonding with NH groups surrounding the catalytic site. As introduced before, when the catalysts have NH groups coordinated to the metal or have difficulty interacting with the metal site, the observed selectivity is towards CO (**Co1, Co3, Co4, Co56** and **Co57**). However, tailoring the second coordination sphere and having the NH group at the appropriate distance could drive to changes in product selectivity. In 2017, Artero and coworkers described new cyclopentadienyl cobalt complexes based on diphosphine ligands functionalized by pendant amine groups (**Co54)** *(214)*. The pendant base at the ligand leads to TS where the hydride is transferred (Fig. 41) through hydrogen bond interactions with a H_2O molecule, enabling a high selectivity towards formate production (98% FE_{HCO2-}).

4. Future perspectives and conclusions

The future of CO_2 reduction catalysis with molecular complexes lies in addressing full understanding of the reaction mechanism. However, the complex nature of the CO_2RR yields multiple products, complicating the generalization of reaction mechanisms. In this regard, coordination complexes are ideal chemical entities to be studied and evolved. The new spectroscopic computational and high throughput techniques part of the CO_2RR have shed light into some aspects of the mechanisms, are the design of some families of catalysts can be rationale, providing faster, more selective and durable catalysts. Leveraging design principles can enhance further our capacity of design. For instance, in the reduction of CO_2 to CO, tuning electronic effects has shown that catalysts with lower overpotentials typically operate at slower rates. To overcome this, strategies that introduce hydrogen bonds or electrostatic interactions have been employed to stabilize M-CO_2 intermediates and facilitate C–O bond cleavage. This through-space stabilization of key intermediates or transition states is crucial for enhancing reaction kinetics, even at lower overpotentials. Although examples of logically tuned catalysts to influence the

critical steps of the catalytic cycle are limited, these principles are applicable to CO_2 reduction to formate, suggesting a need for more rational designs to improve selectivity. The field of CO_2 reduction involving more than two electrons is still emerging, with mechanisms and strategies not yet well-defined. Nonetheless, advancements in mechanistic understanding have proven to be powerful tools in improving CO_2 reduction catalysis.

All this progress has been translated into advanced catalysts. However, although turnover frequencies measured are in the order of millions, turn over numbers are in the order of the tens of thousands, and catalyst, in the best cases last for about 100 h. Photocatalytic systems usually operates at almost homeopathic concentrations, which difficult their applications to energy production or synthetic problems, but may have a niche in biological applications. Regarding electrocatalysts, remarkable progress has been made during the last 10 years. Current densities higher than 100 mA have been achieved directly rivaling with heterogeneous catalysts. Nevertheless, the performance is not at the level needed for industrial application, which is very demanding in terms of durability and activity per catalytic site but also per utilized physical space. Additional understanding of the operative mechanisms and decomposition pathways can help to design a new generation of better catalysts with improved performances. Truly, cobalt complexes for CO_2 reduction have tremendously evolved during last decade, showing that are excellent systems to be study spectroscopically and therefore unraveling its behavior, key intermediates, pitfalls as well as the thermodynamic and kinetic parameters. To advance in the field, more progress is needed in the following key areas:

Innovations in ligand design, multifunctional systems: Continued exploration and development of new ligand frameworks are essential for fine-tuning the electronic properties and stability of metal complexes. Combining several key secondary interactions, such as hydrogen bonding and electrostatic stabilization, will be critical in enhancing catalytic activity and selectivity further. Furthermore, ligands that can provide a robust secondary coordination sphere to stabilize intermediates and transition states beyond the simple stabilization of metal carboxylates will be crucial for advancing CO_2 reduction catalysis. Such as, exploring bimetallic systems and cooperative interactions between metal centers offers a promising strategy for improving catalytic performance. The incorporation of redox-inactive metal sites to enhance electron transfer and stabilize CO_2 adducts has shown significant potential. Further research into the synergistic effects of different metal combinations will help in designing more efficient and selective catalysts.

Mechanistic insights: Gaining a deeper understanding of the mechanistic pathways involved in CO_2 reduction is vital for the rational design of catalysts. Advanced spectroscopic techniques, coupled with computational modeling, will play a significant role in elucidating the key steps and intermediates in the catalytic cycles. This knowledge will enable the development of catalysts with optimized performance and tailored selectivity for desired products.

Selective multi-electron reduction: Achieving high selectivity for higher-order reduction products, such as methanol and formaldehyde, remains a significant challenge. Future research should focus on understanding and controlling the reaction pathways for multi-electron reductions. The design of catalysts that can selectively produce specific products while minimizing by-products will be key to the practical implementation of CO_2 reduction technologies.

Enhancing the stability of CO_2 reduction catalysts is critical for their practical application. This involves not only improving the inherent stability of the catalytic materials but also developing strategies to protect and regenerate catalysts during operation. Studies should focus on understanding degradation mechanisms and designing catalysts that can resist deactivation over long periods. Reticular materials, such as covalent organic frameworks (COFs), represent a promising strategy for improving catalyst stability and performance. COFs offer a highly tunable platform with well-defined porosity and surface areas, facilitating the incorporation of active metal sites and promoting efficient mass transport. The stability and modularity of COFs make them ideal candidates for supporting molecular catalysts and enhancing their durability in CO_2 reduction processes. COFs can provide a robust and stable environment for catalytic centers, preventing aggregation and leaching while maintaining high activity. The integration of COFs with molecular catalysts can lead to the development of hybrid materials that combine the advantages of homogeneous and heterogeneous catalysis, such as well-defined active sites and ease of separation. Moreover, the number of catalytic sites per geometric surface area can be very large due to its intrinsic reticular structure, providing highly dense electrodes which can deliver high current densities.

Integration with renewable energy sources: The development of catalysts that can efficiently operate under visible light or in conjunction with renewable energy sources such as solar or wind is crucial for sustainable CO_2 reduction. Photocatalytic and electrocatalytic systems that

leverage renewable energy will be central to large-scale applications. The integration of these systems into practical devices and reactors will require advancements in catalyst stability and durability. Transitioning from laboratory-scale studies to industrial applications will require the immobilization of molecular catalysts on conductive supports and the design of robust catalytic materials that can withstand long-term operation. A holistic approach and system integration into functional materials, devices (full electrochemical cells) and CO_2 capture will be essential for real-world applications.

In summary, the rational design of cobalt complexes with tailored ligand frameworks, informed by mechanistic insights, offers a promising path forward for developing efficient and selective CO_2 reduction catalysts. Continued research and development in this area are crucial for advancing sustainable CO_2 utilization technologies and contributing to global efforts to mitigate climate change. The future of CO_2 reduction catalysis lies in the integration of these advanced molecular catalysts into practical systems, enabling large-scale applications and driving the transition to a carbon-neutral economy.

References

1. De Luna, P.; Hahn, C.; Higgins, D.; Jaffer, S. A.; Jaramillo, T. F.; Sargent, E. H. *Science* **2019,** *364*, eaav3506.
2. Core Writing Team, H. Lee, J. Romero IPCC, 2023: Sections. In: Climate Change 2023: Synthesis Report. Contribution of Working Groups I, II and III to the Sixth Assessment Report of the Intergovernmental Panel on Climate Change. IPCC, G., Switzerland, Ed. IPCC: Geneva, Switzerland, 2023; pp 35–115.
3. IEA. CO_2 Emissions in 2023, IEA, Paris, 2024. https://www.iea.org/reports/co2-emissions-in-2023, Licence: CC BY 4.0.
4. Solomon, S.; Manning, D.Q.M.; Chen, Z.; Marquis, M.; Averyt, K.B.; Tignor, M.; Miller, H.L. Climate Change 2007: The Physical Science Basis. Contribution of Working Group I to the Fourth Assessment Report of the Intergovernmental Panel on Climate Change. IPCC, C., United Kingdom and New York, Ed., 2007.
5. Monastersky, R. *Nature* **2013,** *497*, 13–14.
6. Cheng, W.; Dan, L.; Deng, X.; Feng, J.; Wang, Y.; Peng, J.; Tian, J.; Qi, W.; Liu, Z.; Zheng, X.; Zhou, D.; Jiang, S.; Zhao, H.; Wang, X. *Scientific Data* **2022,** *9*, 83.
7. Ritchie H.; Rosado P.; Roser M. **2023**. CO_2 and Greenhouse Gas Emissions. Published online at OurWorldInData.org. Retrieved from: https://ourworldindata.org/co2-and-greenhouse-gas-emissions
8. Bhalchandra, M.; Bhanage, M. A. *Transformation and Utilization of Carbon Dioxide;* Springer: Berlin, Heidelberg.
9. Bushuyev, O. S.; De Luna, P.; Dinh, C. T.; Tao, L.; Saur, G.; van de Lagemaat, J.; Kelley, S. O.; Sargent, E. H. *Joule* **2018,** *2*, 825–832.
10. Schneider, J.; Jia, H.; Muckerman, J. T.; Fujita, E. *Chem. Soc. Rev.* **2012,** *41*, 2036–2051.

11. Atkins, P.; Rourke, T. O. J.; Weller, M.; Armstrong, F. *Inorganic Chemistry;* Oxford University Press, Oxford: Oxford, UK.
12. Franco, F.; Fernández, S.; Lloret-Fillol, J. *Curr. Opin. Electrochem.* **2019,** *15*, 109–117.
13. Franco, F.; Rettenmaier, C.; Jeon, H. S.; Roldan Cuenya, B. *Chem. Soc. Rev.* **2020,** *49*, 6884–6946.
14. Boutin, E.; Robert, M. *Trend. Chem.* **2021,** *3*, 359–372.
15. Dalle, K. E.; Warnan, J.; Leung, J. J.; Reuillard, B.; Karmel, I. S.; Reisner, E. *Chem. Rev.* **2019,** *119*, 2752–2875.
16. Wang, M.; Torbensen, K.; Salvatore, D.; Ren, S.; Joulié, D.; Dumoulin, F.; Mendoza, D.; Lassalle-Kaiser, B.; Işci, U.; Berlinguette, C. P.; Robert, M. *Nat. Commun.* **2019,** *10*, 3602.
17. Ren, S.; Joulié, D.; Salvatore, D.; Torbensen, K.; Wang, M.; Robert, M.; Berlinguette Curtis, P. *Science* **2019,** *365*, 367–369.
18. Lin, S.; Diercks, C. S.; Zhang, Y. B.; Kornienko, N.; Nichols, E. M.; Zhao, Y.; Paris, A. R.; Kim, D.; Yang, P.; Yaghi, O. M.; Chang, C. J. *Science* **2015,** *349*, 1208–1213.
19. Dubed Bandomo, G. C.; Mondal, S. S.; Franco, F.; Bucci, A.; Martin-Diaconescu, V.; Ortuño, M. A.; van Langevelde, P. H.; Shafir, A.; López, N.; Lloret-Fillol, J. *ACS Cat.* **2021,** *11*, 7210–7222.
20. Boutin, E.; Merakeb, L.; Ma, B.; Boudy, B.; Wang, M.; Bonin, J.; Anxolabehere-Mallart, E.; Robert, M. *Chem. Soc. Rev.* **2020,** *49*, 5772–5809.
21. Stratakes, B. M.; Dempsey, J. L.; Miller, A. J. M. *ChemElectroChem* **2021,** *8*, 4161–4180.
22. Machan, C. W. *Curr. Opin. Electrochem.* **2019,** *15*, 42–49.
23. Casadevall, C.; Aragón, J.; Cañellas, S.; Pericàs, M. A.; Lloret-Fillol, J.; Caldentey, X. *The Power of High-Throughput Experimentation: General Topics and Enabling Technologies for Synthesis and Catalysis (Volume 1)* **2022**, 145–165. https://doi.org/10.1021/bk-2022-1419.ch009.
24. Fernández, S.; Dubed Bandomo, G. C.; Lloret-Fillol, J. Chapter Eight—Recent advances in electrocatalytic CO_2 reduction with molecular complexes. In *Adv. Inorg. Chem.;* Van Eldik, R.;, Hubbard, C. D., Eds.; Academic Press301–353.
25. Grills, D. C.; Ertem, M. Z.; McKinnon, M.; Ngo, K. T.; Rochford, J. *Coord. Chem. Rev.* **2018,** *374*, 173–217.
26. Lee, G. R.; Maher, J. M.; Cooper, N. J. *J. Am. Chem. Soc.* **1987,** *109*, 2956–2962.
27. Costentin, C.; Drouet, S.; Passard, G.; Robert, M.; Saveant, J. M. *J. Am. Chem. Soc.* **2013,** *135*, 9023–9031.
28. Costentin, C.; Robert, M.; Savéant, J.-M. *Acc. Chem. Res.* **2015,** *48*, 2996–3006.
29. Bonin, J.; Maurin, A.; Robert, M. *Coord. Chem. Rev.* **2017,** *334*, 184–198.
30. Savéant, J.-M. *Chem. Rev.* **2008,** *108*, 2348–2378.
31. Keith, J. A.; Grice, K. A.; Kubiak, C. P.; Carter, E. A. *J. Am. Chem. Soc.* **2013,** *135*, 15823–15829.
32. Su, X.; McCardle, K. M.; Chen, L.; Panetier, J. A.; Jurss, J. W. *ACS Cat.* **2019,** *9*, 7398–7408.
33. Dey, S.; Ahmed, M. E.; Dey, A. *Inorg. Chem.* **2018,** *57*, 5939–5947.
34. Ngo, K. T.; McKinnon, M.; Mahanti, B.; Narayanan, R.; Grills, D. C.; Ertem, M. Z.; Rochford, J. *J. Am. Chem. Soc.* **2017,** *139*, 2604–2618.
35. Fernandez, S.; Franco, F.; Casadevall, C.; Martin-Diaconescu, V.; Luis, J. M.; Lloret-Fillol, J. *J. Am. Chem. Soc.* **2020,** *142*, 120–133.
36. Fernández, S.; Cañellas, S.; Franco, F.; Luis, J. M.; Pericàs, M.À.; Lloret-Fillol, J. *ChemElectroChem* **2021,** *8*, 4456–4465.
37. Manbeck, G. F.; Fujita, E. *J. Porphyrins Phthalocyanines* **2015,** *19*, 45–64.
38. Takahashi, K.; Hiratsuka, K.; Sasaki, H.; Toshima, S. *Chem. Lett.* **1979,** *8*, 305.

39. Behar, D.; Dhanasekaran, T.; Neta, P.; Hosten, C. M.; Ejeh, D.; Hambright, P.; Fujita, E. *J. Phys. Chem. A* **1998,** *102*, 2870–2877.
40. Behar, D.; Dhanasekaran, T.; Neta, P.; Hosten, C. M.; Ejeh, D.; Hambright, P.; Fujita, E. *J. Phys. Chem. A* **1998,** *102*, 2870.
41. Zhu, M.; Yang, D.-T.; Ye, R.; Zeng, J.; Corbin, N.; Manthiram, K. *Catal. Sci. Technol.* **2019,** *9*, 974–980.
42. Bochlin, Y.; Korin, E.; Bettelheim, A. *ACS Appl. Energy Mater.* **2019,** *2*, 8434–8440.
43. Shen, J.; Kortlever, R.; Kas, R.; Birdja, Y. Y.; Diaz-Morales, O.; Kwon, Y.; Ledezma-Yanez, I.; Schouten, K. J. P.; Mul, G.; Koper, M. T. M. *Nat. Commun.* **2015,** *6*, 8177.
44. Shen, J.; Kolb, M. J.; Göttle, A. J.; Koper, M. T. M. *J. Phys. Chem. C* **2016,** *120*, 15714–15721.
45. Hansch, C.; Leo, A.; Taft, R. W. *Chem. Rev.* **1991,** *91*, 165–195.
46. Hu, X.-M.; Rønne, M. H.; Pedersen, S. U.; Skrydstrup, T.; Daasbjerg, K. *Angew. Chem. Int. Ed.* **2017,** *56*, 6468–6472.
47. Sonoyama, N.; Kirii, M.; Sakata, T. *Electrochem. Commun.* **1999,** *1*, 213.
48. Enoki, O.; Imaoka, T.; Yamamoto, K. *Macromol. Symp.* **2003,** *204*, 151.
49. Imaoka, T.; Tanaka, R.; Yamamoto, K. *J. Polym. Sci. Part A: Polym. Chem.* **2006,** *44*, 5229–5236.
50. Leung, K.; Nielsen, I. M. B.; Sai, N.; Medforth, C.; Shelnutt, J. A. *J. Phys. Chem. A* **2010,** *114*, 10174–10184.
51. Zhu, G.; Li, Y.; Zhu, H.; Su, H.; Chan, S. H.; Sun, Q. *ACS Cat.* **2016,** *6*, 6294–6301.
52. Aoi, S.; Mase, K.; Ohkubo, K.; Fukuzumi, S. *Chem. Commun. (Camb)* **2015,** *51*, 10226–10228.
53. Shen, J.; Kortlever, R.; Kas, R.; Birdja, Y. Y.; Diaz-Morales, O.; Kwon, Y.; Ledezma-Yanez, I.; Schouten, K. J. P.; Mul, G.; Koper, M. T. M. *Nat. Commun.* **2015,** *6*, 8177.
54. Yao, C. L.; Li, J. C.; Gao, W.; Jiang, Q. *Phys. Chem. Chem. Phys.* **2017,** *19*, 15067–15072.
55. Göttle, A. J.; Koper, M. T. M. *Chem. Sci.* **2017,** *8*, 458–465.
56. Marianov, A. N.; Jiang, Y. *Appl. Catal. B Environ.* **2019,** *244*, 881–888.
57. Atoguchi, T.; Aramata, A.; Kazusaka, A.; Enyo, M. *J. Chem. Soc. Chem. Commun.* **1991**, 156–157.
58. Tanaka, H.; Aramata, A. *J. Electroanal. Chem.* **1997,** *437*, 29–35.
59. Quezada, D.; Honores, J.; García, M.; Armijo, F.; Isaacs, M. *N. J. Chem.* **2014,** *38*, 3606–3612.
60. Soto, M.; Gotor-Fernández, V.; Rodríguez-Solla, H.; Baratta, W. *ChemCatChem* **2021,** *13*, 2152–2157.
61. Yao, S. A.; Ruther, R. E.; Zhang, L.; Franking, R. A.; Hamers, R. J.; Berry, J. F. *J. Am. Chem. Soc.* **2012,** *134*, 15632.
62. Cao, L.; Wang, C. *ACS Cent. Sci.* **2020,** *6*, 2149–2158.
63. Diercks, C. S.; Lin, S.; Kornienko, N.; Kapustin, E. A.; Nichols, E. M.; Zhu, C.; Zhao, Y.; Chang, C. J.; Yaghi, O. M. *J. Am. Chem. Soc.* **2018,** *140*, 1116–1122.
64. Wang, Y.-R.; Huang, Q.; He, C.-T.; Chen, Y.; Liu, J.; Shen, F.-C.; Lan, Y.-Q. *Nat. Commun.* **2018,** *9*, 4466.
65. Kornienko, N.; Zhao, Y.; Kley, C. S.; Zhu, C.; Kim, D.; Lin, S.; Chang, C. J.; Yaghi, O. M.; Yang, P. *J. Am. Chem. Soc.* **2015,** *137*, 14129.
66. An, S.; Lu, C.; Xu, Q.; Lian, C.; Peng, C.; Hu, J.; Zhuang, X.; Liu, H. *ACS Energy Lett.* **2021,** *6*, 3496–3502.
67. Johnson, E. M.; Haiges, R.; Marinescu, S. C. *ACS Appl. Mater. Interfaces.* **2018,** *10*, 37919–37927.

68. Liang, Z.; Qu, C.; Xia, D.; Zou, R.; Xu, Q. *Angew. Chem. Int. Ed.* **2018,** *57*, 9604–9633.
69. Dubed Bandomo, G. C.; Franco, F.; Liu, C.; Mondal, S. S.; Gallo, A.; Nervi, C.; Lloret-Fillol, J. *ACS Appl. Energy Mater.* **2024,** *7*, 1348–1357.
70. Zhu, M.; Chen, J.; Huang, L.; Ye, R.; Xu, J.; Han, Y.-F. *Angew. Chem. Int. Ed.* **2019,** *58*, 6595–6599.
71. Pander, J. E.; Fogg, A.; Bocarsly, A. B. *ChemCatChem* **2016,** *8*, 3536.
72. Call, A.; Cibian, M.; Yamamoto, K.; Nakazono, T.; Yamauchi, K.; Sakai, K. *ACS Cat.* **2019,** *9*, 4867–4874.
73. Zhang, X.; Cibian, M.; Call, A.; Yamauchi, K.; Sakai, K. *ACS Cat.* **2019,** *9*, 11263–11273.
74. Diercks, C. S.; Lin, S.; Kornienko, N.; Kapustin, E. A.; Nichols, E. M.; Zhu, C.; Zhao, Y.; Chang, C. J.; Yaghi, O. M. *J. Am. Chem. Soc.* **2018,** *140*, 1116.
75. Dong, H.; Lu, M.; Wang, Y.; Tang, H.-L.; Wu, D.; Sun, X.; Zhang, F.-M. *Appl. Catal. B Environ.* **2022,** *303*, 120897.
76. Kornienko, N.; Zhao, Y.; Kley, C. S.; Zhu, C.; Kim, D.; Lin, S.; Chang, C. J.; Yaghi, O. M.; Yang, P. *J. Am. Chem. Soc.* **2015,** *137*, 14129–14135.
77. Guo, Y.; Shi, W.; Yang, H.; He, Q.; Zeng, Z.; Ye, J. Y.; He, X.; Huang, R.; Wang, C.; Lin, W. *J. Am. Chem. Soc.* **2019,** *141*, 17875–17883.
78. Zhang, X.-D.; Hou, S.-Z.; Wu, J.-X.; Gu, Z.-Y. *Chem. Eur. J.* **2020,** *26*, 1604–1611.
79. Yue, Z.; Ou, C.; Ding, N.; Tao, L.; Zhao, J.; Chen, J. *ChemCatChem* **2020,** *12*, 6103–6130.
80. Mahmood, M. N.; Masheder, D.; Harty, C. J. *J. Appl. Electrochem.* **1987,** *17*, 1223–1227.
81. Latiff, N. M.; Fu, X.; Mohamed, D. K.; Veksha, A.; Handayani, M.; Lisak, G. *Carbon* **2020,** *168*, 245–253.
82. Karapinar, D.; Zitolo, A.; Huan, T. N.; Zanna, S.; Taverna, D.; Galvão Tizei, L. H.; Giaume, D.; Marcus, P.; Mougel, V.; Fontecave, M. *ChemSusChem* **2020,** *13*, 173–179.
83. Lieber, C. M.; Lewis, N. S. *J. Am. Chem. Soc.* **1984,** *106*, 5033–5034.
84. Zhu, M.; Chen, J.; Guo, R.; Xu, J.; Fang, X.; Han, Y.-F. *Appl. Catal. B Environ.* **2019,** *251*, 112–118.
85. Meshitsuka, S.; Ichikawa, M.; Tamaru, K. *J. Chem. Soc. Chem. Commun.* **1974**, 158–159.
86. Hiratsuka, K.; Takahashi, K.; Sasaki, H.; Toshima, S. *Chem. Lett.* **1977,** *6*, 1137.
87. Lieber, C. M.; Lewis, N. S. *J. Am. Chem. Soc.* **1984,** *106*, 5033.
88. Mahmood, M. N.; Masheder, D.; Harty, C. J. *J. Appl. Electrochem.* **1987,** *17*, 1223.
89. Furuya, N.; Matsui, K. *J. Electroanal. Chem. Interfacial Electrochem.* **1989,** *271*, 181.
90. Zhang, J.; Pietro, W. J.; Lever, A. B. P. *J. Electroanal. Chem.* **1996,** *403*, 93–100.
91. Abe, T.; Taguchi, F.; Yoshida, T.; Tokita, S.; Schnurpfeil, G.; Wöhrle, D.; Kaneko, M. *J. Mol. Catal. A: Chem.* **1996,** *112*, 55–61.
92. Yoshida, T.; Kamato, K.; Tsukamoto, M.; Iida, T.; Schlettwein, D.; Wöhrle, D.; Kaneko, M. *J. Electroanal. Chem.* **1995,** *385*, 209.
93. Abe, T.; Yoshida, T.; Tokita, S.; Taguchi, F.; Imaya, H.; Kaneko, M. *J. Electroanal. Chem.* **1996,** *412*, 125.
94. Kramer, W. W.; McCrory, C. C. L. *Chem. Sci.* **2016,** *7*, 2506.
95. Liu, Y.; McCrory, C. C. L. *Nat. Commun.* **2019,** *10*, 1683.
96. Zhu, M.; Ye, R.; Jin, K.; Lazouski, N.; Manthiram, K. *ACS Energy Lett.* **2018,** *3*, 1381.
97. Jiang, Z.; Wang, Y.; Zhang, X.; Zheng, H.; Wang, X.; Liang, Y. *Nano Res.* **2019,** *12*, 2330–2334.
98. Yang, S.; Yu, Y.; Gao, X.; Zhang, Z.; Wang, F. *Chem. Soc. Rev.* **2021,** *50*, 12985–13011.

99. Meshitsuka, S.; Ichikawa, M.; Tamaru, K. *J. Chem. Soc. Chem. Commun.* **1974**, 158.
100. Li, F.; MacFarlane, D. R.; Zhang, J. *Nanoscale* **2018,** *10*, 6235–6260.
101. Xu, H.; Cai, H.; Cui, L.; Yu, L.; Gao, R.; Shi, C. *Nano Res.* **2023,** *16*, 3649–3657.
102. Choi, J.; Wagner, P.; Gambhir, S.; Jalili, R.; MacFarlane, D. R.; Wallace, G. G.; Officer, D. L. *ACS Energy Lett.* **2019,** *4*, 666–672.
103. Han, N.; Wang, Y.; Ma, L.; Wen, J.; Li, J.; Zheng, H.; Nie, K.; Wang, X.; Zhao, F.; Li, Y.; Fan, J.; Zhong, J.; Wu, T.; Miller, D. J.; Lu, J.; Lee, S.-T.; Li, Y. *Chemistry* **2017,** *3*, 652–664.
104. Chen, J.; Li, J.; Liu, W.; Ma, X.; Xu, J.; Zhu, M.; Han, Y.-F. *Green Chem.* **2019,** *21*, 6056–6061.
105. Wu, H.; Zeng, M.; Zhu, X.; Tian, C.; Mei, B.; Song, Y.; Du, X.-L.; Jiang, Z.; He, L.; Xia, C.; Dai, S. *ChemElectroChem* **2018,** *5*, 2717–2721.
106. Isaacs, M.; Armijo, F.; Ramírez, G.; Trollund, E.; Biaggio, S. R.; Costamagna, J.; Aguirre, M. J. *J. Mol. Catal. A: Chem.* **2005,** *229*, 249.
107. Roy, S.; Reisner, E. *Angew. Chem. Int. Ed.* **2019,** *58*, 12180–12184.
108. Morlanés, N.; Takanabe, K.; Rodionov, V.; Catal, A. C. S. **2016,** *6*, 3092.
109. Zhang, X.; Wu, Z.; Zhang, X.; Li, L.; Li, Y.; Xu, H.; Li, X.; Yu, X.; Zhang, Z.; Liang, Y.; Wang, H. *Nat. Commun.* **2017,** *8*, 14675.
110. Matheu, R.; Gutierrez-Puebla, E.; Monge, M.Á.; Diercks, C. S.; Kang, J.; Prévot, M. S.; Pei, X.; Hanikel, N.; Zhang, B.; Yang, P.; Yaghi, O. M. *J. Am. Chem. Soc.* **2019,** *141*, 17081–17085.
111. Yang, Z.; Zhang, X.; Long, C.; Yan, S.; Shi, Y.; Han, J.; Zhang, J.; An, P.; Chang, L.; Tang, Z. *CrystEngComm* **2020,** *22*, 1619–1624.
112. Magdesieva, T. V.; Zhukov, I. V.; Kravchuk, D. N.; Semenikhin, O. A.; Tomilova, L. G.; Butin, K. P. *Russ. Chem. Bull.* **2002,** *51*, 805–812.
113. Wu, Y.; Jiang, Z.; Lu, X.; Liang, Y.; Wang, H. *Nature* **2019,** *575*, 639–642.
114. Boutin, E.; Wang, M.; Lin, J. C.; Mesnage, M.; Mendoza, D.; Lassalle-Kaiser, B.; Hahn, C.; Jaramillo, T. F.; Robert, M. *Angew. Chem. Int. Ed.* **2019,** *58*, 16172–16176.
115. Lu, X.; Wu, Y.; Yuan, X.; Huang, L.; Wu, Z.; Xuan, J.; Wang, Y.; Wang, H. *ACS Energy Lett.* **2018,** *3*, 2527–2532.
116. Ren, S.; Joulié, D.; Salvatore, D.; Torbensen, K.; Wang, M.; Robert, M.; Berlinguette, C. P. *Science* **2019,** *365*, 367–369.
117. Ren, S.; Joulié, D.; Salvatore, D.; Torbensen, K.; Wang, M.; Robert, M.; Berlinguette, C. P. *Science* **2019,** *365*, 367–369.
118. Kutz, R. B.; Chen, Q.; Yang, H.; Sajjad, S. D.; Liu, Z.; Masel, I. R. *Energy Technol.* **2017,** *5*, 929–936.
119. Grodkowski, J.; Neta, P.; Fujita, E.; Mahammed, A.; Simkhovich, L.; Gross, Z. *J. Phys. Chem. A* **2002,** *106*, 4772.
120. Gonglach, S.; Paul, S.; Haas, M.; Pillwein, F.; Sreejith, S. S.; Barman, S.; De, R.; Müllegger, S.; Gerschel, P.; Apfel, U.-P.; Coskun, H.; Aljabour, A.; Stadler, P.; Schöfberger, W.; Roy, S. *Nat. Commun.* **2019,** *10*, 3864.
121. Grodkowski, J.; Neta, P. *J. Phys. Chem. A* **2000,** *104*, 1848.
122. Fisher, B. J.; Eisenberg, R. *J. Am. Chem. Soc.* **1980,** *102*, 7361–7363.
123. Gangi, D. A.; Durand, R. R. *J. Chem. Soc. Chem. Commun.* **1986**, 697–699.
124. Creutz, C.; Schwarz, H. A.; Wishart, J. F.; Fujita, E.; Sutin, N. *J. Am. Chem. Soc.* **1991,** *113*, 3361–3371.
125. Fujita, E.; Creutz, C.; Sutin, N.; Szalda, D. J. *J. Am. Chem. Soc.* **1991,** *113*, 343.
126. Fujita, E.; Szalda, D. J.; Creutz, C.; Sutin, N. *J. Am. Chem. Soc.* **1988,** *110*, 4870.
127. Ogata, T.; Yanagida, S.; Brunschwig, B. S.; Fujita, E. *Energy Convers. Manage.* **1995,** *36*, 669.

128. Creutz, C.; Schwarz, H. A.; Wishart, J. F.; Fujita, E.; Sutin, N. *J. Am. Chem. Soc.* **1991,** *113*, 3361.
129. Fujita, E.; Creutz, C.; Sutin, N.; Brunschwig, B. S. *Inorg. Chem.* **1993,** *32*, 2657.
130. Fujita, E.; Furenlid, L. R.; Renner, M. W. *J. Am. Chem. Soc.* **1997,** *119*, 4549.
131. Fujita, E.; Van Eldik, R. *Inorg. Chem.* **1998,** *37*, 360–362.
132. Fujita, E.; Furenlid, L. R.; Renner, M. W. *J. Am. Chem. Soc.* **1997,** *119*, 4549–4550.
133. Schneider, J.; Jia, H.; Muckerman, J. T.; Fujita, E. *Chem. Soc. Rev.* **2012,** *41*, 2036.
134. Fachinetti, G.; Floriani, C.; Zanazzi, P. F. *J. Am. Chem. Soc.* **1978,** *100*, 7405–7407.
135. Fujita, E.; Szalda, D. J.; Creutz, C.; Sutin, N. *J. Am. Chem. Soc.* **2002,** *110*, 4870–4871.
136. Szalda, D. J.; Fujita, E.; Creutz, C. *Inorg. Chem.* **1989,** *28*, 1446–1450.
137. Polyansky, D. E.; Grills, D. C.; Ertem, M. Z.; Ngo, K. T.; Fujita, E. *ACS Cat.* **2022,** *12*, 1706–1717.
138. Arana, C.; Yan, S.; Keshavarz-K, M.; Potts, K. T.; Abruna, H. D. *Inorg. Chem.* **2002,** *31*, 3680–3682.
139. Che, C.-M.; Mak, S.-T.; Lee, W.-O.; Fung, K.-W.; Mak, T. C. W. *J. Chem. Soc. Dalton Trans.* **1988**, 2153–2159.
140. Tinnemans, A. H. A.; Koster, T. P. M.; Thewissen, D. H. M. W.; Mackor, A. *Recl. Trav. Chim. Pays-Bas* **1984,** *103*, 288.
141. Fisher, B. J.; Eisenberg, R. *J. Am. Chem. Soc.* **1980,** *102*, 7361.
142. Lacy, D. C.; McCrory, C. C. L.; Peters, J. C. *Inorg. Chem.* **2014,** *53*, 4980–4988.
143. Sheng, H.; Frei, H. *J. Am. Chem. Soc.* **2016,** *138*, 9959–9967.
144. Zhang, M.; El-Roz, M.; Frei, H.; Mendoza-Cortes, J. L.; Head-Gordon, M.; Lacy, D. C.; Peters, J. C. *J. Phys. Chem. C* **2015,** *119*, 4645.
145. Sheng, H.; Frei, H. *J. Am. Chem. Soc.* **2016,** *138*, 9959.
146. Garza, A. J.; Pakhira, S.; Bell, A. T.; Mendoza-Cortes, J. L.; Head-Gordon, M. *Phys. Chem. Chem. Phys.* **2018,** *20*, 24058–24064.
147. Zhou, J.; Nie, W.; Tarnopol, D. E.; McCrory, C. C. L. *Chem. Catal.* **2024,** *4*.
148. Chen, L.; Guo, Z.; Wei, X.-G.; Gallenkamp, C.; Bonin, J.; Anxolabéhère-Mallart, E.; Lau, K.-C.; Lau, T.-C.; Robert, M. *J. Am. Chem. Soc.* **2015,** *137*, 10918–10921.
149. Zhang, Y.-Q.; Wang, Z.-H.; Li, M.; Liao, R.-Z. *J. Catal.* **2022,** *414*, 277–293.
150. Andrin, B.; Marques Cordeiro Junior, P. J.; Provost, D.; Diring, S.; Pellegrin, Y.; Robert, M.; Odobel, F. *Chem. Commun. (Camb)* **2024,** *60*, 5022–5025.
151. Haake, M.; Aldakov, D.; Pérard, J.; Veronesi, G.; Tapia, A. A.; Reuillard, B.; Artero, V. *J. Am. Chem. Soc.* **2024,** *146*, 15345–15355.
152. Nie, W.; Wang, Y.; Zheng, T.; Ibrahim, A.; Xu, Z.; McCrory, C. C. L. *ACS Cat.* **2020,** *10*, 4942–4959.
153. Nie, W.; McCrory, C. C. L. *Chem. Commun.* **2018,** *54*, 1579.
154. Liu, F.-W.; Bi, J.; Sun, Y.; Luo, S.; Kang, P. *ChemSusChem* **2018,** *11*, 1656–1663.
155. Chan, S. L.-F.; Lam, T. L.; Yang, C.; Yan, S.-C.; Cheng, N. M. *Chem. Commun.* **2015,** *51*, 7799–7801.
156. Wang, F.; Cao, B.; To, W. P.; Tse, C. W.; Li, K.; Chang, X. Y.; Zang, C.; Chan, S. L. F.; Che, C. M. *Catal. Sci. Technol.* **2016,** *6*, 7408.
157. Bairagi, A.; Pereverzev, A. Y.; Tinnemans, P.; Pidko, E. A.; Roithova, J. *J. Am. Chem. Soc.* **2024,** *146*, 5480–5492.
158. Call, A.; Codolà, Z.; Acuña-Parés, F.; Lloret-Fillol, J. *Chem. Eur. J.* **2014,** *20*, 6171–6183.
159. Call, A.; Franco, F.; Kandoth, N.; Fernández, S.; González-Béjar, M.; Pérez-Prieto, J.; Luis, J. M.; Lloret-Fillol, J. *Chem. Sci.* **2018,** *9*, 2609–2619.
160. Sakaguchi, Y.; Call, A.; Yamauchi, K.; Sakai, K. *Dalton Trans.* **2021,** *50*, 15983–15995.

161. Wang, J. W.; Huang, H. H.; Sun, J. K.; Ouyang, T.; Zhong, D. C.; Lu, T. B. *ChemSusChem* **2018,** *11*, 1025–1031.
162. Yang, Y.; Xie, F.; Chen, J.; Qiu, S.; Qiang, N.; Lu, M.; Peng, Z.; Yang, J.; Liu, G. *Molecules* **2024,** *29*.
163. Zhu, C.-Y.; Huang, Y.-C.; Hu, J.-C.; Li, Q.-K.; Tan, H.; Gui, M.-X.; Deng, S.-F.; Wang, F. *J. Photoch. Photobio. A* **2018,** *355*, 175–179.
164. Wang, F.; Cao, B.; To, W.-P.; Tse, C.-W.; Li, K.; Chang, X.-Y.; Zang, C.; Chan, S. L.-F.; Che, C.-M. *Catal. Sci. Technol.* **2016,** *6*, 7408–7420.
165. Wang, J.-W.; Huang, H.-H.; Sun, J.-K.; Ouyang, T.; Zhong, D.-C.; Lu, T.-B. *ChemSusChem* **2018,** *11*, 994.
166. Wang, J.-W.; Huang, H.-H.; Sun, J.-K.; Zhong, D.-C.; Lu, T.-B. *ACS Cat.* **2018,** *8*, 7612–7620.
167. Chapovetsky, A.; Do, T. H.; Haiges, R.; Takase, M. K.; Marinescu, S. C. *J. Am. Chem. Soc.* **2016,** *138*, 5765–5768.
168. Chapovetsky, A.; Welborn, M.; Luna, J. M.; Haiges, R.; Miller, T. F.; Marinescu, S. C. *ACS Cent. Sci.* **2018,** *4*, 397–404.
169. Johnson, E. M.; Liu, J. J.; Samuel, A. D.; Haiges, R.; Marinescu, S. C. *Inorg. Chem.* **2022,** *61*, 1316–1326.
170. Wang, Y.; Zhang, J.; Yang, W.; Tao, W.; Tao, K.; Deng, J.; Shi, W.; Zhong, D.; Lu, T. *Chin. J. Chem.* **2023,** *41*, 3305–3310.
171. Zhu, C.-Y.; Zhang, Y.-Q.; Liao, R.-Z.; Xia, W.; Hu, J.-C.; Wu, J.; Liu, H.; Wang, F. *Dalton Trans.* **2018,** *47*, 13142–13150.
172. Chai, X.; Huang, H.-H.; Liu, H.; Ke, Z.; Yong, W.-W.; Zhang, M.-T.; Cheng, Y.-S.; Wei, X.-W.; Zhang, L.; Yuan, G. *Chem. Commun.* **2020,** *56*, 3851–3854.
173. Elgrishi, N.; Chambers, M. B.; Artero, V.; Fontecave, M. *Phys. Chem. Chem. Phys.* **2014,** *16*, 13635–13644.
174. Elgrishi, N.; Chambers, M. B.; Fontecave, M. *Chem. Sci.* **2015,** *6*, 2522–2531.
175. Queyriaux, N.; Abel, K.; Fize, J.; Pécaut, J.; Orio, M.; Hammarström, L. *Sustain. Energy Fuels* **2020,** *4*, 3668–3676.
176. Queyriaux, N. *ACS Cat.* **2021,** *11*, 4024–4035.
177. De La Torre, P.; Derrick, J. S.; Snider, A.; Smith, P. T.; Loipersberger, M.; Head-Gordon, M.; Chang, C. J. *ACS Cat.* **2022,** *12*, 8484–8493.
178. Wang, M.; Chen, L.; Lau, T. C.; Robert, M. *Angew. Chem. Int. Ed.* **2018,** *57*, 7769.
179. Bohn, A.; Moreno, J. J.; Thuéry, P.; Robert, M.; Rivada-Wheelaghan, O. *Chem. Eur. J.* **2023,** *29*, e202202361.
180. Song, S.; Lee, W.; Lee, Y.; Cho, K.-B.; Lee, J.; Seo, J. *Inorg. Chem.* **2023,** *62*, 2326–2333.
181. Droghetti, F.; Amati, A.; Pascale, F.; Crochet, A.; Pastore, M.; Ruggi, A.; Natali, M. *ChemSusChem* **2024,** *17*, e202300737.
182. Boudreaux, C. M.; Nugegoda, D.; Yao, W.; Le, N.; Frey, N. C.; Li, Q.; Qu, F.; Zeller, M.; Webster, C. E.; Delcamp, J. H.; Papish, E. T. *ACS Cat.* **2022,** *12*, 8718–8728.
183. Sun, L.; Reddu, V.; Xi, S.; Dai, C.; Sheng, Y.; Su, T.; Fisher, A. C.; Wang, X. *Adv. Energy Mater.* **2022,** *12*, 2202108.
184. Cometto, C.; Chen, L.; Lo, P.-K.; Guo, Z.; Lau, K.-C.; Anxolabéhère-Mallart, E.; Fave, C.; Lau, T.-C.; Robert, M. *ACS Cat.* **2018,** *8*, 3411–3417.
185. Wang, M.; Chen, L.; Lau, T.-C.; Robert, M. *Angew. Chem. Int. Ed.* **2018,** *57*, 7769–7773.
186. Cometto, C.; Chen, L.; Anxolabéhère-Mallart, E.; Fave, C.; Lau, T.-C.; Robert, M. *Organometallics* **2019,** *38*, 1280–1285.
187. Loipersberger, M.; Cabral, D. G. A.; Chu, D. B. K.; Head-Gordon, M. *J. Am. Chem. Soc.* **2021,** *143*, 744–763.
188. Gao, J.; Dai, G. *Comput. Theor. Chem.* **2022,** *1214*, 113794.

189. Ma, B.; Chen, G.; Fave, C.; Chen, L.; Kuriki, R.; Maeda, K.; Ishitani, O.; Lau, T.-C.; Bonin, J.; Robert, M. *J. Am. Chem. Soc.* **2020,** *142*, 6188–6195.
190. Ho, P.-Y.; Cheng, S.-C.; Yu, F.; Yeung, Y.-Y.; Ni, W.-X.; Ko, C.-C.; Leung, C.-F.; Lau, T.-C.; Robert, M. *ACS Cat.* **2023,** *13*, 5979–5985.
191. Tsubonouchi, Y.; Takahashi, D.; Berber, M. R.; Mohamed, E. A.; Zahran, Z. N.; Alenad, A. M.; Althubiti, N. A.; Yagi, M. *Electrochim. Acta* **2021,** *387*, 138545.
192. Barlow, J. M.; Yang, J. Y. *ACS Cent. Sci.* **2019,** *5*, 580–588.
193. Saha, P.; Amanullah, S.; Dey, A. *Acc. Chem. Res.* **2022,** *55*, 134–144.
194. Parkin, A.; Seravalli, J.; Vincent, K. A.; Ragsdale, S. W.; Armstrong, F. A. *J. Am. Chem. Soc.* **2007,** *129*, 10328.
195. Chapovetsky, A.; Welborn, M.; Luna, J. M.; Haiges, R.; Miller, T. F., 3rd; Marinescu, S. C. *ACS Cent. Sci.* **2018,** *4*, 397–404.
196. Chapovetsky, A.; Do, T. H.; Haiges, R.; Takase, M. K.; Marinescu, S. C. *J. Am. Chem. Soc.* **2016,** *138*, 5765.
197. Beley, M.; Collin, J. P.; Ruppert, R.; Sauvage, J. P. *J. Am. Chem. Soc.* **1986,** *108*, 7461.
198. Costentin, C.; Drouet, S.; Robert, M.; Savéant, J. M. *Science* **2012,** *338*, 90.
199. DeLuca, E. E.; Xu, Z.; Lam, J.; Wolf, M. O. *Organometallics* **2019,** *38*, 1330–1343.
200. Azcarate, I.; Costentin, C.; Robert, M.; Savéant, J. M. *J. Am. Chem. Soc.* **2016,** *138*, 16639.
201. Sung, S.; Kumar, D.; Gil-Sepulcre, M.; Nippe, M. *J. Am. Chem. Soc.* **2017,** *139*, 13993–13996.
202. Gotico, P.; Halime, Z.; Leibl, W.; Aukauloo, A. *ChemPlusChem* **2023,** *88*, e202300222.
203. Chen, H.; Chen, L.; Chen, G.; Robert, M.; Lau, T.-C. *ChemPhysChem* **2021,** *22*, 1835–1843.
204. Xia, W.; Wang, F. *Mol. Catal.* **2023,** *535*, 112884.
205. Durfy, C. S.; Zurakowski, J. A.; Drover, M. W. *ChemSusChem* **2024,** *17*, e202400039.
206. Francke, R.; Schille, B.; Roemelt, M. *Chem. Rev.* **2018,** *118*, 4631.
207. Krogman, J. P.; Foxman, B. M.; Thomas, C. M. *J. Am. Chem. Soc.* **2011,** *133*, 14582–14585.
208. Guo, Z.; Chen, G.; Cometto, C.; Ma, B.; Zhao, H.; Groizard, T.; Chen, L.; Fan, H.; Man, W.-L.; Yiu, S.-M.; Lau, K.-C.; Lau, T.-C.; Robert, M. *Nat. Catal.* **2019,** *2*, 801–808.
209. Bharti, J.; Chen, L.; Guo, Z.; Cheng, L.; Wellauer, J.; Wenger, O. S.; von Wolff, N.; Lau, K.-C.; Lau, T.-C.; Chen, G.; Robert, M. *J. Am. Chem. Soc.* **2023,** *145*, 25195–25202.
210. Ouyang, T.; Wang, H.-J.; Huang, H.-H.; Wang, J.-W.; Guo, S.; Liu, W.-J.; Zhong, D.-C.; Lu, T.-B. *Angew. Chem. Int. Ed.* **2018,** *57*, 16480–16485.
211. Dey, S.; Todorova, T. K.; Fontecave, M.; Mougel, V. *Angew. Chem. Int. Ed.* **2020,** *59*, 15726–15733.
212. Ahmed, M. E.; Rana, A.; Saha, R.; Dey, S.; Dey, A. *Inorg. Chem.* **2020,** *59*, 5292–5302.
213. Intrator, J. A.; Velazquez, D. A.; Fan, S.; Mastrobattista, E.; Yu, C.; Marinescu, S. C. *Chem. Sci.* **2024,** *15*, 6385–6396.
214. Roy, S.; Sharma, B.; Pécaut, J.; Simon, P.; Fontecave, M.; Tran, P. D.; Derat, E.; Artero, V. *J. Am. Chem. Soc.* **2017,** *139*, 3685.

About the authors

Dr. Casadevall began her academic career at the University of Girona, where she completed her BSc (2013) and MSc (2014). Then she moved to ICIQ (Tarragona) to do a PhD (2019) working on homogeneous systems for artificial photosynthesis and photocatalysis. Subsequently she joined the University of Cambridge (UK) as a BBSRC postdoctoral researcher and later as a Marie Skłodowska–Curie Individual Fellow working on biohybrid systems for artificial photosynthesis. In October 2022 she came back to Spain and started her independent career with a "La Caixa Junior Leader Incoming Fellowship" at ICIQ and the University Rovira i Virigli (URV), where she is currently a Ramón y Cajal fellow (equivalent to Assistant Professor tenure-track), working on the development of catalyst-functionalized polymeric microreactors to produce solar fuels and chemicals.

Prof. Lloret-Fillol began his academic career at the University of Valencia, where he completed his PhD in 2006. Subsequently, he joined Prof. L.H. Gade's group at the University of Heidelberg as a Marie Curie postdoctoral fellow. In 2010, he launched his independent career, mentored by Prof. M. Costas under the Ramón y Cajal program at the University of Girona. By 2014, he was appointed Group Leader at the Institut Català d'Investigació Química (ICIQ), and in 2015, became an ICREA Research Professor. That same year, he received an ERC Consolidator Grant. His research focuses on artificial photosynthesis and catalysis.